Characterization studies of carbon nanotubes as cold electron field emitters for electron cooling applications in the Extra Low ENergy Antiproton (ELENA) ring at CERN

Thesis submitted in accordance with the requirements of
the University of Liverpool for the degree of Doctor of Philosophy by

Bruno Galante

February, 2023

Abstract

Electron emission allows the extraction of electrons from a material, commonly a metal or a semiconductor. There are three main processes for achieving electron emission: thermionic emission, photo-emission, and field emission.

Electron emission is of high importance in electron cooling. Electron cooling guarantees beam quality in low-energy antimatter facilities. In the Extra Low ENergy Antiproton ring (ELENA), the electron cooler reduces the emittance growth of the antiproton beam so that a focused and bright beam can be delivered to the experiments at the unprecedentedly low energy of 100 keV.

Cold emission can be beneficial in the electron cooler of ELENA for avoiding the use of a thermionic cathode. The thermionic cathode imposes constraints on the beam temperature, the fragility of the gun, and the gun design. A cold cathode may solve all these problems at once. In this thesis work, cold emission is achieved via field emission from carbon nanotubes (CNTs).

For the electron cooler of ELENA, the lifetime and the current stability of the electron source play a primary role. Furthermore, it is important to pulse the cathode to promptly enable/disable the cooling process and to change the electron beam energy according to the cooling stage and the ELENA beam cycle. This work proves that a CNT array can stably emit for hundreds of hours and a record emission time of 1500 hours has been proved. The operation of a CNT cathode in current switching mode has also been tested. Rise and fall times below 1 μs have been proved with unaltered current emission stability during operation.

Several constraints can arise when using CNTs as electron sources. Among these, the role of an extracting grid needs accurate evaluation. In this Ph.D. work simulations of the beam passage through micro-metric grids were performed. These simulations were aimed at studying the effect of the grid on the beam current, trajectory, and transverse energy. It was found that a grid with a squared pattern, 15 μm hole size and 3 μm bar width, does not significantly alter the beam trajectory and the beam transverse energy. The transparency of such a grid was about 68%.

Finally, guidelines for mitigating possible issues related to the design of a CNT-based cold cathode electron gun were addressed. A gun layout has been

proposed after the optimization of all components through electromagnetic simulations.

The findings of the research carried out within the frame of this Ph.D. project are applicable to a wide range of CNT applications: from electron guns for accelerator science to X-ray tubes, CNT-based televisions, and any case where electron extraction is required.

The findings from studies into extracting grids and gun design have an even wider reach and benefit any application where particle extraction and transport are involved.

Acknowledgements

It is not easy to find the right words to acknowledge all the people who have helped, inspired, or supported me in this long journey. I will try to be brief, even though some people would deserve at least a page each. I must start with my family, who has always supported me throughout my life. Without them, I would not be here. I will always be grateful to them. Then, a mention must be given to my friends spread everywhere in the world. Friends I knew already, or friends I made along this way. All these people kept me going in these past years. Then I must mention my section at CERN, they were of great help to my professional growth and the successful completion of my experiments. In particular, my supervisor, Gerard, gave me the chance to be part of this project. He chose me, and he supported me. This can't be forgotten. Thanks then to my colleagues for their help in devising parts of my experiments, in particular Jean Cenede, Alexandre Frassier, and Wilfried Devauchelle. Furthermore, the TE and EN departments at CERN deserve thanks as well for their help in the materials characterization. Finally, I want to conclude by thanking my supervisors in Liverpool: Carsten, Javier, and Oznur. Without them, this thesis would probably look quite different. For the same reason, I must thank Aaron, Liam, and Steven, who helped polish my sometimes too Italian English. I hope I have not forgotten anyone. Certainly, this has been quite the journey.

Contents

Chapter 1

Introduction

1.1 CERN

The Conseil Européen pour la Recherche Nucléaire (CERN) [1], is a European research centre whose roots date back to 9$^{\text{th}}$ December 1949. The reason behind the creation of what is now one of the biggest research centres in the world comes from the need to restore European science after the end of World War 2. The idea was born thanks to some of the brightest minds of the time. Raoul Dautry, Pierre Auger, and Lew Kowarski in France, Edoardo Amaldi in Italy, and Niels Bohr in Denmark were some of those visionary minds. It was in 1951 during a UNESCO meeting held in Paris that the establishment of CERN was decided, with the collaboration of 11 countries. The first brick was laid by the first Director-General Felix Bloch, in July 1955.

CERN has today 23 Member States which, through delegates, take part in the CERN Council with the aim of directing CERN's research goals.

1.1.1 Research at CERN

CERN is a large complex containing a number of accelerators that have been constructed and then succeeded over the years with the aim of reaching higher and higher energies. To better understand the accelerators composing the complex they are listed, as well as their main goals, as follows [1]:

- Linac 4 (LINear ACcelerator 4): accelerates protons to the energy of 160 MeV.

- Proton Synchrotron Booster (PSB): accelerates the proton beam to 2 GeV.
- Proton Synchrotron (PS): accelerates protons to the energy of 26 GeV.
- Super Proton Synchrotron (SPS): acceleration to 450 GeV.
- Large Hadron Collider (LHC): final acceleration to 6.5 TeV.

The Large Hadron Collider (LHC) is the most powerful accelerator in the world. Here two proton beams circulate in opposite directions and then collide in four interaction points, in each of them the energy of the collisions reaches 13 TeV. Protons are not the only particles that can be accelerated in the LHC. Thanks to a source of vaporized lead, it is also possible to produce and then accelerate lead ions through the LINAC 3 (LInear ACcelerator 3) and LEIR (Low Energy Ion Ring) [2].

1.1.2 The antimatter factory

Another big branch of experiments takes place in the so-called antimatter factory. Here precision studies on antimatter are performed to solve some of the most important science riddles. Why is the Universe mainly composed of matter? Where did all the antimatter go? In the antimatter factory, the antiprotons are created and then prepared for the experiments to try and answer these fundamental questions [1].

In the antimatter factory, there are two machines: the Antiproton Decelerator (AD) [3] and the Extra Low ENergy Antiproton (ELENA) ring [4, 5].

To create antiprotons, a proton beam coming from the PS is directed into a target. Among the many particles created due to the collisions, there are antiprotons. The antiprotons with correct energy are injected and stored into the AD, where they are consequently decelerated and cooled before being transferred to ELENA. In ELENA they undergo a further deceleration and cooling process before being delivered to the experiments placed in the AD hall. The antimatter experiments work on characterizing antimatter properties such as the charge-to-mass ratio of antiprotons, the hyperfine structure of antihydrogen, the gravitational constant “g” of antihydrogen, etc. This information is compared to the knowledge that we already possess about

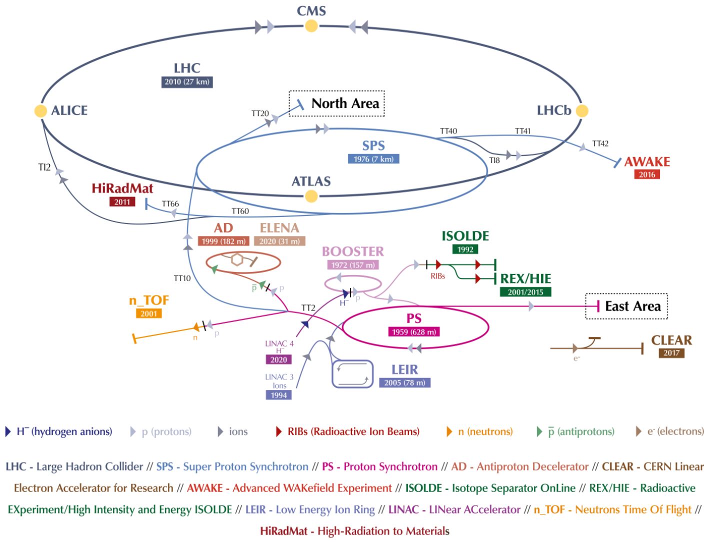

Figure 1.1: CERN Accelerator Complex [1].

their common "normal" counterparts, protons and hydrogen, to look for discrepancies that could account for the lack of antimatter in the Universe as we know it [1, 3].

1.1.3 CERN accelerator complex

On top of all the accelerators on the complex, CERN hosts many other facilities which allow for a large number of different experiments, spanning: neutrino research, beam-target collisions, galactic cosmic rays detection, and many more [1]. Figure 1.1 shows a schematic of where most of the machines and experiments at CERN are located.

1.2 AD & ELENA

ELENA, figure 1.2, is a compact ring for the cooling and deceleration of antiprotons coming from the AD. The AD fulfills several tasks: collect antiprotons, decelerate them down to 5.3 MeV (momentum of 100 MeV/c), cool the beam, and eject the antiproton beam via the transfer lines to ELENA [1, 4, 5]. The ELENA beam cycle is composed of two steps of deceleration accompanied by the two stages of electron cooling. The typical ELENA cycle

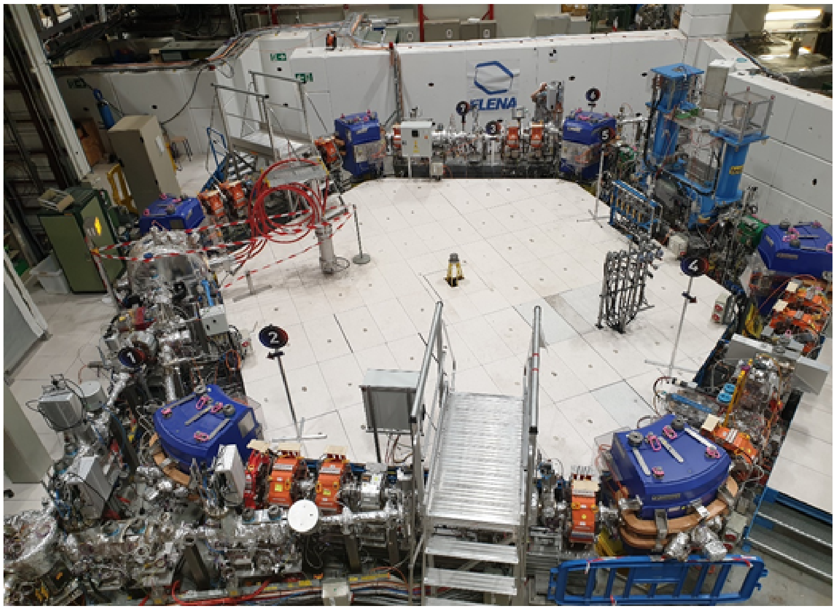

Figure 1.2: ELENA

is shown in figure 1.3 and all basic parameters of the ELENA ring are listed in table 1.1.

ELENA, with its circumference of 30.4 m, is placed in the AD Hall and in the center of the AD [4–6]. The goal of ELENA is to decelerate the antiproton beam to the unprecedented kinetic energy of 100 keV and furthermore: increase the number of available anti-protons by one or two orders of magnitude, serve up to four experiments simultaneously, and allow for new experiments.

The electron cooling process plays a key role in the operation of the AD and ELENA as it is essential in order to deliver a small emittance and energy spread beam to the experiments for investigation and trapping. Particularly in ELENA, since the beam is decelerated to such a low final kinetic energy (100 keV), the cooling process is vital in order to make the deceleration efficient and reach the required beam emittance. This means that the electron cooler is undoubtedly one of the key devices of the ELENA facility and therefore needs particular care for ensuring a successful beam delivery.

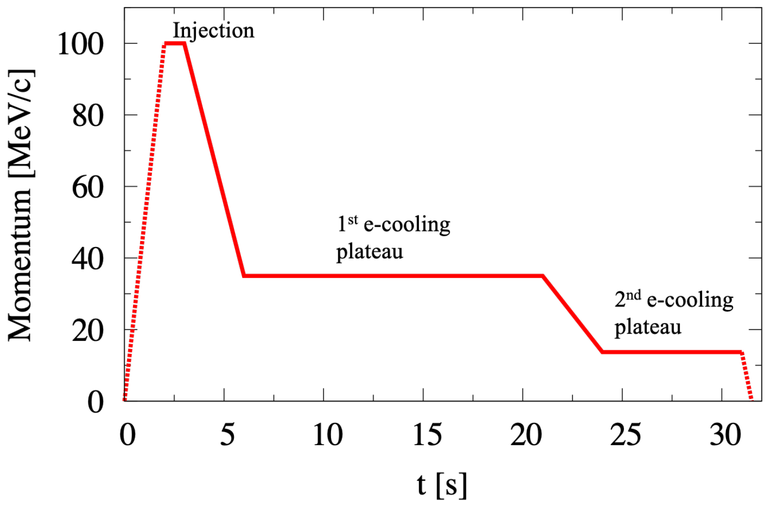

Figure 1.3: ELENA Typical Cycle [6].

Table 1.1: ELENA - basic parameters

Item	Value	Dimension
Circumference	30.4	m
Beam momenta max/min	100 / 13.7	MeV/c
Energy range max/min	5.3 / 0.1	MeV
Working Point	2.3 / 1.3	Q_x / Q_y
Ring Acceptance	75	π mm mrad
Intensity of injected/ ejected beam	$3.0 \times 10^7/1.8 \times 10^7$	
Number of extracted bunches	≤ 4	
Emittances (h/v) of extracted bunches	4 / 4	π mm mrad [95%]
$\Delta p/p$ of extracted beam	2.5×10^{-3}	[95%]
Pressure	3×10^{-12}	Torr

1.3 Electron cooling

When a beam is circulating in a storage ring it usually undergoes emittance growth due to phenomena such as Intra Beam Scattering (IBS), scattering with residual gas molecules, and space-charge effects. This causes an increase in the beam size and ultimately can result in losses when the beam size approaches the physical or dynamic acceptance. To counteract these effects electron cooling becomes necessary [7–10].

Electron cooling was first proposed in 1966 by Budker [11] as a method that allows the reduction of the occupied phase space of a particle beam [7–10]. Budker's idea was based on two main points: the use of an electron beam as an absorber, and to equalizing average velocities of heavy particles and electrons, which gives the maximal value of the cross-section of electromagnetic interaction [8, 11].

In this way, it is possible to introduce an effective "friction" in a particle beam, which facilitates the reduction of the beam phase space volume (emittance). In other words, electron cooling is a fast process for reducing the size, divergence, and energy spread of stored charged-particle beams without removing particles from the beam [7, 8].

1.3.1 Simplified view

The cooling process is fulfilled by combining a monochromatic electron beam with a circulating beam over a short length of the storage ring, e.g. the drift region. The electron beam is continuously replenished with an electron gun—in many cases this is a thermionic gun. After generation, the electrons are electrostatically accelerated to the average ion velocity and then injected into the drift region such that they overlap the circulating beam [7, 10].

If we observe the region from the frame moving with the velocity of the electrons (rest frame), then the electrons will be at rest in our coordinate system. Whilst the ions will pass through with different velocities and directions as if they were part of a hot gas. The ions will then collide with the electrons and through Rutherford scattering they will lose energy; this energy will be transferred to the electrons in the form of heat thanks to Coulomb interactions. As the electron beam is constantly replenished, energy is removed from the electron-ion system. Thus the ion beam (or ion gas in this analogy) will reduce in temperature due to the many collisions. This is the reason why such a process was named "electron cooling" [7–10]. A reduced

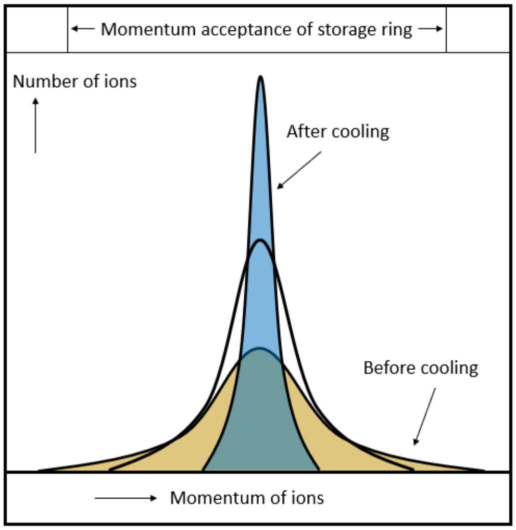

Figure 1.4: Effect of the electron cooling on the beam.

transverse energy spread is also beneficial as the ion beam will tend to the transverse energy spread of the electrons through the cooling process. The effect of the electron cooling on the size and momentum spread of stored beams or trapped ions is illustrated in figure 1.4.

1.3.2 Electron cooling theory

To study how the equilibrium temperature is reached the interactions between electrons and ions must be considered. The main models used for studying the electron-ion interactions are:

1. single collisions
2. multiple collisions
3. binary-collision model
4. dielectric plasma description

The following derivations are based on the work of Helmuth Poth [7]. In electron cooling, the ion-electron interactions are based on a series of small-angle scatterings where only a small fraction of momentum and energy are transferred in each scattering event. At the same time, the initial direction of the ion will be slightly perturbed after each collision. The two main effects due to these collisions can be therefore isolated:

- friction, most commonly named frictional force or cooling force – reduction of the momentum of the ion along the initial direction
- diffusion – heating due to multiple scatterings

The diffusion coefficient D is defined as

$$D = \frac{d}{dt}(p_i^2 \Theta_{rms}^2), \tag{1.1}$$

where Θ_{rms}^2 is the root mean square (r.m.s.) width of the angular distribution of the ion beam and p_i is momentum transferred from the ion to the electron.

Single collisions

In the case of a single collision, the momentum transferred from the ion to the electron is

$$\Delta p = \int \epsilon \; dt = \frac{1}{4\pi\epsilon_0} \int \frac{Ze^2}{x^2 + b^2} \; dt, \tag{1.2}$$

where ϵ is the Coulomb force, $\epsilon_0 (= 8.854 \times 10^{-12} As/Vm)$ is the permittivity of free space, Z is the charge of the ion, e is the elementary charge and b (see figure 1.5) is the impact parameter. Neglecting the longitudinal part of the force

$$\Delta p = \int_{-\infty}^{+\infty} \epsilon_\perp \; dt = \int_{-\infty}^{+\infty} \frac{Ze^2 b}{v_i \sqrt{(x^2 + b^2)^3}} dx = \frac{2Ze^2}{4\pi\epsilon_0 v_i b}. \tag{1.3}$$

And the energy transferred from the ion to the electron can be written as

$$\Delta E_{i \to e}(b) = \frac{(\Delta p)^2}{2m_e}, \tag{1.4}$$

In figure 1.5 is possible to see a summary of the scattering variables.

Multiple collisions

In the case of multiple collisions, a statistical approach is necessary in order to study the effect of the many small-angle scatterings. It is then possible to obtain the cooling force and the diffusion coefficient by integrating over all the possible values of the impact parameters and therefore, over all scattering

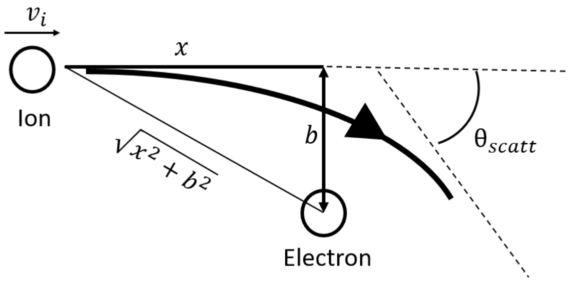

Figure 1.5: Scattering variables.

angles. The results show a relation between the cooling force and the diffusion coefficient as

$$F_n = \frac{1}{2m_e}\frac{\partial D_{mn}}{\partial v_{i_m}}. \tag{1.5}$$

This shows how the friction and diffusion processes happen simultaneously during the cooling process.

The multiple collisions model permits obtaining new and more precise relations for the cooling force and the diffusion coefficient in analogy to electrostatic quantities. It can be shown that [7, 10]

$$\mathbf{F}(\mathbf{v}_i) = -F_0 c^2 L_C grad_{v_i}\Phi \tag{1.6a}$$

$$D_{mn}(v_i) = m_e F_0 c^2 \frac{\partial^2 \Xi}{\partial v_{i_m}\partial v_{i_n}}, \tag{1.6b}$$

where Φ and Ξ are defined as quasi-potentials. L_C is the Coulomb logarithm and it is defined as

$$L_C = \int_{b_{min}}^{b_{max}} \frac{db}{b} = ln\frac{b_{max}}{b_{min}}, \tag{1.7}$$

and $F_0 = 4\pi Z^2 n_e r_e^2 m_e c^2$.

Binary-collision model

In this further extension, the magnetization of the electrons is also added to the model. Electrons in a uniform magnetic field have an additional helical motion perpendicular to the magnetic field direction. The frequency of such motion is given by the cyclotron frequency and the radius of the path is called gyration radius. This leads to a first important distinction, the collisions are divided into two classes: fast collisions and adiabatic collisions. The difference between the two is the collision time. In the first case, the collision time is considered smaller than the cyclotron period and the electrons are considered free. In this case, the assumptions considered in the previous sections are still valid. In the second case, the electrons perform several gyrations within the collision time, so that the motion in the transverse direction cancels out. A way to approach the problem is to divide the force into two components. The first takes into account only the fast collisions and is therefore essentially equivalent to the previous case. It can be called the non-magnetized case, F^{NM}. The latter takes into account solely the adiabatic collisions and represents the magnetized case or adiabatic case F_{ad} [7, 9, 10, 12],

$$F = F^{NM} + F^{ad}. \tag{1.8}$$

The calculation of the adiabatic force is then split into two main cases depending on the relation between the ion velocity, v_i, and the longitudinal velocity spread $\Delta_\parallel$: (i) $v_i >> \Delta_\parallel$, (ii) $v_i << \Delta_\parallel$.

This model gives a good approximation for the non-magnetic case. In the case of a uniform magnetic field, the calculation was limited in the case of collisions falling into the strict two classes discussed above and the results are consistent only for such extremes. Moreover, collective effects have not yet been considered and these have serious implications when considering plasmas.

A choice regarding the impact parameters, depending on the particle velocity, was made in order to solve the equations for the cooling force and the diffusion coefficient. At high velocities, the cooling force can be limited to fast collisions and adiabatic collisions, which means either small impact parameters or large impact parameters. This case is therefore well treated with the binary model. However, at low velocities, the choice of impact parameters is less well constrained. In such a case the binary model is no longer valid and the "dielectric plasma description" is required for a more comprehensive study [7–9, 12, 13].

Dielectric plasma description

The dielectric plasma description allows the study of collective effects, but the description can no longer be described analytically. In this approach, the force is derived from the electric field E_{ind} induced by the ions which also acts back on it. In this case, instead of using the electric field, the potential

ϕ is used. As the ions have velocity v_i, the potential varies in space and time. It is thus convenient to use the Fourier transform for the potential $\phi(r,t) \rightarrow \phi(\mathbf{k},\omega)$. For electrons at rest the result is equivalent to the binary model. The situation changes when introducing magnetic confinement.

The key feature of the dielectric plasma model is the possibility to correctly treat collisions at every possible impact parameter, while also reconnecting to the binary model in the case of zero magnetic field. The results provided by this method are quite precise, but in many cases it is not possible to solve the equation analytically and numerical approaches are required [7, 13].

1.3.3 The cooling time

The calculation of the cooling time is not typically straightforward, and in most cases it needs to be performed numerically given the complexity of the expressions. However, it is possible to calculate the cooling time analytically for a particular case of interest: an ion beam with Gaussian velocity distribution and a width small enough so that the cooling force is directly proportional to the ion velocity. For simplicity, the case with no magnetic field will be considered [7, 11, 13]. The cooling time can then be expressed as

$$\tau = \frac{3}{2\sqrt{2\pi}} \frac{\beta\gamma^2}{c\, r_p \eta L_c} \frac{m_e c^3}{ej} \left(\frac{\Delta_e}{m_e c^2} \right)^{3/2}, \tag{1.9}$$

where η is the proton orbit fraction occupied by the electron beam, r_p is the classical radius of the proton, β is the proton equilibrium velocity in the units of the speed of light c, $\gamma = (1-\beta^2)^{-1/2}$, Θ_{ei} is the r.m.s value of the ratio of the i-th transverse component of the velocity to the average velocity, j is the electron current density and Δ_e is the electron beam temperature. This expression correlates the cooling time with some of the key electron beam parameters such as the electron temperature, Δ_e, and the electron beam current density, j [11].

Finally, a strong dependence on the electron beam temperature, Δ_e, is observed. This shows how the electron beam temperature plays a major role in affecting the cooling time [7, 10, 11, 13].

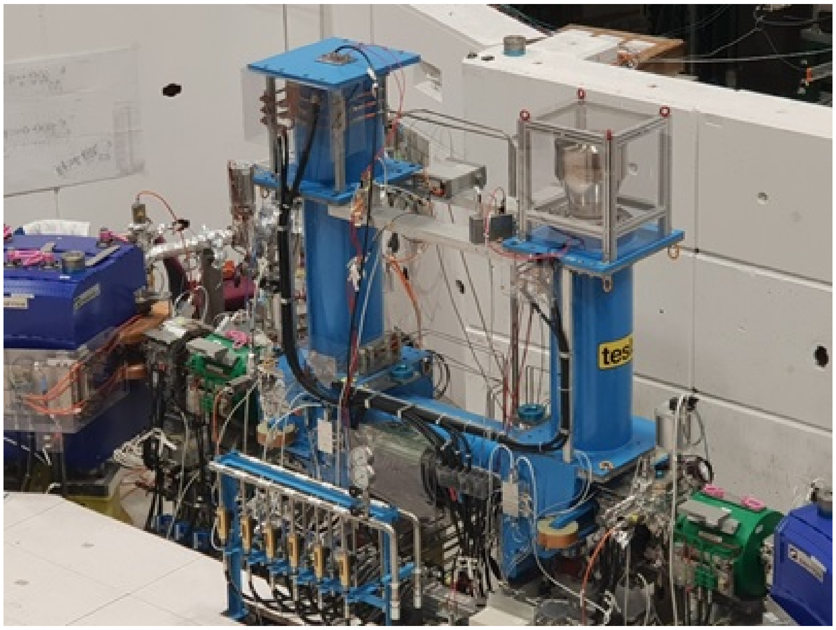

Figure 1.6: The ELENA electron cooler.

1.4 The electron cooler in ELENA

When designing an electron cooler great care must be taken, especially considering the unprecedented low energies of ELENA. The design of the electron gun electrodes, the quality of the magnetic field, and the efficient collection of the electrons must be optimal. These are all necessary parameters for producing a beam: (i) that has the desired energy and current properties; (ii) that circulates in the electron cooler without losses and that can efficiently overlap with the circulating antiproton; (iii) and that can be dumped in the collector without causing damage to the collector itself. A photo of the ELENA electron cooler is reported in figure 1.6.

The ELENA electron cooler works at two stages of the beam cycle. The electron beam generated by the electron gun must be cold and stable at the energies of 355 eV, for the first plateau, and only 55 eV for the second plateau. The typical ELENA beam cycle was shown in 1.3.

The antiproton beam is injected into ELENA at 100 MeV/c. It then undergoes a first deceleration process to 35 MeV/c. After this deceleration, the first electron cooling stage takes place in order to correct the emittance

Table 1.2: Electron cooler of ELENA - basic parameters.

Item	Value	Dimension
Momentum	35 / 13.7	MeV/c
Electron Beam Energy	355 / 55	eV
Electron Current	5 / 1	mA
B_{Gun}	1000	G
B_{Drift}	100	G
Toroid Bending Radius	0.25	m
Cathode Radius	8	mm
Electron Beam Radius	25	mm
Cooling (drift) Length	1.0	m
Total Cooler Length	1.93	m

blow-up caused by the deceleration process and from possible injection mismatches. The beam is then further decelerated to 13.7 MeV/c (100 keV) and cooled a second time. After this cycle, the antiproton beam is ready to be delivered to the experiments.

The electron cooler's layout and magnet system are largely based on the electron cooler previously built at Kyoto University [6, 14, 15]. Such an electron cooler was also designed for relatively low energies and high field uniformity, and therefore was a near-perfect match for the ELENA requirements.

In table 1.2 the main parameters of the ELENA electron cooler are listed [6, 14].

In order to describe the electron cooler there are several key components that must be discussed: (i) the magnet system, (ii) the electron gun, and (iii) the collector. All the details of the magnet system and the figures are based on the Tesla Engineering [16] internal report "Electromagnetic analysis of the ELENA magnet system" [17].

1.4.1 Magnet system

The magnet system plays a key role in keeping the electron beam in the desired orbit. To do so good field homogeneity is required along the electron beam path so that the beam remains uniform along its whole diameter (about 50 mm). The main magnetic system is composed of: three standard solenoids: gun solenoid, drift solenoid, collector solenoid; expansion solenoid; and two toroids. Several smaller coils and correctors are also installed to provide field corrections and optimize the beam orbit. All correctors are listed below.

- circular correction coils
- Helmholtz correction coils
- steering saddles
- fine correction coils
- toroid correction coils
- squeeze coil
- orbit correction coils

The arrangement of the main elements is reported in figure 1.7.

Standard solenoids

The three standard solenoids work at a nominal value of 100 Gauss, but they are designed to reach 250 Gauss. The required field alignment (B_{trans}/B_{long}) is of less than 5×10^{-3} over a cylindrical volume of 50 cm in length and 30 mm in radius. Therefore, at the nominal value of 100 Gauss the misalignment is of about 0.5 Gauss is desired.

Circular correction coils

These coils are placed at each side of the standard solenoid, each placed 10 cm from the end.

Helmholtz correction coils

The Helmholtz coils are long rectangular saddle coils and their purpose is to steer the beam along the standard solenoids' length in order to reach optimal alignment with the circulating beam and therefore achieve the most efficient cooling. Their length is approximately equal to the solenoid length and there are two pairs of them in order to steer the beam both vertically and horizontally.

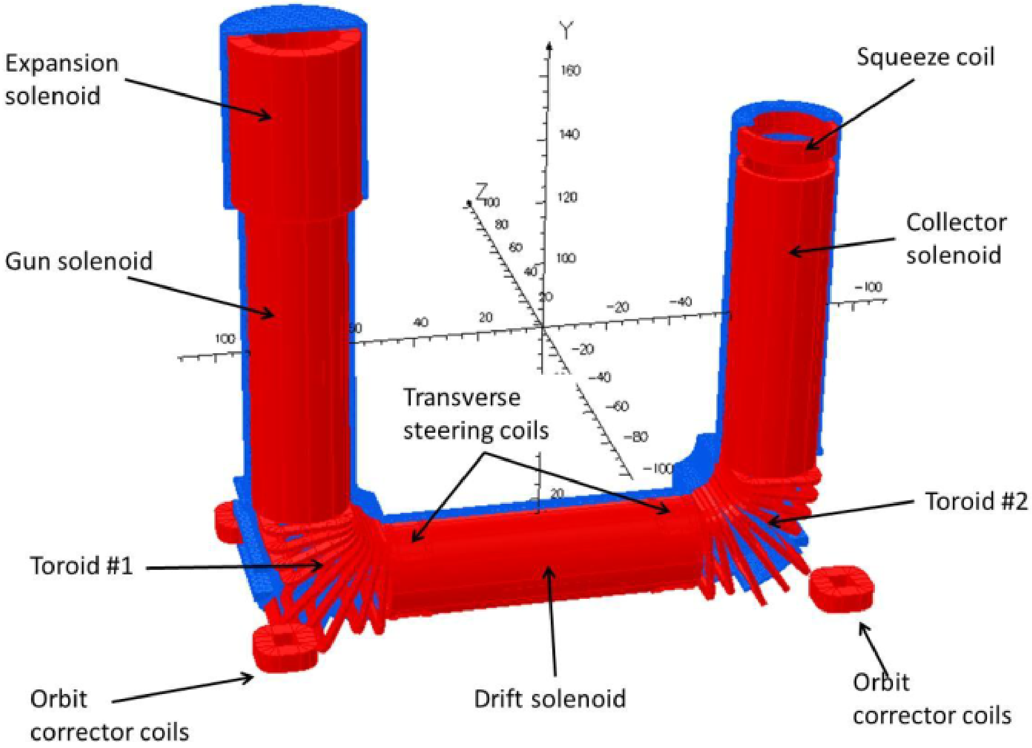

Figure 1.7: Arrangement of ELENA magnetic system.

Steering saddles

Due to the U shape of the cooler, a distortion in the magnetic field arises near the junction between the toroids and standard solenoids and needs to be corrected. This is achieved by means of additional correctors called steering saddles.

Fine correction coils

The fine correction coils are the last set of correction coils present in the standard solenoids. The fine correction coils come in pairs, for the horizontal and vertical plane respectively, in order to correct for both B_x and B_y. In this coordinate system the beam travels along the z direction. These correctors are saddle coils and there are 24 of them in total, 12 for controlling B_y and 12 for controlling B_x.

Expansion solenoid

The expansion solenoid is placed on the gun side, before the gun solenoid, and it is the section where the electron gun is placed. The geometry of the coil is identical to the standard solenoids. The main difference with the standard solenoids is the maximum magnetic field value reachable, 2,500 Gauss, whereas the nominal value for operation is 1,000 Gauss. The field variation is required to be of less than 5×10^{-3} over a 10 cm center region.

Because of the expansion and standard solenoids arrangement, the electron beam will go from a region of higher magnetic field, in the expansion solenoid with 1,000 Gauss, to a region of lower magnetic field, in the standard solenoid with 100 Gauss. In this way, the so-called “adiabatic expansion” can be achieved.

The adiabatic expansion permits a decrease in the transverse temperature of the electron beam. When the beam is generated at the cathode, it has a minimum transverse temperature of 0.1 eV and a beam size of about 16 mm in diameter, as per the cathode size. However, for the cooling process to be effective, the transverse temperature must be strongly reduced. Considering the magnetic field ratio in the cooler of ELENA (1,000 Gauss / 100 Gauss), it is possible to simultaneously decrease the beam transverse temperature by a factor ten and increase the beam size by a factor $\sqrt{10}$, thus reaching a beam size of about 50 mm of diameter, and the desired transverse temperature of about 10 meV [18, 19]. Therefore

$$R_f = \sqrt{\frac{B_{Exp}}{B_{Std}}} R_i, \quad k_B T_{\perp,f} = \frac{B_{Std}}{B_{Exp}} k_B T_{\perp,i}, \tag{1.10}$$

where R_f is the final beam radius and R_i is the initial beam radius. B_{Exp} and B_{Std} are respectively the magnetic field value in the expansion solenoid and the magnetic field value in the standard solenoid. k_B is the Boltzmann Constant and $T_{\perp,f}$ and $T_{\perp,i}$ are the final and initial transverse temperatures of the electron beam [18, 19].

Toroids

The toroids must bend the electron beam and allow for it to be efficiently transferred from the gun solenoid to the drift solenoid and then from the drift solenoid to the collector solenoid. In each toroid there are nine rectangular coils, e.g. racetrack-type coils. An illustration of the two toroids is reported in figure 1.7.

Toroid correction coils

Like for the standard solenoids, in the toroids too a set of correction coils is installed in order to allow for fine adjustment of the transverse field. There are two correction coils per toroid, one on each side.

Squeeze coil

The squeeze coil is placed at the collector side between the collector and the collector solenoid. Its purpose is to facilitate the injection of the beam in the collector.

Orbit correction coils

The orbit correction coils are placed outside each toroid section. The purpose of these coils is to balance the transverse component of the magnetic field generated by the gun, the collector solenoids, and the toroids. These transverse components affect the circulating antiproton beam orbit. Their placement is illustrated in figure 1.7.

1.4.2 Electron gun

The electron gun is used to produce an electron beam with a specified current and energy in order to achieve the most efficient electron cooling possible. For ELENA these are listed in table 1.1. The key parameters are that the gun must work during the whole operation time, typically in the order of months and it must produce a cold ($T_\perp < 0.1$ eV, $T_\parallel < 1$ meV) and relatively intense electron beam ($n_e \approx 1.5 \times 10^{12}$ m^{-3}).

The electron gun currently installed in ELENA is a thermionic gun which consists of a dispenser cathode made of tungsten and barium oxide (BaO). In order to produce electrons the cathode is heated to the temperature of 1,200 °C, the electrons are then accelerated by a series of electrodes designed to minimize the transverse temperature of the beam. Particular care was directed towards the design of the electrodes in order to obtain as flat as possible equipotential lines in the emission region, particularly around the cathode.

1.4.3 Collector

The collector reabsorbs the electrons after the cooling section. On its way, the electron beam undergoes a spreading achieved using the squeeze coil and repeller electrode. It is only at this point that the beam is dumped over the large surface of the collector. The reason for spreading the beam is to reduce the beam power per unit area to minimize outgassing from the collector surface. The maximum power of the electron beam in ELENA is less than 2 W, however, the outgassing caused by such beam dumping can still create pressure rises, which are better to be avoided in such a low pressure environment as ELENA's ($P \leq 4 \times 10^{-12}$ mbar).

Furthermore, the electromagnetic field at the collector has the additional task to create a barrier preventing secondary electrons to be accelerated back to the cooling section. These electrons would oscillate back and forth until colliding with the vacuum chamber, thus causing a pressure rise [6, 14].

1.4.4 Constraints and possible improvements

While the electron cooler of ELENA can efficiently cool the antiproton beam, a number of improvements can be made.

A possible improvement is an upgrade of the electron gun. The electron gun in ELENA is mostly based on previously designed guns such as the ones used in AD and LEIR, with adjustments to fit the particular requirements of ELENA. The thermionic cathode currently used in the electron gun serves the scope of the ELENA cooler, although it imposes several constraints. These are the use of high temperatures, a complicated and fragile heating system with a hot filament, and the use of a strong adiabatic expansion to reduce the transverse energy of the beam.

The use of an alternative emission process such as field emission could improve the gun performance as a high temperature would be no longer required for the electron emission. The high temperature used for the emission sets an intrinsic constraint on the minimum transverse energy spread of the beam. In our particular case, this minimum transverse energy spread is 0.1 eV. This is however the minimum value; due to the electron gun's electrodes and tail effect, the transverse energy spread can reach much higher values when going farther from the central region of the beam. Cold electron emission may erase this problem since the emission is not mediated by the application of temperature [20–23].

1.5 Research goal

The aim of this Ph.D. project is to characterize and assess the feasibility of using a cold cathode electron gun based on a novel nano-structured material: carbon nanotubes (CNTs) [6, 14, 20].

Contrarily to thermionic emission, field emission relies on the application of solely electric fields to both generate and control the electron beam. Furthermore, a thermionic gun leads to intrinsic constraints regarding the beam temperature due to the high temperatures required. Cold emissions could allow some of the limitations of thermionic emission to be overcome. Photo-emission is a possible cold emission solution, although its intricate setup arrangements and the usually short lifetime present significant hurdles to its use in ELENA. The only remaining option is field emission, however, its use has always been hindered due to the extremely high electric field necessary to extract significant currents. The use of nano-structures overcomes this limitation thanks to the field enhancement at the nano-structures' tips.

CNTs have gained attention in the last two decades due to their unique properties. For electron emission, their most appealing property is the high aspect ratio, which allows a strong field enhancement, and therefore high emitted currents at relatively low applied field. Furthermore, they present additional interesting properties: a chemically inert structure thanks to a stable carbon backbone; they can be produced in a cost-effective and scalable way. However, research into their use is somewhat limited.

This thesis sets the goal on a characterization of the emitting properties of CNTs and on a feasibility study towards their use as cathode material for the electron gun of the electron cooler of ELENA and/or for any electron gun application.

Several properties of a CNT-based cathode need evaluation for endorsing its possible use in operation.

The first emitting properties that must be evaluated are lifetime and current emission stability. Both are essential for use in operation where emission over long periods of time, e.g. months, is envisaged. In this thesis, a lifetime study will be performed as well as a current stability study at different applied electric fields. Conditioning also represents a vital parameter for ensuring reliable emission. A conditioning process will be then proposed based on emission and vacuum characterization results.

The compatibility with the requirements of the electron cooler of ELENA regarding maximum emitted current and current switching is also necessary. While the emitted current doesn't seem to be problematic due to the relatively high currents that CNTs can emit [20, 23–25], the current switching capabilities need testing as literature is scarce on the subject. CNTs will thus be tested switching the voltage on the cathode with a fast push-pull circuit in order to study the emission behavior in current switching mode.

Furthermore, in a field emission cathode, the use of extraction grids becomes necessary in order to enable homogeneous current emission from the whole cathode area. However, electric field distortions in the grid's holes can cause severe changes to the beam properties, mostly on beam transverse energy and beam current. These factors must be evaluated in order to assess the impact of using such extracting grids. A set of simulations will be devised in order to study the effect of several hole sizes and finally assess the minimum hole size required for matching ELENA's requirements.

Finally, based on the results achieved in the previous tests and simulations, a possible low-energy electron gun design will be proposed.

Chapter 2

Electron Field Emission

In this chapter, the main electron emission principles will be listed and briefly explained. Highlighting the main difference among them as well as their respective weaknesses and strengths. As field emission is the main subject of this Ph.D. project, a formal description of the physics behind it is thus described in more detail. A distinction between the main field emission theories is also reported, focusing on the distinction between field emission from flat metals or nano-structures.

2.1 Introduction

Electron emission represents the extraction of electrons from a material, commonly a metal or a semiconductor. Such extraction results in free electrons, thus no longer bonded to the material. This can allow the formation of an electron beam if the electrons are collected and then accelerated by applying an electric field.

There are several ways to extract electrons from a material, the three most common methods are thermionic emission, photo-emission, and field emission. The difference between the three principles relies on how electrons are forced out of the material. The electrons are bound to the material and to free them they must be excited with an energy high enough to overcome the potential barrier between the material's surface and the vacuum. In thermionic emission, this energy is provided by means of high temperatures. The principle of photo-emission is somewhat similar, but in this case the electrons are excited by means of collisions with photons with suitable energy.

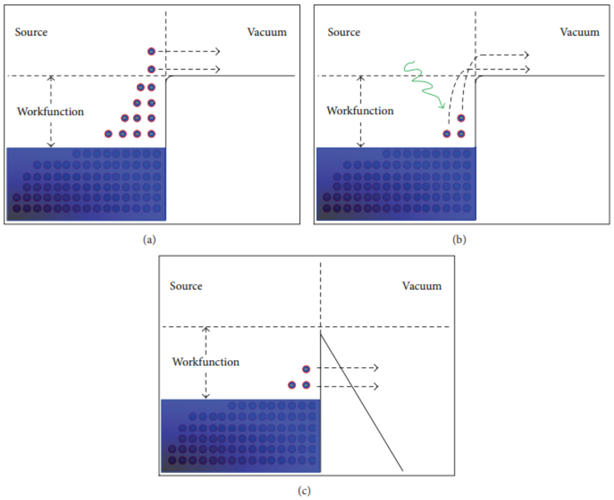

Figure 2.1: The three main electron emission principles: a) Thermionic emission, b) Photo-emission, c) Field emission [26].

The photons are generated with a laser which is pointed at the cathode's surface which allows for a low energy bandwidth in the emitted electrons. In field emission the scenario is quite different. By applying a strong electric field, it is possible to bend the potential barrier between the material's surface and the vacuum, therefore allowing for a quantum effect to arise: the tunneling through the potential barrier. The main differences among the three emission principles are well illustrated in figure 2.1, [26].

In general, the choice of one principle over the others relies on the number of electrons required, the energy distribution of the emitted electrons, and mechanical aspects due to experimental considerations. In our case field emission was chosen as it allows a cold cathode and for its only dependence on the electric field. Photo-emission presents a number of problems such as an intricate experimental setup due to the need for a suitable laser system to produce the photons required for the emission, the usually poor stability of the emitted current, and the usually short lifetime of the photo-cathodes (on the order of a few days) [27, 28].

Field emission may solve all these problems at once, providing a cold, stable, and long-lifetime cathode. Nonetheless, it also presents technical problems such as the need for very strong electric fields in order to extract relatively high currents. This has often hindered the use of field emission cathodes thus far. Field emission was proposed for the first time by Fowler and Nordheim in 1928 [29]. However, it has gained wider attention in the last 20 years with the advancement of nano-technology, which has brought to the creation of nano-materials like CNTs and metal nano-tips. By using such geometries it is possible to enhance the electric field, thus reaching larger local electric fields compared to the applied macroscopic field [20, 26, 30, 31].

In order to describe field emission more rigorously several steps will be considered as follows: Fowler-Nordheim theory, Murphy-Good theory, and field emission in nano-structures.

2.2 Fowler-Nordheim theory

Fowler and Nordheim, in 1928, were the first to propose a theory for electron emission from flat metal surfaces in the case of the presence of a strong electric field and at low temperatures. In order to derive the semi-classical Fowler-Nordheim formula they start by considering the kinetic energy of electrons at the interface between the material's surface and the vacuum. The problem can be approached in one dimension and the interface is represented by a potential barrier with value C, figure 2.2 [29].

In reality, the top corners are in both cases rounded by means of the image effect (figure 2.3). However, Fowler and Nordheim built their theory on the assumption that this effect is negligible in the case of a very strong electric field and at ordinary temperatures.

Within these assumptions, it is possible to study the tunneling through the potential barrier by solving the following wave equations [29]

$$\frac{d^2\Psi}{dx^2} + \kappa^2(W - C + Fx)\Psi = 0 \ (x > 0), \tag{2.1}$$

$$\frac{d^2\Psi}{dx^2} + \kappa^2 W\Psi = 0 \ (x < 0), \tag{2.2}$$

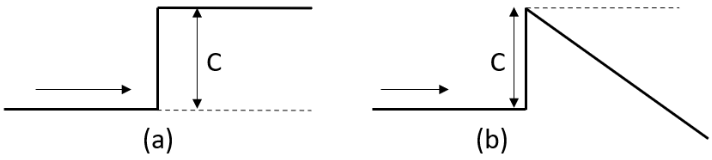

Figure 2.2: (a) Potential barrier in case of no external electric field and (b) in presence of external electric field.

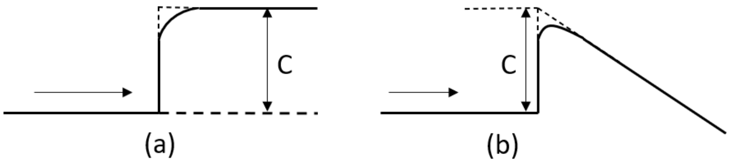

Figure 2.3: Potential barrier in case of no external electric field (i) and in presence of external electric field (ii) adding up the rounded top corners due to image effect [29].

taking also into account the continuity conditions for which Ψ and $\frac{d\Psi}{dx}$ are continuous at $x = 0$ and that for $x > 0$ the electrons would only move to the right direction. κ is a constant defined by $\kappa^2 = 8\pi^2 m/h^2$ [29].

By solving these equations it is possible to derive the fraction of electrons of given energy W tunneling through the potential barrier under the influence of the external field F. This solution represents the emission coefficient $D(W)$, which is found to be [29]

$$D(W) = \frac{4\{W(C-W)\}^{\frac{1}{2}}}{C}\, e^{-4\pi(C-W)^{\frac{3}{2}}/3F}. \tag{2.3}$$

Another important parameter is the number of electrons $N(W)$ incident on the surface of unit area per unit time with kinetic energy W. This was already previously calculated by Nordheim [32] starting from Sommerfeld's theory [29],

$$N(W) = \frac{4\pi mkT}{h^3}\, L\left(\frac{W-\mu}{kT}\right), \tag{2.4}$$

where

$$L(\beta) = \int_0^\infty \frac{dy}{e^{\beta+y}+1}, \tag{2.5}$$

here μ represents the classical Fermi energy or partial chemical potential of an electron distribution in the Fermi-Dirac statistics. Having these quantities defined it is now possible to define the current I as [29]

$$I = \frac{4\pi m\epsilon kT}{h^3} \int_0^\infty D(W) L\left(\frac{W-\mu}{kT}\right) dW, \tag{2.6}$$

with ϵ being in this case the electron charge.

In the case of low ordinary temperatures and high external electric field, and then using the expression of $D(W)$ as in 2.3, it is possible to obtain the general Fowler-Nordheim formula [29]

$$I = 6 \cdot 2 \times 10^{-6} \frac{\mu^{\frac{1}{2}}}{(\chi + \mu)\chi^{\frac{1}{2}}} F^2 \, e^{-2\cdot 1 \times 10^8 \chi^{\frac{3}{2}}/F}, \tag{2.7}$$

I is expressed in amperes per square centimeter of emitting surface, μ and χ are in volts, and F in volts per centimeter. Furthermore, all the numerical values of the constants have been inserted. Lastly, χ is given by $\chi = C - \mu$.

This expression was obtained at the limit of $T = 0$. However, it can be considered a valid approximation as long as μ/kt is very large [29].

The FN formula is most commonly represented as

$$J = (A\, E_L^2 \,/\, \Phi)\, exp(\frac{-B\,\phi^{3/2}}{E_L})\,, \tag{2.8}$$

where J is the current density, $A = 1.54 \times 10^{-6}\,\mathrm{A\,eV\,V^{-2}}$, $B = 6.83 \times 10^{9}\,\mathrm{eV^{-3/2}\,V\,m^{-1}}$, Φ is the work function of the material, and E_L is the local electric field at the emission surface [20, 26].

2.3 Murphy-Good theory

In 1956 Murphy and Good (MG) proposed a revised theory for field emission [33]. They managed to develop a theory that takes into account the thermionic regime, field emission regime, and intermediate region. With each of them being a particular case of a more general theory of electron emission [33]. Furthermore, they found a more precise field emission formula. The FN theory was known to be an approximation as it disregarded the image effect, as the contribution was assumed negligible [29, 34]. This was proved wrong by Burgess, Kroemer, and Houston (BKH), who proved in their study that it is not possible to disregard the image effect and therefore the rounding of the potential barrier (see figure 2.2). This rounded barrier usually takes the name of Schottky-Nordheim (SN) barrier [31, 35, 36]. For planar surfaces, the SN barrier makes the probability of tunneling higher by a factor between 250–500 [37]. Murphy and Good succeeded in finding a revised theory for field emission building on the results achieved by BKH [33, 35].

To derive the equation describing the general principle of electron emission from a metal a few basic equations need to be introduced. According to the free electron model, it is possible to write the number of electrons per second per unit area having energy within the range dW incident on the barrier as [33]

$$N(T,\mu,W)dW = 4\pi mkTh^{-3}ln\{1+exp[-(W-\mu)/kT]\}dW, \qquad (2.9)$$

where N is called the supply function, m is the electron mass, k is Boltzmann's constant, T is the temperature, h is Planck's constant and μ is the Fermi energy. Since energies are measured from zero for a free electron outside the metal, the work function ϕ can be considered as $-\mu$. W represents the energy for the motion normal to the surface $W = [p^2(x)/2m] + V(x)$ [33], with x being the coordinate normal to the surface and out of the metal, $p(x)$ is the electron momentum normal to the surface and $V(x)$ is the effective electron potential energy, which can be written as [33]

$$V(x) = -e^2(4x)^{-1} - eFx, \qquad when\ x > 0 \qquad (2.10)$$

$$, = -W_a, \qquad when\ x < 0, \qquad (2.11)$$

where $-e$ is the electron charge, $-e^2(4x)^{-1}$ is the image force contribution, $-eFx$ is the contribution from the external field F, and $-W_a$ is the effective constant potential energy inside the metal (figure 2.4). In figure 2.4 V_{max} represents the maximum value of the potential energy $V_{max} = -(e^3F)^{\frac{1}{2}}$ [33].

As for the case of the FN formalism, there is the need to introduce the probability that an electron incident on the barrier emerges from the metal, or in other words the transmission coefficient, hereby called $D(F,W)$ [33]

$$D(F,W) = \left[1 + exp\left(-2i\hbar^{-1}\int_{x_1}^{x_2} p(\xi)d\xi\right)\right]^{-1}, \qquad (2.12)$$

x_1 and x_2 are the points where $p^2(x)$ becomes zero and $p(x)$ is given by [33]:

$$p(x) = \{2m[W + e^2(4x)^{-1} + eFx]\}^{\frac{1}{2}}. \qquad (2.13)$$

The values of the limits of integration x_1 and x_2 strictly depend on the value of W. In the same way, the validity of equation 2.13 for $p(x)$ is also dependent on the value of W. In general, equation 2.13 will be valid for values of W below a certain limiting value $W_l = -\frac{1}{2}\sqrt{2}(e^3F)^{\frac{1}{2}}$ [33]. From these considerations, it is possible to determine the value of the transmission

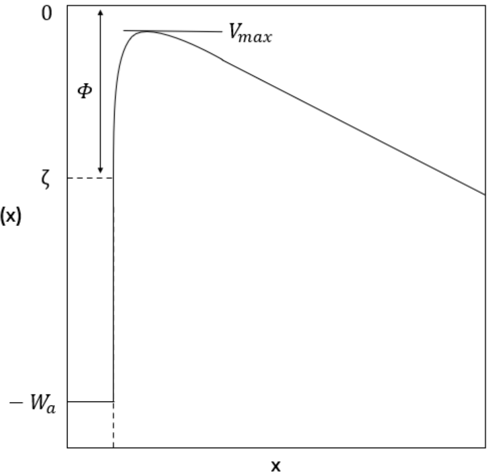

Figure 2.4: Potential barrier with the image effect contribution and names of the constants for MG electron emission calculations.

coefficient D depending on the value of W. In detail, it is given by equations 2.12 and 2.13 when $W < W_l$ and it es equal to one when $W > W_l$. The final expression for the transmission coefficient can be calculated by solving the integral in equation 2.12. The results achieved by BKH come here in place and permit to write the following revised expression for the transmission coefficient [33]

$$D(F,W) = \{1 + exp[(4/3)\sqrt{2}(F\hbar^4/m^2e^5)^{-\frac{1}{2}}y^{\frac{3}{2}}v(y)]\}^{-1}, \quad when\ W < W_l. \tag{2.14}$$

$$D(F,W_l) = 1, \ \ when\ W > W_l, \tag{2.15}$$

where $y = (e^3F)^{\frac{1}{2}}/|W|$ and

$$v(y) = -(y/2)^{\frac{1}{2}}\{-2E[(y-1)^{\frac{1}{2}}/(2y)^{\frac{1}{2}}] + (y+1)K[(y-1)^{\frac{1}{2}}/(2y)^{\frac{1}{2}}]\} \tag{2.16}$$

when $y > 1$,

$$v(y) = (1+y)^{\frac{1}{2}}\{E[(1-y)^{\frac{1}{2}}/(1+y)^{\frac{1}{2}}] - yK[(1-y)^{\frac{1}{2}}/(1+y)^{\frac{1}{2}}]\} \tag{2.17}$$

when $y < 1$. With K and E being two integrals of the type [33]:

$$K[k] = \int_0^{\pi/2}(1-k^2\sin^2\theta)^{-\frac{1}{2}}d\theta, \quad E[k] = \int_0^{\pi/2}(1-k^2\sin^2\theta)^{\frac{1}{2}}d\theta.$$

Here also comes the first important distinction among electron emission principles: the case $W > W_l$ corresponds to the case of thermionic emission.

It is now possible to calculate the general equation for the total electric current per unit area by integrating the product of the electron charge e, the transmission coefficient D, and the supply function N over all possible energies [33]

$$j(F,T,\mu) = e\int_{-W_a}^{\infty} D(F,W)N(T,\mu,W)dW \tag{2.18}$$

$$\begin{aligned} &= \frac{kT}{\pi^2}\int_{-W_a}^{W_l} \frac{ln\{1+exp[-(W-\mu)/kT]\}dW}{1+exp[(4/3)\sqrt{2}F^{\frac{1}{2}}y^{\frac{3}{2}}v(y)]} \\ &+ \frac{kT}{2\pi^2}\int_{W_l}^{\infty} ln\{1+exp[-(W-\mu)/kT]\}dW. \end{aligned} \tag{2.19}$$

For the case of high temperature and small fields (thermionic emission), the current can be obtained

$$j = \frac{1}{2}\pi^{-2}(kT)^2(\pi d/\sin\pi d)exp[-(\phi - F^{\frac{1}{2}})/kT], \tag{2.20}$$

where the term $d = \frac{F^{\frac{3}{4}}}{\pi kT}$ was introduced for sake of abbreviation and clarity. When d is so small that $\pi d/\sin\pi d$ can be replaced by one, hence in the case of very high temperature and very small field, equation 2.20 becomes the Richardson-Schottky formula [38].

Considering the field emission regime and therefore low temperature and high field it is possible to obtain the so-called MG field emission formula [33]

$$j = \frac{F^2}{16\pi^2\phi t^2}\left(\frac{\pi ckT}{\sin\pi ckT}\right) exp\left(-\frac{4\sqrt{2}\phi^{\frac{3}{2}}v}{3F}\right), \tag{2.21}$$

where the variable v is introduced as $v = e^{(W-\mu)/kT}$.

Finally, Murphy and Good found a solution for the current in the case of what they call the intermediate region [33]

$$j = \frac{F}{2\pi}\left(\frac{kTt^{\frac{1}{2}}}{2\pi}\right) exp\left(-\frac{\phi}{kT} + \frac{F^2\gamma}{24(kT)^2}\right), \tag{2.22}$$

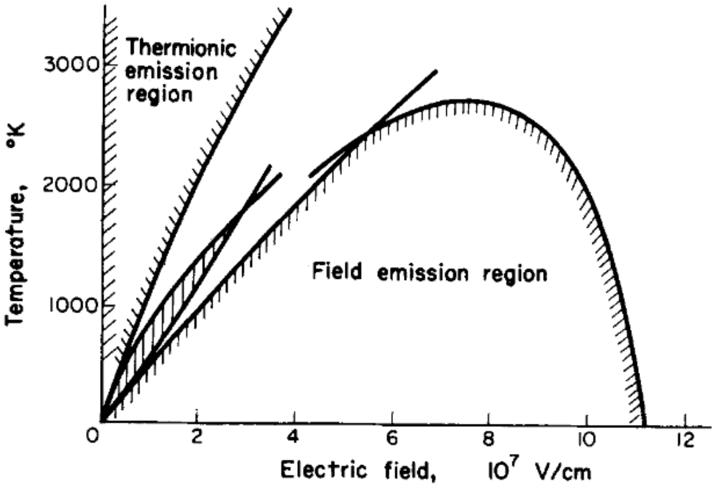

Figure 2.5: Regions of interest and region boundaries for the electron emission principles according to Murphy-Good theory [40]

where $\gamma = 3t^{-2} - 2vt^{-3}$ and $t(y) = v(y) - \frac{2}{3}ydv(y)/dy$.

In figure 2.5 the three regions of interest lie in relation to temperature and electric field for a material with a work function of 4.5 eV (comparable to tungsten). The discrepancies between FN and MG theories impact the intercept of the FN plot, while the exponential factor, or the slope, remains approximately unaltered for both theories [36, 37, 39].

2.4 Field emission in nano-structures

The theories presented so far are relative to a bulk material, in particular to flat metals. The MG model is recognized as the best to describe such a situation. However, when it comes to nanostructures such as nanotips and CNTs it is not possible to consider the MG model correct either. For instance, a CNT cannot be considered an infinite bulk material, as it is done for the derivation of the FN and MG formulas. The tip may not behave as a normal metal, meaning that the electrons would not be free and therefore the tip effect could become dominant. The CNT must be considered as a 3D structure which requires a first-principles study and a quantum mechanical approach to the problem [20, 41–43].

Several examples of deviation from the classical approach have been observed experimentally. Evidence is brought by the non-linear I-V characteristics in the FN plots and the saturation of the emitted current at high electric fields [20, 41–43]. As of the time of writing, there is no complete theory able to fully describe the field emission process in CNTs. However, a few theories and a few different approaches have been proposed such as the integration of time-dependent Schrödinger equation, the transfer matrix method, or semi-classical approaches [20].

2.4.1 Integration of the time-dependent Schrödinger equation

In this method [43] in order to simulate the field emission of nano-structures in a realistic way, no simplifying assumptions are used on either geometry, potential distributions, or electronic states. The tunneling probability is calculated by monitoring the time evolution of the wave function initially confined inside the emitter and therefore studying the transmission of the electrons from inside the emitter to the vacuum by tunneling through the potential barrier. The simulation of the CNT is to be done at an atomic level, but CNTs can reach considerable lengths and in such cases the simulation would not be feasible. The problem is solved by considering a short CNT whilst using the enhancement that a long CNT would exhibit. In this way, it is possible to include contributions from every atom in the simulation and at the same time simulate a long CNT. This model was used to approach several other problems connected with the field emission from CNTs, such as doping effect [44], oxygen effects [45], etc. [20, 43].

Another way to approach the problem is to solve the Schrödinger equation using the transfer matrix method. In this method bundles or arrays of CNTs can be evaluated by dividing the system into regions: perfect metal, part of the CNTs which experiences the external fields, and vacuum. With this method, it was confirmed that arrays and bundles emit less because of the screening effect [46]. Whilst Mayer et al. calculated the difference in emission between single and multi-walled CNTs. The results show that multi-walled CNTs are better emitters, especially when having a convex termination [47].

2.4.2 Semi-classical approaches

The semi-classical approaches are hybrid methods where part of the calculation is based on a first-principle quantum mechanical approach and another part of the calculation is instead addressed by means of classical approaches such as WKB-style approximations. In particular, the electronic structure of the nanotube tip is calculated at a three-dimensional quantum mechanical level, for the classical approach is unable to describe the behavior of the tips. While the transmission through the potential barrier and into the vacuum is evaluated by a WKB-style approximation. This type of approach has helped in understanding many properties of field emission from CNTs that depend on the chirality. For instance, it was found that the emission properties depend more on the energy gap than on the chirality itself [20].

2.5 Conclusions

Despite the fact that field emission was discovered almost a century ago, a comprehensive theory that can fully describe the process in detail is yet to be found. The main problems arise when it comes to describing field emission in presence of nano-tips or CNTs. This case often requires the use of numerical methods or simulations. The best results obtained so far involve the use of first-principle studies and quantum mechanical approaches in order to simulate the CNT or metal tip in detail.

In most experiments concerning field emission, the FN and MG models are still frequently used, despite the fact that the FN model cannot fully represent the experimental data. The MG model gets closer to evaluating the current values and therefore it is usually a better choice. The reason for the use of the FN model is mostly connected with the simplicity of the final formula. This makes it the choice in many studies where simple fits for comparisons are required.

Chapter 3

Carbon Nanotubes as Cold Electron Field Emitters

In this chapter, an overview, a formal definition, and a description of the main properties of carbon nanotubes (CNTs) are reported. Whilst in the first part of the chapter the general properties of CNTs are addressed, in the second part a more focused description of carbon nanotubes as cold electron field emitters is documented. The main field emitting properties of CNTs are reported as well as the parameters that affect the electron emission properties, such as maximum current output, emission stability, lifetime, and heating contribution during electron emission.

3.1 Introduction

CNTs are an allotropic form of carbon. They are hollow cylinders made of one or more graphene layers rolled in such a way as to produce a perfect tube. Perfect CNTs would therefore be made of a lattice solely composed of carbon atoms bonded to each other in order to form a hexagonal lattice. The only exception is represented by the closing caps which would be composed of hexagons to allow for bending and eventually for the closure of the tubes [20, 31, 48–50].

CNTs were first discovered by chance in 1991 by Iijima while working at NEC corporation in Japan [51]. He observed them while analyzing the carbon-soot produced by the arc-discharge method with Transmission Electron Microscopy (TEM); the arc-discharge growth method was already widely used for the production of fullerenes. Carbon nanotubes represented a total novelty being perfectly graphitized and being also closed at each end by means of half fullerenes [31, 49–58].

Since then CNTs attracted wide attention in many research fields thanks to the numerous theoretical unique properties attributed to them. In theory, CNTs can have an elastic modulus of about 1 TPa, and tensile strength of 100 GPa was measured for an individual CNT, made of several concentric layers. Such strength, for instance, is ten times higher than any commercial fiber. On top of this, CNTs have a density even lower than Aluminium, which makes them one of the lightest materials known so far [48, 52, 58].

An interesting property is that CNTs can be either metallic or semiconductive. In the case of metallic nanotubes, such as multi-walled CNTs, they can carry currents of up to dozens of A/cm^2. Furthermore, individual CNTs can have a thermal conductivity of 3,500 W m^{-1} K^{-1} at room temperature; this value would even exceed the thermal conductivity of diamond. Moreover, open nanotubes show capillarity which enables them to incorporate and take in metals or liquids; adsorption is also possible either into them or on their walls thanks to their nano-metric scale. This can lead to unlimited possibilities in various fields such as microelectronics, superconductivity, applications in the field of hydrogen adsorption and medium storage, and many more [48, 52, 58].

Most properties mentioned so far derive from the intrinsic features of single nanotubes. However, bundles, thin films, arrays, or bulk production of CNTs unlocks a series of additional unique properties which rely on either unorganized or organized CNT architectures such as near-ideal black-body adsorption and shape recovery to name just a couple [48–50, 58].

Finally, and most importantly for our investigations, carbon nanotubes show that they can emit electrons at relatively low applied electric fields, therefore paving the way to a new generation of field emitting materials, which is the main property addressed and used in this work. This particular property arises thanks to their geometrical shape. In fact, CNTs have a diameter in the order of a few nanometers, whilst they can reach heights in the order of some centimeters, which allows for a great field enhancement and consequently great field emitting properties [20, 23, 25, 26, 48–50, 58–62].

3.2 CNT types

A single-walled carbon nanotube (SWNT) is a graphene sheet rolled to form a cylinder, usually with a diameter ranging between 0.4–3 nm [52, 56]. Such range is similar to the diameter range of fullerenes, and in fact, half fullerenes are responsible for the nanotube closing. The length of a CNT can vary between a few μm to even a few cm [52, 53, 55, 56]. A CNT is made of a hexagonal lattice, a honeycomb lattice, of carbon atoms, each of them in the sp^2 hybridization so to form three bonds each [55, 56, 63]. Depending on how the graphene sheet is rolled over, it is possible to build different types of CNTs: arm-chair, zig-zag, or chiral.

The difference among them is given by the choice of the rolling axis relative to the honeycomb lattice and the radius of the closing cylinder. Both variables depend on the so-called chiral vector, C_h. The chiral vector is represented by a pair of integer indices, n and m (chiral indices); these two indices correspond to the number of fundamental translational vectors ($\boldsymbol{a}_1$ and $\boldsymbol{a}_2$) along two directions in the honeycomb crystal lattice of graphene,

$$\boldsymbol{C}_h = n\boldsymbol{a}_1 + m\boldsymbol{a}_2. \tag{3.1}$$

When $m = 0$ the nanotube is called “zig-zag”, when $n = m$ the nanotube is called “arm-chair”, whilst all other configurations are designated as “chiral”. See figure 3.1 for a representation of the chiral vector and figure 3.2 for a representation of the three different types of CNTs [20, 49, 50, 52, 53, 55, 56, 64].

In figure 3.1 it is possible to notice another variable: the chiral angle θ. θ is the angle between the chiral vector and the nearest zig-zag of C–C bonds. Arm-chair CNTs have a chiral angle of 30°; zig-zag CNTs have always a chiral angle of 0°; chiral CNTs have a chiral angle in the range 0–30°. Therefore, all CNTs have a chiral angle in this range. The remaining parameters in figure 3.1 represent:

- O and A connect the two lattice points defined by the chiral vector.
- **T** is called the primitive translation vector. It goes perpendicularly to the chiral vector starting from the origin point and stops at the first lattice point.
- B and B' are the lattice points that complete the rectangular strip that acts as unit of repetition of the CNT. Meaning that a SWNT has translational symmetry along the tube axis.

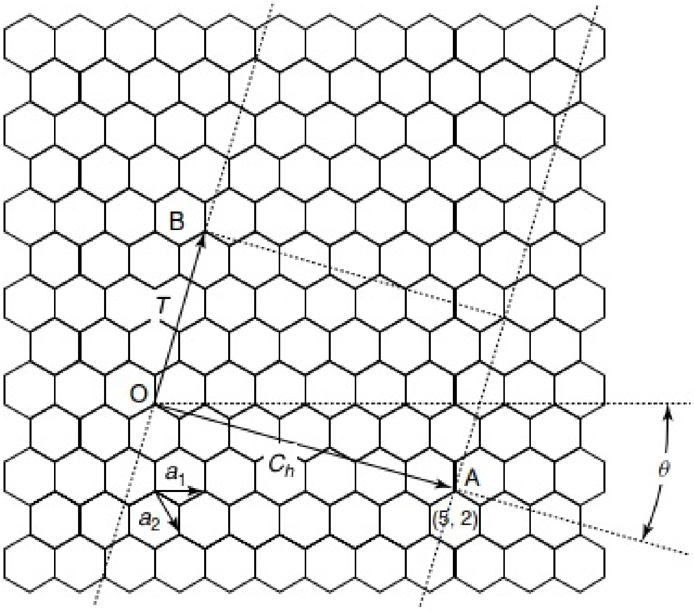

Figure 3.1: Graphene lattice and representation of the chiral vector [20].

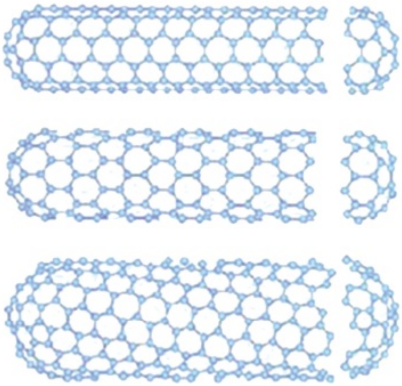

Figure 3.2: CNT types depending on the chirality. Top: Arm-chair, $n = m$. Middle: zig-zag, $(n, 0)$, bottom: chiral, $(n, m)\, m \neq 0$ [20].

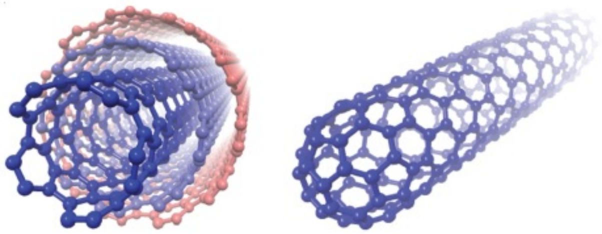

Figure 3.3: Illustration of a MWNT (left) and a SWNT(right) [26].

The CNT is finally obtained by cutting the graphene sheet through the points O and A, perpendicularly to the chiral vector [55]. In other words, OA, thus the chiral vector, represents the tube circumference. Therefore, from the chiral vector (and from OA) it is also possible to calculate the CNT radius $r = \frac{\boldsymbol{C_h}}{2\pi}$ [55].

3.2.1 SWNTs and MWNTs

CNTs can be composed of a single wall and therefore be called single-walled CNTs (SWNTs) or of multiple concentric walls, thus being called multi-walled CNTs (MWNTs). In figure 3.3 illustrations of both types can be seen and compared [26]. So far the simplest case of a SWNT was discussed, however, MWNTs have some additional properties which need further consideration. MWNTs can have a diameter that varies from a few nanometers up to several hundreds of nanometers depending on the number of walls [20, 55, 65]. The distance between two adjacent walls is always constant and it is about 0.344 nm on average, which roughly corresponds to the inter-layer distance of graphite planes [20, 55]. MWNTs, due to the presence of several planes, tend to be more aligned and also easier to produce, especially in bulk. They also usually present higher purity compared to SWNTs due to the growth mechanisms [50, 66].

3.2.2 Electronic structure and properties for different CNT types

CNTs can exhibit either semiconducting or metallic behavior depending on their chirality and on whether they are single- or multi-walled. Furthermore, in the case of semiconducting behavior, the band gap is strictly dependent on the chirality [20, 53, 55, 56].

For a carbon nanotube of infinite length, the electronic states are parallel lines in the reciprocal lattice, continuous along the tube axis and quantized along the circumference. The electronic nature of the carbon nanotube depends then on how the Brillouin zone is placed in relation to these electronic states [56].

- arm-chair CNTs, (m, m): there are always states crossing the corner points of the first Brillouin zone, meaning that this CNT type is metallic
- (m, n) CNTs of the type $m - n = 3 \times$ integer: only some electronic states cross on the corner point of the Brillouin zone. This would lead to a semi-metallic behavior, but in reality translates to a small-gap semiconductor due to the orbital rehybridization effect induced by the curvature necessary to close the tube. Both zig-zag and chiral CNTs lie in this category, depending on the m, n integers.

In figure 3.4 the electronic behavior variation of CNTs depending on the chirality and consequently on the overlap between Brillouin zone and electronic states is shown [56]. MWNTs can be considered metallic due to the presence of several concentric layers.

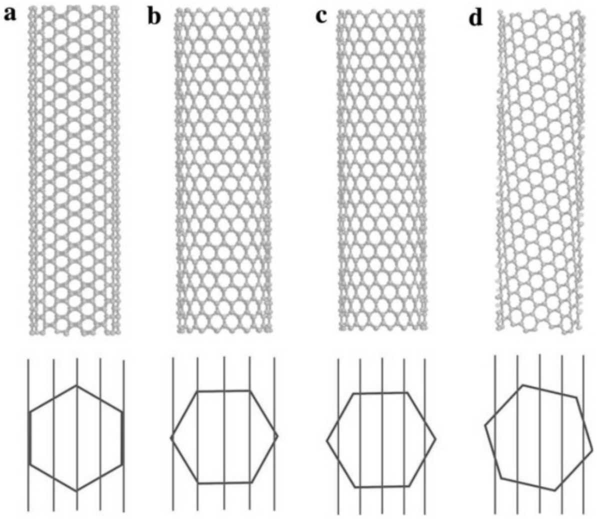

Figure 3.4: Illustration of how the chirality affects the overlap between Brillouin zone and electronic states in different CNTs. The hexagons represent the Brillouin zones for each CNT type and the vertical lines represent the electronic states. a) Arm-chair CNT $(10, 10)$: The central line crosses two corner points of the hexagon, resulting in a metallic CNT. b) Zig-zag CNT $(12, 0)$: the vertical lines touch the hexagon corners, but the CNT is semi-metallic with s small band-gap due to curvature. c) Zig-zag $(14, 0)$: semiconducting since the vertical lines miss all hexagon corners. d) As for c) this tube is also semiconducting [56].

3.3 Carbon nanotubes for electron emission

Several factors must be considered for using CNTs as electron emitters. Firstly, there is the need for a metallic contact in order to connect them to a power supply. The usual approach is to grow them onto a metallic substrate, or as in the most common case onto an n-doped silicon substrate.

Even considering the substrate constraints, the different possibilities regarding growth type and possible arrangements remain extremely diverse. Differences can arise from different factors or parameters:

- structural properties: SWNTs or MWNTs; diameter; length; open or closed cap
- chemical properties: impurities in the tube; defects
- density of the tubes
- orientation of the tubes

Literature can provide answers to a few of these points, but it is still hard to conclusively describe the interrelationship among all these parameters. The reasons for this are: difficulty of producing CNTs with no defects, their sensitivity to production technique and growth conditions, the presence of a very high number of degrees of freedom that makes the isolation of a single factor very challenging, etc. Finally, another important source for the discrepancies is the different experimental setups used in literature, each of them operating under different conditions, which makes it very hard to fully isolate the real results from the experimental limitations/conditions.

Bonard et al. presented a nice comparison study among SWNTs, closed-cap MWNTs, opened-cap MWNTs (all of these grown by arc-discharge method and then deposited as a film on a substrate) and catalytically grown MWNTs [67]. The comparison with catalytically grown MWNTs is not considered given the huge improvements in their production since the publication of this article. Nevertheless, it can give a very good idea of the differences between SWNT, closed-cap, and opened-cap MWNTs grown by arc-discharge and deposited to form a film. It was found that MWNTs tend to perform better, in particular closed-cap MWNTs. This is a result of a better purity obtained whilst growing MWNTs and that having several shells helps them to be more resistant. As for the better performance of the closed-cap MWNTs,

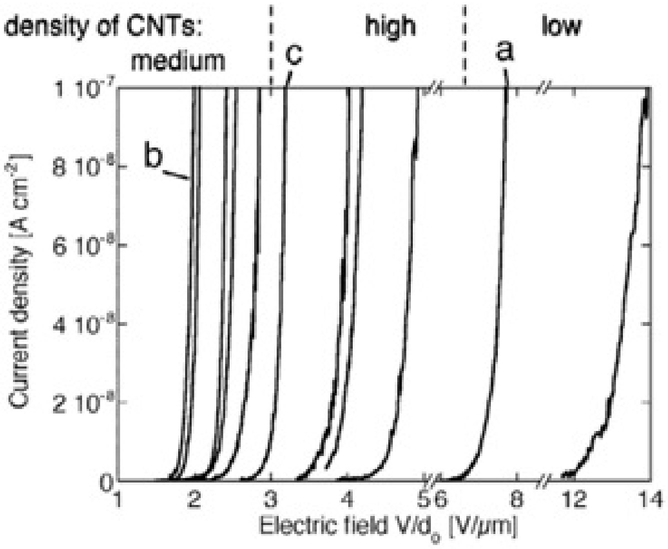

Figure 3.5: Field emission performance of CNT forests with different densities of emitters [68].

the explanation could be connected to the creation of emitting states at the cap that would not be present in the opened-cap case.

In [68] the effect of the density of CNTs in a forest on the emission performance is also studied and can provide some useful information. In this study, the density of the emitters is tuned varying the concentration of the catalyst promoting the CNT growth. The results are conveniently summarised in figure 3.5.

Figure 3.5 shows how the best performance is achieved with medium density films/forests. This can be explained by the screening effect which occurs when there are densely packed emitters. Electron emission in CNTs is enhanced by means of a field enhancement due to their whisker-like structure. However, when the nanotubes are densely packed, the field lines cannot fully penetrate, therefore limiting the field enhancement. In other words, the adjacent nanotubes act as a screen for the electric field, resulting in a poorer field enhancement and in a limitation of the emitted current. On the other hand, the overall emitted current also strongly depends on the number of emitters. The combination of these two factors explains how medium densities are the most beneficial for achieving the best emission performance.

In general, the best solution appears to be one involving aligned CNTs

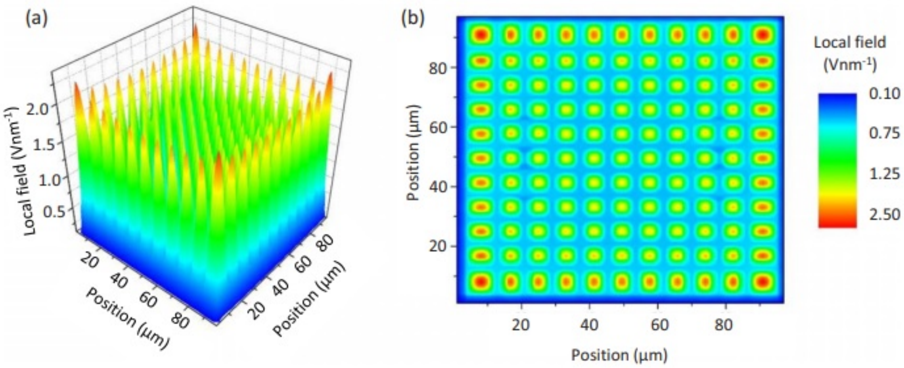

Figure 3.6: 3D simulation results showing the screening effect on a CNT array and highlighting the so-called "edge effect". a) shows a contour plot of the local electric field over an array of 11×11 CNT with a spacing of $S = h$. b) shows a top-down view of the same array [69].

perpendicular to a metallic substrate, having a good spacing for limiting the screening effect while also being packed enough in order to have a large enough number of emitters sharing the emission. Various studies have been reported which try to calculate the best spacing for limiting the screening effect [69, 70]. These studies also proved how the CNT height has to be taken into account. In fact, in order to limit the screening effect, it was found that the best distance is around three times the CNT height. In principle, a longer nanotube would emit more because of the higher geometrical field enhancement, but this assumption is no longer valid when going from a single nanotube to an array of nanotubes. In the array case, having longer nanotubes means that a larger spacing is needed for limiting the screening, which reduces the emitter density.

The screening will be higher for the CNTs in the middle of the chip and will decrease until almost disappearing at the edges. The edges, being scarcely screened by other CNTs, will in fact experience the higher field and therefore emit the most. This effect is well illustrated in figure 3.6 and it is usually referred to as "Edge effect" [61, 69].

Lastly, the degradation of the CNTs during emission must be considered. The nature of the degradation is not yet fully clear, but some of the causes that likely play a role are connected to the presence of residual gases in the emission area, which leads to phenomena such as; ion bombardment, ionization processes, and adsorption/desorption from the CNT tips [71, 72]. Studies on SWNTs and MWNTs at comparable base pressures show how MWNTs tend to be more resistant; SWNTs show a degradation rate that can be ten times higher. This behavior is attributed to the multiple shells of MWNTs, which makes them more robust [69].

3.3.1 Vertically aligned CNTs

At the moment, the best results from CNT field emitters are achieved with vertically aligned MWNTs, which are more stable and easier to produce. Moreover, patterned arrays of MWNTs permit finding a compromise between CNT length and inter-tube spacing [31, 61, 62, 73]. The most common technique to achieve this purpose is Chemical Vapour Deposition (CVD), either thermal or plasma-enhanced. Patterned arrays are CNT arrays where the catalyst is deposited with micro-metric precision in order to design a regular pattern. Many patterns have been tested during the last two decades, two that have provided some of the best performances are the squared-islands pattern and the hexagonal pattern. Both patterns allow for a good emitter distribution, with the hexagonal pattern being the one that allows for the best space coverage because of its geometrical features.

J. Sohn et al. [25] provided a good example of the results that can be achieved with a squared-islands array as shown in figure 3.7. This pattern is made of $30 \times 30\,\mu$m islands with a pitch distance (distance between two adjacent islands) of $125\,\mu$m. With such a pattern it was possible to achieve a peak of emitted current density of 80 mA/cm^2 with an applied electric field of 3 V/μm. The chip size in this case was 1 cm × 1 cm while the CNT height was $8\,\mu$m.

In [24] another array type is presented. This is a hexagonal array and the chip studied had an emission area of 4×4 mm^2 and a CNT height of $10\,\mu$m. With this array, a current density of 1 mA/cm^2 was reached at 1.5 V/μm and the current density peak value achieved was 1.5 A/cm^2. In this case, the width of the CNT walls was only $1\,\mu$m in order to enhance the edge effect and achieve extremely high current densities. Scanning Electron Microscope (SEM) images of the structure are reported in figure 3.8.

The edge effect clearly affects the emitted current, however, the presence of many empty areas in the chip implies a smaller number of CNTs and this can greatly affect the long-term performance. This also means that each CNT would emit a much larger current which translates into a higher temperature

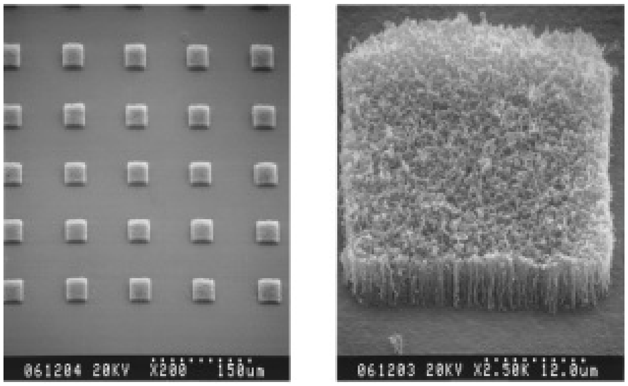

Figure 3.7: SEM images of a squared-islands array. Left) top view of the pattern. Right) Top view of a single island [25].

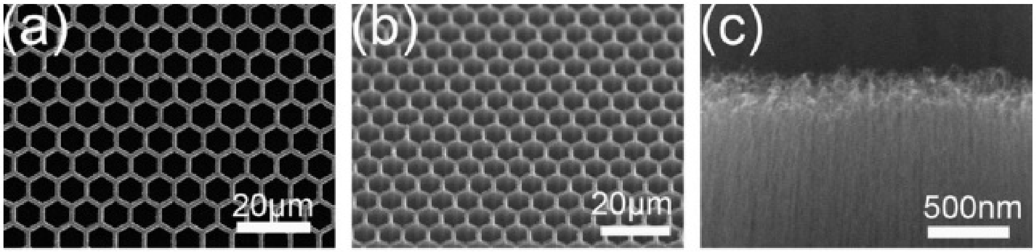

Figure 3.8: SEM images of the hexagonal array. a) top view, b) tilted top view, c) transverse view [24].

of the emitters, caused by Joule effect [20, 74], and consequently in having emitters much more affected by adsorption/desorption of impurities.

3.3.2 Heat generation

The heat generation in CNTs during emission was studied in [20, 74]. The main contribution derives from Joule heating activated by the current emission. It is clear in these references that the temperature of the CNTs is strictly dependent on the emitted current. In [74] the nanotube is treated as a resistance, which is justified, especially in the case of MWNTs grown via CVD. In high-quality SWNTs this assumption may not be fully valid because of the appearance of additional effects such as ballistic transport where thermal and electrical conductivity becomes more complicated to analyze. Within this assumption, the Joule heating during field emission is studied considering the CNT as a one-dimensional object of length L in contact with a heat sink at a fixed temperature. Heat losses through the cap of the CNT are also included. The result is:

$$\Delta T_A = \frac{\rho}{2\kappa}\frac{L^2 I^2}{\pi^2 r^4}, \tag{3.2}$$

where T_A is the temperature at the apex of the CNT and κ is the thermal conductivity. Equation 3.2 is obtained by introducing the resistivity ρ, $R = \rho L/A$, and using the cross-section of the outside tube, $A = \pi r^2$. This formula is useful to highlight how the temperature arising in the CNT scales with parameters such as the CNT radius r ($\propto r^{-4}$), the CNT length L ($\propto L^2$), and the emitted current I ($\propto I^2$). This suggests that extremely long and thin CNTs may not be the best solution for cold field emission since this would also imply a much higher heating limiting high current emission.

Simulations of the temperature profiles for a 40μm-long CNT with a radius of 10 nm emitting different amounts of current have also been performed in [74]. The diagrams are shown in figure 3.9.

What is also possible to infer from figure 3.9 is how the temperature contribution becomes evident starting at emitted currents in the order of hundreds of nA. This means that limiting the current emitted from a single CNT to values in the order of a few nA or hundred pA would keep the temperature contribution to negligible values [20, 74, 75].

A further contribution to the heating of CNTs during emission is represented by the Nottingham effect [20, 30, 74]. The emitter can be heated

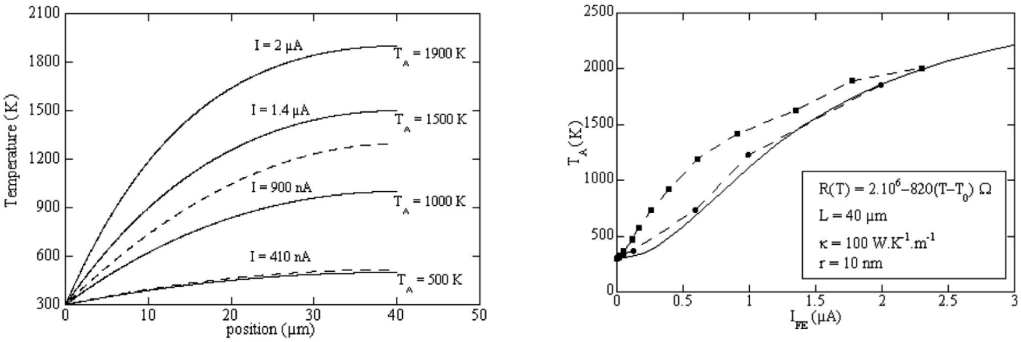

Figure 3.9: Left: temperature profiles along a 40μm-long CNT for different currents. The parameters used are listed in the right figure. Right: Simulation of the temperature at the apex of the CNT vs emission current [74]. The dashed lines in this case show the experimental values for two runs of an additional study made in [75].

or cooled depending on the difference between the average energy of emitted and replaced electrons. At low temperatures, close to 0K, the energy of emitted electrons is less than the Fermi energy, leading to heating. If the temperature is higher than the inversion temperature, the electrons at energy levels above the Fermi energy are preferentially participating in the emission, leading to cooling. Therefore, the Nottingham effect can either cool or heat the CNT structure [76].
When the emitted current density and the electric field are high, the emitted electrons have a temperature higher than the electron coming from the circuit to replace them. In this case, the Nottingham effect leads to cooling. However, this effect becomes negligible when the temperature due to Joule heating becomes dominant [20, 30, 74, 76].

At low emitted current densities and relatively low electric field, as in the case previously discussed, the Nottingham effect is negligible [30, 74].

3.4 Conclusions

A careful choice of the array type is vital and greatly depends on the use-case. Maximizing the edge effect, thus limiting the screening effect, permits reaching the highest emitted current densities. Having a large number of CNTs sharing the emission allows for better stability and lifetime. For this

Ph.D. thesis, stability and lifetime are the parameters which can most greatly affect the use of a CNT cathode in operation. Thus, the choice of the CNT arrangement must lean towards a high-density patterned forest of vertically aligned CNTs.

Furthermore, a factor that has to be carefully considered is the availability of CNT arrays. In fact, having reproducible arrays and easily available in case of necessity for both operation and testing is of great importance. Hence the focus of this research has to be directed to products that are accessible and already produced at a commercial level.

Another aspect to consider is the limitation of temperature contributions. The research on this field [20, 74, 75] highlights that the heating contribution in CNTs becomes significant only when the current emission is higher than hundreds of nA per tip. When using a large area cathode with a high density of CNTs, and considering the current output required in this PhD theses, e.g. a few mA, a current density of the order of some mA/cm^2 suffice. This means that single CNTs would emit currents of the order of hundreds of pA, or even less when considering emission areas in the order of a few cm^2. In such a regime the temperature contribution appears negligible.

CNTs prove to be a very interesting material for achieving cold electron emission for many additional use-cases. They have proved to be able to emit current densities as large as 1 A/cm^2 [20, 23, 24] and the stability seems to be matching the requirements of this research in the short term. Further characterization of long-term stability and lifetime are however essential to test the feasibility of using them in ELENA and for most purposes.

Chapter 4

Characterization of the current emission and conditioning process of field emitting CNT arrays

In this chapter, an overview of the experimental setups used in this thesis is given and the results obtained are then discussed in detail. The experimental work was divided into several parts. The first set of experiments was devoted to investigating the emission stability and emission lifetime of several CNT cathodes. For this purpose a vacuum tank was assembled and an ad-hoc experimental apparatus was designed and consequently constructed. This setup was called the Cold Cathode Test Bench (CCTB).

A further set of measurements was then focused on the characterization of the features of the CNT arrays. These were investigated using several experimental techniques:

- Scanning Electron Microscopy (SEM) for imaging and visual characterization of the arrays
- Secondary Electron Yield measurement (SEY) and
- Ultra-violet Photoelectron Spectroscopy (UPS) for work function evaluations
- X-ray Photoelectron Spectroscopy (XPS) for chemical characterization

- Residual Gas Analysis (RGA) for studying the out-gassing during bake-out

These tests served to determine the main properties of the CNT arrays, to assess the best way to handle and efficiently exploit the full potential of these cathodes. This was achieved through a conditioning process that allows them to perform at their best without contamination deriving from the emission environment or from within their structure due to the growth process.

The last part of the experimental work aimed at testing the current switching capabilities of the CNT arrays. This was mostly coupled with the previous experimental setup (CCTB) with the only exception of a hardware switching box developed in-house for this purpose.

4.1 Methods

4.1.1 The Cold Cathode Test Bench

The main experimental setup, shown in figures 4.1 and 4.2, consists of a CNT array acting as the cathode and a molybdenum plate acting as the anode where the electron beam is collected and measured. Therefore operated in diode configuration. Figure 4.1 shows a photograph of the the setup, with a detailed illustration of the stack presented in figure 4.2. The setup is placed in a vacuum chamber with three flanges dedicated to sample hosting. Each flange can host up to three samples, as shown in figure 4.1, translating to a maximum capacity of nine samples. Each sample is independent from the others and can have a diameter of up to 45 mm.

The flanges have undergone a few iterations over the course of the thesis work. In the current version the distance between the cathode and anode is set to approximately 800 μm and a mica insulating plate is placed on the top of the cathode to avoid contributions from the cathode edges. Additionally, the mica plate acts as a mask, having a fixed aperture which permits precise control of the emitting area, as shown in figure 4.1(b).

Each sample stack is made of:

- a copper support that acts simply as a holder for the whole structure,
- a Vespel™or mica insulating plate,
- a Stainless Steel (SS) plate as sample holder,

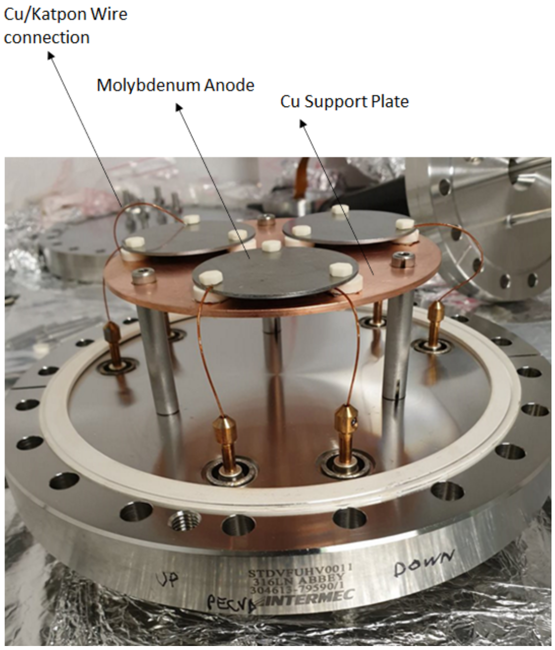

(a) Fully assembled flange with three samples in diode configuration.

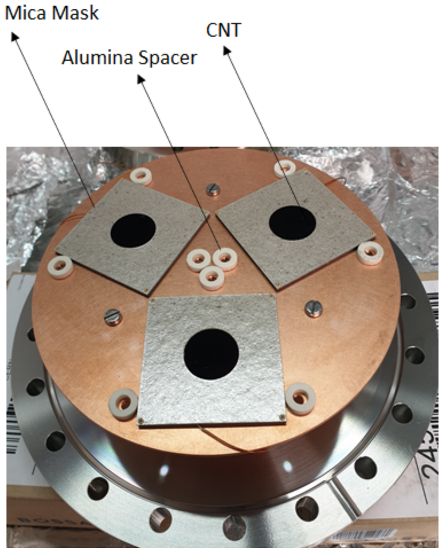

(b) Partially assembled flange and CNT samples arrangement

Figure 4.1: Cold Cathode Test Bench 1.

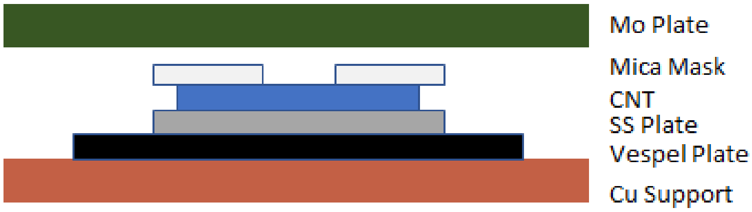

Figure 4.2: CNT Sample stack layout. Sizes are not to scale.

- an n-doped silicon substrate with the CNT array,
- a mica insulating mask,
- a molybdenum plate acting as anode.

The SS plate allows for electrical connections to be made, with the stack being held together by means of PEEK (PolyEther Ether Ketone) insulating screws. Except for the molybdenum plate, which is fixed directly on top of the copper support using ceramic screws and washers.

The electrical connections are realised with copper/Kapton™wires; one connected to the SS plate and the second to the molybdenum plate, as shown in figure 4.1. Both wires are then connected to SHV (Safe High Voltage) coaxial feedthroughs in order to provide a secure high voltage connection outside of the vacuum. To produce the electric field a negative voltage is applied to the cathode using an ISEG HPn-120256 power supply [77] with a maximum voltage of -12 kV. The current measurements are made at the anode side, which is grounded, using a Hameg HM8012 programmable multimeter [78] with resolution of 1 μA. The samples used are all relatively large in size, meaning that currents from hundreds of μA up to several mA can be extracted.

As this is a bespoke setup it has undergone several changes throughout the period of this work. Several arrangements and several materials were tested before reaching the final setup illustrated above. Some of the main upgrades involve the use of a conductive silver glue to fix the CNT sample on the SS plate. This ensures a good and stable positioning of the sample and even more importantly ensures a good conductivity between the SS plate and the CNT chip. The mica mask was also not included in the first setup, its purpose is to delimit the emission area with improved precision and at the same time eliminate possible contribution from the silicon substrate sharp edges.

Such sharp edges had also caused some electrical breakdowns that were then mitigated via the mica mask. The choice of the molybdenum plate arose after the use of a copper foil, which faced a few issues such as burning of the foil surface most likely due to oxygen contamination. Molybdenum instead proved to be an optimal choice because of its great electrical conductivity, enhanced heat conductivity due also to the more bulk nature of the upgraded anode and low coefficient of expansion making it more stable when compared to copper. In this case, there is the need to apply high voltages between two electrodes which are only some hundreds of microns apart, at the same time all parts are required to be Ultra High Vacuum (UHV) compatible. This implies a number of constraints that cannot be avoided. Thus, this experimental setup required an iterative development period, although in its final version has proved to be very solid and reliable, while at the same time being UHV and HV (High-Voltage) compatible.

For the data acquisition LABVIEW [79] routines were used, both for DC operation and for a software-driven switching mode. The pressure in the vacuum chamber is monitored with a Pfeiffer full-range vacuum gauge [80] able to measure pressures from 1×10^{-9}–10^{3} mbar.

A bake-out system has also been assembled on the top of the vacuum tank. It consists of heating jackets mounted around each flange and heating tapes mounted all around the tank. The whole system is then covered with aluminum scotch tape and aluminum foil, which provide for the required temperature insulation of the system. The whole system is shown in figure 4.3. Initially the bake-out system was not a part of the experimental setup. However, after several tests, the setup was upgraded for including it. Its addition permits the cleaning of the emission region and the samples' surfaces making the conditioning process of the samples faster and safer, whilst at the same time enhancing the stability and lifetime properties of the CNT arrays.

Finally, the pumping system consists of an Edwards pumping group [81], which includes a dry primary pump and a turbo pump. With this system and with a thorough cleaning of each part it is possible to reach pressures below 10^{-9} mbar [21, 22].

4.1.2 CNT arrays

Two types of CNT arrays have been characterized in this study: a honeycomb-like array (CNT1) and a squared-islands array (CNT2). Both geometries were characterized and validated with SEM before operation. Figure 4.4

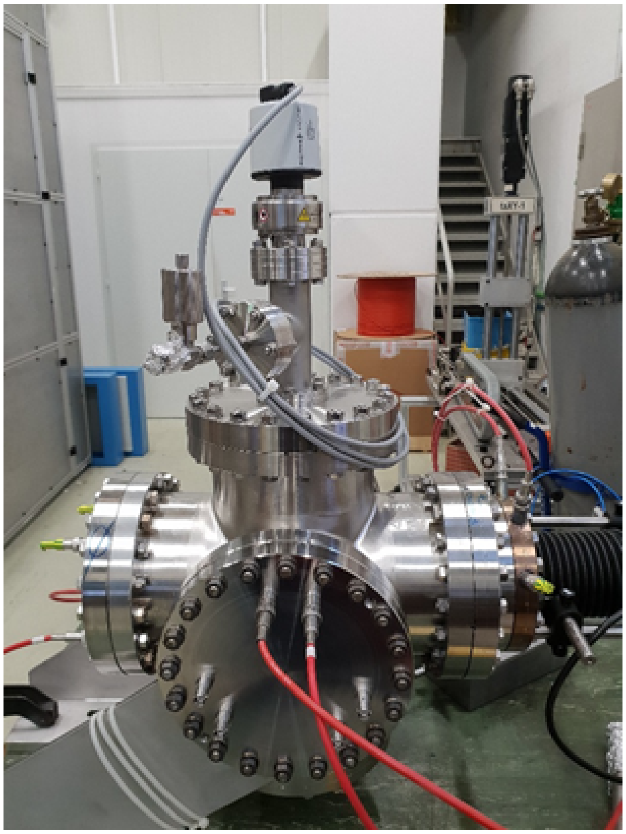

Figure 4.3: Photo of the Cold Cathode Test Bench (CCTB).

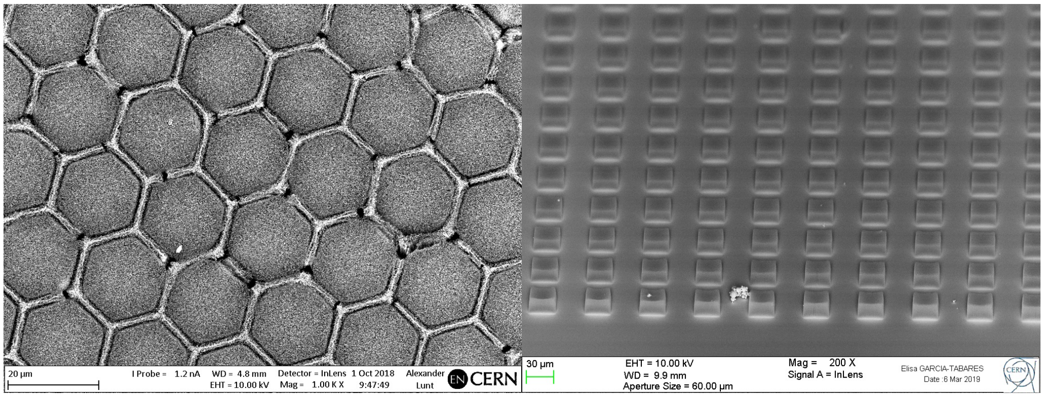

(a) (b)

Figure 4.4: SEM images of the honeycomb-like array CNT1 (a) and squared-islands array CNT2 (b).

shows the scanning electron micro-graphs of the two arrays. In both cases the CNT height is of about 50 μm. The honeycomb-like pattern is made of an array of hexagons with side size of 10 μm and spacing between hexagons of 5 μm. The CNTs, also visible in figure 4.4, are placed inside the hexagons, while the channels separating the hexagons are empty. The squared-islands array pattern is made of 30 μm $\times$ 30 μm squares, with a spacing of 30 μm. In this case, the CNTs constitute the squares while the channels between the islands are empty. The samples have been purchased from an external commercial supplier, Nanolab Inc. [82]. All samples were grown using Thermal Chemical Vapour Deposition [83] using a combination of aluminium and iron as catalysts to promote CNT growth.

These patterns have been selected in order to limit screening effects, thus increasing the emitted current density, while still having a large number of emitters participating in the emission [21, 22]. The two arrangements, hexagonal pattern and square pattern, are the configurations which grant the best space coverage, thus permitting to have a large number of emitters and at the same time include appropriate spacing in order to minimize the screening effect and enhance the emission properties.

4.1.3 Scanning Electron Microscope

The SEM used is a Zeiss XB540 FIB-SEM [84]. This was used in collaboration with the EN-MME-MM section at CERN which is the reference section for microscopy analysis.

A SEM is a type of electron microscope that produces images of a sample by scanning the surface with a focused beam of electrons. The electrons interact with atoms in the sample, producing various signals that contain information about the surface topography and composition of the sample. The electron beam is scanned in a raster scan pattern, and the position of the beam is combined with the intensity of the detected signal to produce an image. In the most common SEM mode, secondary electrons emitted by atoms excited by the electron beam are detected using a secondary electron detector. The number of secondary electrons that can be detected, and thus the signal intensity, depends, among other things, on specimen topography [85].

FIB-SEM adds a further functionality. FIB stands for Focused Ion Beam and it enables the milling of the sample's surface for a few nanometers or micrometers [86]. It is a very powerful tool when measurements of a sample's cross section are required. This functionality was used for measurements of the CNT height as part of the sample characterizations.

4.1.4 Techniques for vacuum characterization of the CNT arrays

SEY, UPS and XPS were performed in collaboration with the surface treatments group at CERN. With these experimental techniques measurements of the CNT arrays' work function (SEY [87] and UPS [88]), study the chemical composition of the samples (XPS [89]) and monitor the out-gassing during annealing cycles were possible ([90]).

A commercial UHV system, with a base pressure below 2×10^{-10} mbar (SPECS, Surface Nano Analysis GmbH, Berlin, Germany [91]), was used for SEY, XPS and UPS characterization of CNT samples on silicon. The system consists of a hemispherical electron energy analyzer (Phoibos 150 [92]) with nine channeltrons, a monochromated AlKα X-ray source (XR50 M with Focus 500, $h\nu = 1486.7\,\mathrm{eV}$), and a noble gas discharge source that was operated with He (UVS 10/35, $h\nu = 21.2\,\mathrm{eV}$). The energy scale of the analyzer is regularly calibrated using sputter-cleaned polycrystalline copper, silver, and gold foils. For analysis of the SEY between 0 and 1800 eV primary electron energy, an electron beam of ~ 2 nA generated by a Kimball Physics ELG-2 electron gun [93] at a distance of 2 cm to the sample was focused to a spot diameter of 1 mm on the surface. A sample bias of ±47.1 V was used. The details of the setup and the implemented experimental conditions are described in further detail in reference [21, 94]. If not otherwise specified, the primary electrons impinge the sample at normal incidence.

SEY

The SEY setup consists of an electron gun (ELG-2/EGPS-1022 from Kimball Physics [93]) and a sample holder, on which the sample current I_{sample} is measured.

The SEY is measured using the following approach:

1. A positive voltage is applied to the sample. All primary electrons (PE) impinging on the sample surface are collected by the sample and the emitted secondary electrons are recaptured by the sample itself.
   → I_{sample} can be therefore assumed to be the primary current I_{PE} from the electron gun.

2. A negative voltage V is applied to the sample. All emitted secondary electrons (SE) are accelerated to leave the sample surface, i.e., I_{sample} measures the flux of electrons through the sample.
   → The current of secondary electrons is $I_{SE} = I_{PE} - I_{sample}$.

3. The secondary electron yield SEY $\delta = I_{SE}/I_{PE}$ can be calculated from those two measurements

In this way it is possible to calculate and plot the SEY as a function of the primary electron energy and get the so-called SEY-edge. Then, the derivative of the SEY-edge was fitted by a Gaussian function to determine the inflection point.

Subsequently, a sputtered Au foil was used as reference material for the work function analysis. For the Au reference, a work function of 5.3 eV was considered and the shift of the inflection point for the other samples was used to determine their work function.

Analysis of the surface composition

For analysis of the surface composition XPS was performed. XPS was measured in the CERN's surface analysis experimental setup (from SPECS). The chamber pressure during measurement was of about 9×10^{-10} mbar, with the samples at room temperature. This method allows a quantitative distinction of the chemical composition in the near surface region. Monochromated X-rays are used to irradiate the sample surface and the spectral distribution of emitted electrons is detected and analyzed (photoelectric effect). Using X-rays, mainly strongly bound electron states are characterized, which give information about chemical composition and bond configuration of the incorporated atoms. The detection limit is element-dependent, but it roughly is 0.1 atom%, i.e. the percentage of one kind of atom relative to the total number of atoms (1000 ppm). All elements except hydrogen and helium are accessible. The depth of information for inorganic materials is limited to 5–7 nm from the outermost surface for the used excitation energy. The parameters of the analysis are:

- analysis of the photoelectrons perpendicular to the surface (normal emission)
- constant pass energy of 50 eV for survey spectra, 30 eV for detailed spectra
- analysis area of ~ 1 mm in diameter
- the sample was grounded

Ultraviolet Photoelectron Spectroscopy was used operating the same electron analyzer used for XPS analysis [88]. UPS was used for further measurement of the samples' work function as a cross check method.

4.1.5 Current switching system

The electron gun of the electron cooler in ELENA needs to be switched on and off in order to follow the cooling plateaus imposed by the beam cycle. While the speed of the switching is not a crucial point, it is important to test whether a CNT-based cathode can be switched on and off repeatedly with rise and fall times below 1 ms without strong perturbations of the current between cycles. In order to test the CNT current switching behaviour a hardware switching system was designed and coupled with the CCTB. The switching system was designed using a BEHLKE ([95, 96]) push-pull switch of the model series HTS. HTS transistors are made up of a large number of MOSFETs (Metal-Oxide Semiconductor Field-Effect Transistors), lying parallel and in series, which are combined in a compact, low-inductance bank. Furthermore, they are controlled absolutely synchronously via a special driving circuit within their case [96].

The remaining components of the circuit have been chosen partly by following the switch's application notes and partly empirically in order to be best suited to the specific case and to the requirements concerning current output and operating voltage.

The Behlke switch used had a maximum operating voltage of 2 kV, which was enough for testing the cathodes with a current output in the range of dozens/hundreds of μA. The choice of limiting the operating voltage to 2 kV sets a limit on the extracted current. However, there are several motivations which led to this decision. First, the possibility of using a switch that was already used in other applications and for which the necessary connections, supplies and know-how were promptly available. Second, electronic components with low inductance and able to withstand very high voltages are usually non-standards and non-trivial to acquire, which translates into time and cost related constraints. Third, the current output does not represent a problem whatsoever when operating this type of switches, since they can withstand currents in the order of Amperes. Therefore, the use of currents in the order of mA does not represent an obstacle to the use of such switches. Lastly, the cost of the necessary equipment for testing the switching mode at higher operating voltages, e.g. $\sim$ 10 kV, would greatly outweigh the benefits in terms of research findings and consequently does not justify such an investment at a testing stage.

For the ELENA beam cycle the switching rise and fall times required are in the order of 1 ms and the switching frequency required is in the order of less than 1 Hz. However in this study the tests on the CNT cathodes were performed for rise and fall times down to μs and operating frequencies up to 10 Hz. In such a way it was possible to both stress-test the cathodes and pave the way for alternative applications.

The schematic of the switching circuit is shown in figure 4.5.

The value of the electronic components have been chosen according to the switch data-sheet and via empirical studies. C_1 is a low-inductance capacitors stack composed of two capacitors, each having a capacitance of $1.5\,\mu$F, for a

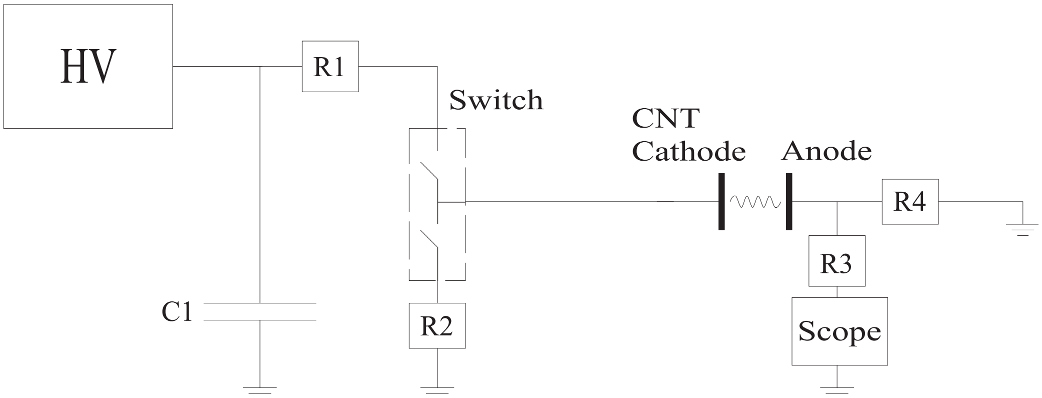

Figure 4.5: Schematic of the switching circuit used to pulse the CNT cathode.

total of 3 μF. This capacitor has the goal to buffer the high-voltage supply. This prevents dangerous flyback voltages and allows for fast charging and discharging of load capacitors, such as the CNT diode. R_1 and R_2 are low inductance series resistor, they permit matching of the impedance between the switch, line and load. Their value, partly according to data-sheets and partly empirically, was set to 50 Ω. All the electronic components mentioned so far are on the cathode side and are part on the high-voltage side of the circuit. The remaining parts, on the anode side, do not experience high-voltage, since the anode is grounded. The anode part of the circuit has the goal to convert the current extracted from the cathode in a potential that can be measured using a digital oscilloscope. As this side of the circuit is not experiencing a high voltage, all remaining components are standard low-voltage components.

These electronic parts served to realise a shunt resistance, which is connected in parallel to the oscilloscope so that the entire current generated by the CNT cathode flows through it and generates a voltage drop. This voltage drop is then measured using the oscilloscope. R_3 is set to 1 kΩ in order to safeguard the shunt and allows for precise measurements. R_4 is set to 1 kΩ and represents the shunt resistor. The value of the shunt resistor is then used for calculations of the current via the Ohm's law, starting from the voltage drop that is measured on the oscilloscope. An additional resistance, which will be hereby named R_5, is set to 50 Ω within the oscilloscope and directly through the oscilloscope software. This serves to protect the oscilloscope and avoid reflections.

The high-voltage power supply used is a ISEG HPn 120256 [77], which is able to generate a negative voltage up to 12 kV. The oscilloscope used is a Rohde&Schwarz RTO 1024 [97] with frequency up to 2 GHz and sampling rate up to 10 GSa/s.

The push-pull switch is a Behlke HTS 61-01-HB-C which is connected on one side to the power supply and the other side to the ground. In this way it can switch between high-voltage and ground. It is powered and operated using a signal generator (Agilent 33220A [98]) which enables square-wave signal generation and a power supply DELTA ELEKTRONIKA ES-030-10 [99] set to 5 V to power the system.

All the connections, made with high voltage cable, were devised to be as short as possible in order to limit delay times and arise of some parasitic capacitance and antenna effects.

4.2 Results and discussion

This section details the research conducted using the CCTB. These tests were conducted on several samples and led to the final sample choice and on assessing whether CNTs can be eligible candidates to be used in operation in the ELENA electron cooler's electron gun. The first part of the work focused on a literature study aimed at selecting two possible CNT array types. The choice was based on selecting the array types which were showing the best performance in terms of emitted current and emission stability. At the same time array types that were more common in the literature were a focus as this indicates an overall success of an array type and a better literature base to start upon.

Once the two arrays were selected, the focus switched to their characterization based on the requirements of the ELENA electron cooler, i.e. good emission stability, long lifetime and the optimal conditioning process required to achieve repeatable and optimal performance.

All the tests served to single out the best array type, on which subsequent studies focused. A part of the tests was performed in DC mode at different emitted current values to assess compliance with the gun requirements, e.g. current fluctuation of less than 5%. Further tests were then performed in current switching mode, in order to comply with the ELENA beam cycle. These new studies also served as a comparison with the results previously achieved without proper conditioning. Moreover, an in-depth surface analysis of the samples was performed to evaluate the benefits of the conditioning process and further characterize the samples.

4.2.1 Lifetime and stability measurements

The characterization of several honeycomb-like (CNT1) and squared-islands (CNT2) array types started with a conditioning and stability test at fixed field before the voltage was slowly ramped up. Initial tests on several samples showed that rapidly increasing the electric field, and therefore the emitted current abruptly, causes severe damage on the CNT samples, which in turn led to a fast burn-out of the initial samples. For this reason, the tests on the samples started at low field for several hours to test their stability step-by-step while monitoring the current adjustments and the vacuum level changes during emission. These initial procedures as well as the results from vacuum monitoring showed that the emitted current is strongly dependent on the vacuum level and vice-versa which is shown in figure 4.6. This can be partly explained by the shortening of CNTs during current peaks and by out-gassing. Other important factors are ion bombardment and residual gas ionization, these effects become dominant when (i) the pressure is not low enough, (ii) there is high concentration of residual gases in the emission area, (iii) there is significant contamination of the emission surface [71]. As a result, the current emission can be significantly affected leading to breakdowns, thus affecting the stability of the emission and in some cases altering the field emitter tips. This also disrupts the field emission properties of the material and leads to severe degradation. These last two factors also play a major role in affecting emission stability and lifetime. Most of these phenomena act in a cause and effect dynamics. This means that in some cases the deterioration of the CNTs depends on the pressure, due to ion bombardment and out-gassing inducing shortening of the CNTs and arcing. In other cases the pressure depends instead on current spikes, arcing and out-gassing too. To limit these cause and effect dynamics, thus ensuring a stable emission, a good vacuum and a slow conditioning process are essential. For instance, a slow conditioning process with gradual increase of the electric field (and consequently of the emitted current) is also beneficial to shorten, and/or burn, protruding CNTs that can alter the overall cathode performance affecting the emission stability.

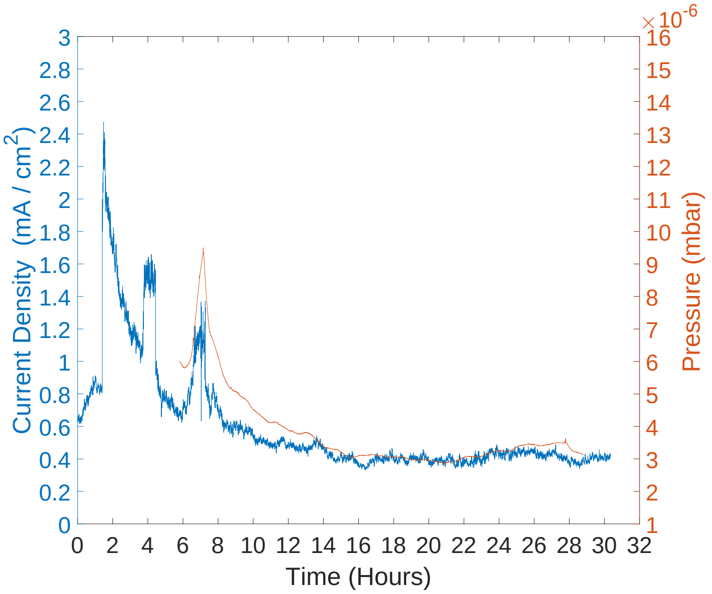

(a)

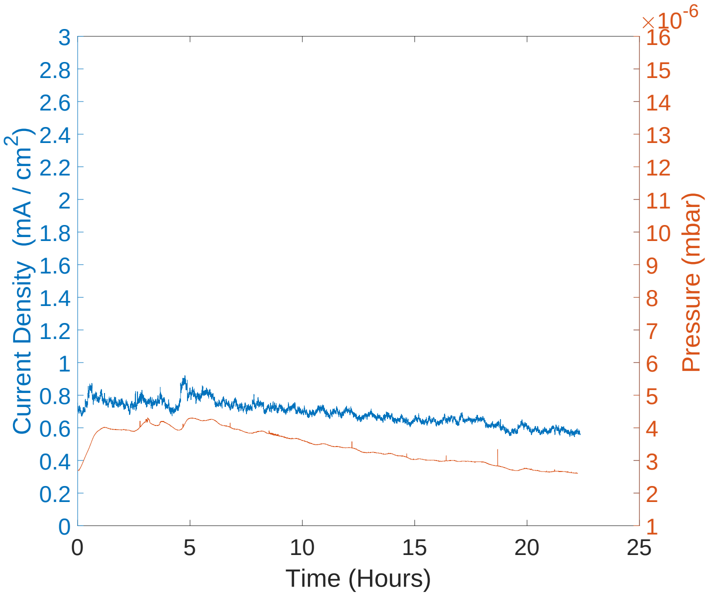

(b)

Figure 4.6: Conditioning test for CNT1-type array. Current density and pressure as a function of time for field $E = 1.94$ V/μm (a), and $E = 2.4$ V/μm (b).

SEM imaging was conducted before the tests and after a few hundred hours of operation, but did not show any clear sign of deterioration, indicating that if a shortening of the CNTs did happen it was negligible or marginal. It is known that when CNT arrays are grown, they come with some length distribution. State-of-the-art growing methods ([20, 23]) permit this distribution to be at a really low level, usually in the order of less than 5% of the CNT average length. However, the longest nanotubes will clearly emit the most and will burn-out quickly. If this process is controlled via a conditioning process the major effect will be a shortening which will translate in an improved length homogeneity and therefore more stable emission. Of course, the shortening can often translate in appreciable vacuum changes that in turn can alter the emission properties for a time. Therefore, major changes to the emission performances can then be attributed to burnout/shortening of protruding CNTs, which is not trivial to detect via SEM imaging, out-gassing and desorption from the nanotubes' tips.

The next step was to test the sample ramping the voltage and therefore the electric field. The emission properties as a function of the applied electric field have thus been studied and are shown in figure 4.7. The threshold field, defined here as the electric field necessary to reach a current density of 1 mA/cm^2, is $E_{tr} = 1.67$ V/μm for the two cases studied. The two cases mentioned correspond to two different voltage ramps performed on a CNT1 sample: the first one was made after about 380 hours of operation, and the second one after an additional 300 hours. However, the behaviour of the two curves, both fitted with the classic FN equation [29] for simplicity 2.8, show a slight shift when the electric field increases, indicating that the conditioning process has indeed changed the emission properties (figure 4.7). Despite the FN formula being theoretically incorrect when it comes to describing the field emission properties of CNTs [37, 41, 42], it is still correct in the regime of interest. This means that for comparing between two similar samples it is still useful due to its simplicity. These preliminary tests give a clear understanding of how the emission properties can change from operation-to-operation if the samples have not been pre-conditioned properly. A further source of instabilities and possible cause of sample damage is also represented by the anode itself. As mentioned in the previous chapter the anode material was changed from copper to molybdenum. On the copper surface, after use, clear sign of burnt material could be seen, most likely due to the oxygen content or gas absorption on the metal surface due to air exposure. The electron beam hitting the surface causes a temperature increase which in turn can cause gas atoms release from the metal's surface. Meaning that the anode needs conditioning prior to operation. Bake-out can mitigate this effect, but cannot fully eliminate it. This is in fact a normal behaviour that has also been experienced in other experimental apparatus for gun testing and in the ELENA electron cooler as well during the first stages of electron emission.

All these phenomena drastically affect the current emission during the first stages. As discussed above, vacuum spikes often lead to current peaks and vice-versa. However, when this is performed with the due time and step-by-step, it was observed that after a time of re-adjustment the sample keep emitting and ultimately the current emission stabilise, indicating that no permanent damage was inflicted. Further tests have in fact shown that the CNT1 samples can still emit for hundreds of hours without showing signs of burnout.

Concerning the test with CNT2-type arrays, most chips did not show acceptable performances. Among the properties shown by the CNT2s, a higher threshold field was measured, $E_{tr} = 2.71$ V/μm, with respect to the CNT1s. On the other hand, although CNT2s showed a good initial stability, their lifetime was significantly lower than that for CNT1s, as shown in figure 4.8. In their best performance the CNT2s reached total burnout after approximately 500 operation hours, a value much smaller than for the CNT1s, for which an operational time of more than 1,500 hours was demonstrated without clear signs of burnout.

Ultimately, none of the correctly used CNT1s reached burnout after hundreds of hours of use. The 1,500 hours value concerning the CNT1-type samples' operation time arises from a cumulative analysis of all the measurements performed on a CNT1 sample. Such tests include trial voltage ramps and several conditioning tests made at fixed fields and performed at different base pressures. Such additional tests are similar to the tests presented so far and are not directly reported since they do not bring any additional value nor further depth to the discussion.

In the CNT2-type arrays, the number of CNTs is significantly smaller than it would be in a CNT1-type array of equal size. For equal chip size a CNT2-type array would have a number of CNTs of around 25 % compared to a CNT1-type array. This explains why the field necessary to extract a comparable amount of current is higher. As a consequence, this causes two operational problems: a bigger current per tip must be emitted, which increases the stress on the nanotubes, thus negatively affecting stability and

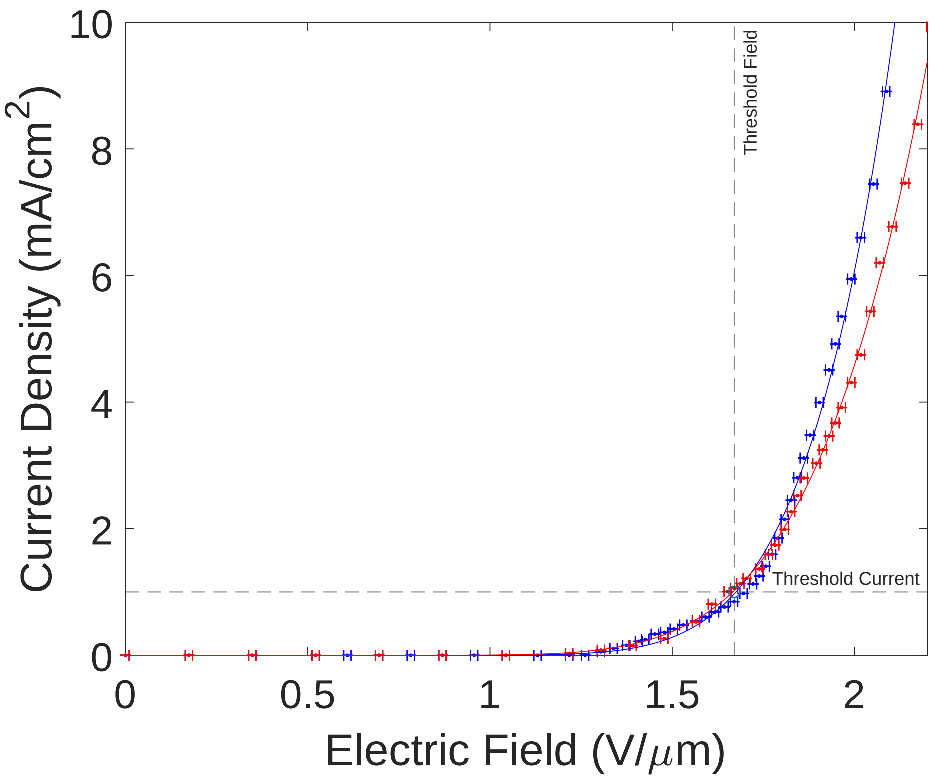

Figure 4.7: Plot of experimental points and fit with Fowler-Nordheim equation of an electric field ramping test for CNT1-type array. On the axis: applied electric field vs current density at $t_1 = 380$ h (blue) and $t_2 = t_1 + 300$ h (red). The threshold field relative to the threshold current of 1 mA is represented with the dotted lines and centered at the value $E_{tr} = 1.67$ V/μm. The error bars for Plot 1 and Plot 2 are derived from the instruments' precision, e.g. the multimeter sensitivity for the current density and the voltage power supply sensitivity for the electric field.

lifetime, as indicated by the experiments conducted so far; a larger applied electric field is required, which translates into more energetic electrons, while for the purpose of this work it is important to keep the electron beam energy as low as possible.

All the above conceptual and experimental evidences led to discarding the CNT2-type arrays and focus the investigation on the CNT1-type arrays to be applied in the electron cooler gun.

The effect of the environment conditions on the current emission is also shown in figure 4.8. At the time of CNT2 burnout a large vacuum spike can be noted as shown in figure 4.8(b). This is the same effect seen in the lifetime measurement of CNT1, figure 4.8(a). The two chips were being tested simultaneously and after the vacuum spike the emitted current for the first array undergoes a steep peak and then drops significantly. This is an interesting event, in fact it supports the assumption that the environment significantly alter the emission process without however necessarily leading to permanent damage.

Further studies at different vacuum levels on other samples showed how the difference in emission stability can be striking. For optimal performance, a pressure in the order of 10^{-8} mbar or lower is necessary to avoid significant contributions from ionization processes. Further proof of this behaviour is given by the increased performance of CNT1s when the pressure was decreased below 1×10^{-8} mbar. It is possible to infer from figures 4.9 and figure 4.10 how the emission stability was improved without clear signs of deterioration. As an additional improvement, a bake-out process was also added to clean the vacuum chamber and the emission region. The bake-out permits to reach a lower base pressure and at the same time cleans the cathode, emission region and anode from part of the adsorbants present due to air exposure.

Figure 4.9 shows results from stability tests conducted on the same CNT1 sample on which the lifetime and stability studies were previously reported. In this case, the test is performed in switching mode to test the feasibility of current switching as required for ELENA. In this mode, the cathode emits for about 15 seconds, which is approximately the cooling time for the first cooling plateau in ELENA, followed by 15 seconds of pause, which is approximately the time required for injection, deceleration steps and ejection in the ELENA cycle. The emission switching was initiated via a LABVIEW routine, which controls the power supply providing the negative voltage to the cathode. The power supply was switched on and off every 15 seconds. In figure 4.9(a)

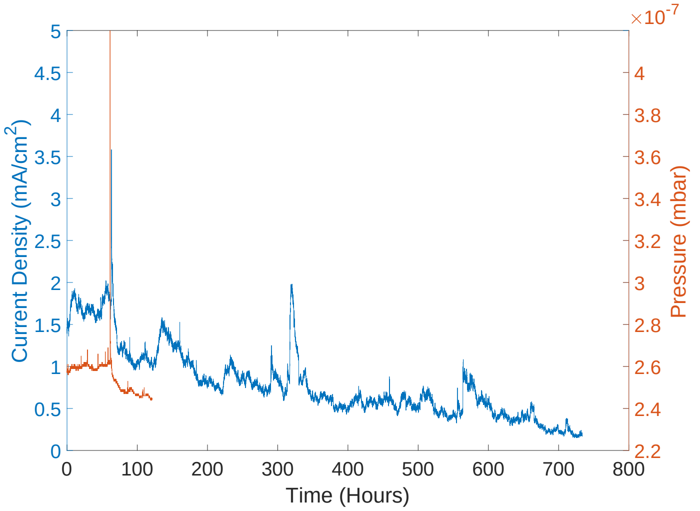

(a)

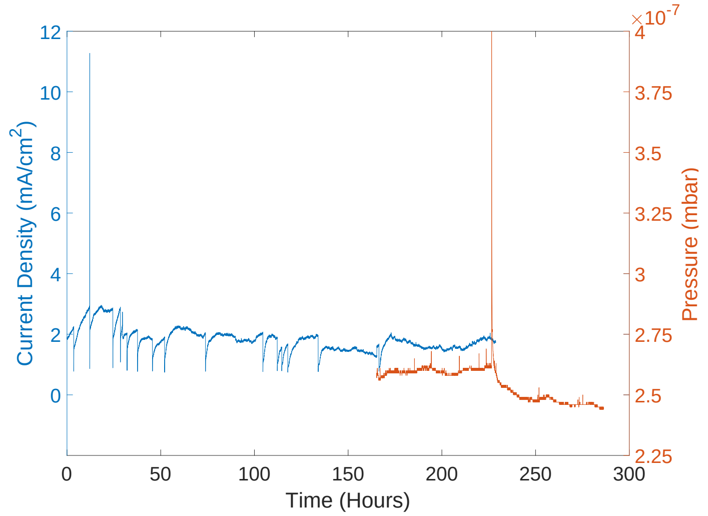

(b)

Figure 4.8: Lifetime test for CNT1 with a fixed field $E = 3$ V/μm (a) and for CNT2 with fixed field $E = 3.9$ V/μm (b).

it is possible to see how the switching does not cause significant variations despite the presence of local low current peaks. These are due to two possible causes, the imperfect switching system which is based on turning on and off the power supply via software, and a possible overshooting, meaning that the voltage reaches a localised peak before stabilising to the set value. After around 14 hours the switching was stopped to evaluate the stability in DC. The stability was still optimal. In figure 4.9(b) the switching is restarted and continued for 25 additional hours without clear signs of degradation. This initial studies using a current switching mode are not conclusive but served as a first test to assess its feasibility. More accurate results relative to the current switching mode and achieved using an appropriate and ad-hoc hardware will be presented in the next sections.

The samples used so far have all been exposed to harsh conditions, such as relatively high pressure (above 10^{-7} mbar), joint operation with other cathodes, absence of bake-out etc. At the same time all these tests permitted to find the best conditions for ensuring stable and reliable emission. Additionally, they show how CNT cathode, while needing care during operation, remain quite robust.

In figure 4.10 the performance of another sample (CNT1-type) is presented. The emission is remarkably stable for more than 250 hours in total at two different applied electric fields. In this case, there was an optimal pressure of less than 1×10^{-9} mbar and a bake-out process at 220 °C was performed before the test. However, CNTs can easily be heated to much higher temperatures since they are grown at temperatures of the order of 700 °C.

Comparing now the results obtained for the CNT1-type array it is possible to extract some further evidence of the importance of the conditioning process and the need to ramp up the electric field gradually. In fact, it can be seen in figure 4.7 that the current emitted per applied electric field is extremely high compared to all other results from stability tests for the same sample. Especially considering that the results for the additional CNT1-type sample are comparable with the first sample's latest results. After efficient conditioning and with a proper base pressure of at least 10^{-8} mbar these discrepancies disappear. In fact, in figure 4.6b the extracted current density amounts to 0.7 mA/cm^2 on average for an electric field of 2.4 V/μm, and in figure 4.10 a similar current density of 0.9 mA/cm^2 at an electric field of 2.5 V/μm was measured. This shows that samples of the same type roughly exhibit the same performance, proving a good reliability for the emission from

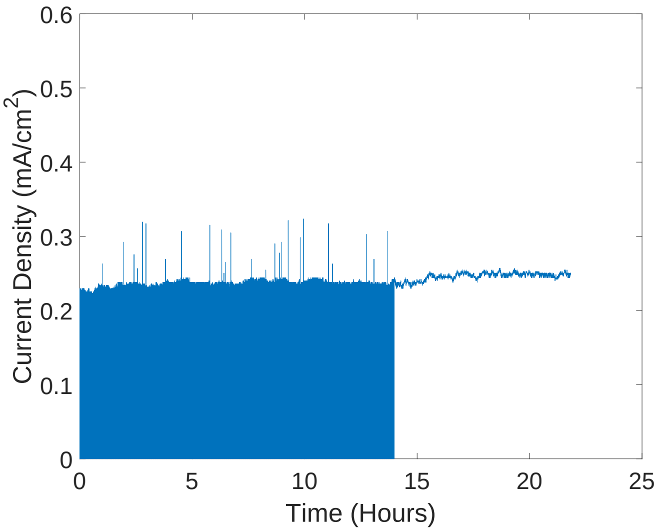

(a)

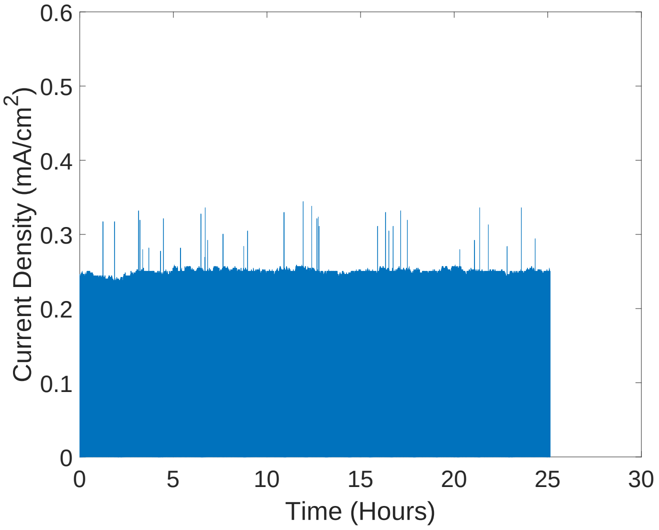

(b)

Figure 4.9: Emission stability test in current switching mode for a CNT1-type array ($E = 2$ V/μm). In (a) the switching mode is operated for around 14 hours, then the emitter is subsequently operated in DC mode to compare stability. In (b) the switching mode is continued for an additional 25 hours.

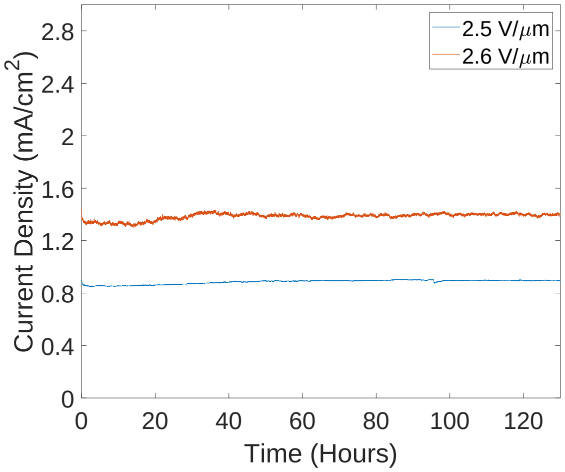

Figure 4.10: Emission stability test for CNT1-type array at two different applied electric fields: $E = 2.5$ V/μm and $E = 2.6$ V/μm.

CNT arrays, which could not be taken for granted based on the literature. These comparisons show that without a proper and efficient conditioning process it is hard to separate the real performance of the sample from spurious effects caused by ionization processes, adsorbates temporarily changing the work function value and presence of protruding CNTs.

The measurement of the current density as a function of the applied electric field was then conducted on this last CNT1-type sample. In this case, the conditions were optimal for both pressure and bake-out. It is possible to see from figure 4.11 how, despite some small variations, the results tend to converge to similar values and also agree more with the results achieved via stability measurements. In this particular case the electric field was ramped up and down six times from 0 to 2.6 V/μm. This electric field range permitted to reach current densities up to 2 mA/cm^2. Since the emission target is in the order of 1–2 mA/cm^2, the study was limited to this current density range. This is also motivated by the same behaviour shown in every ramp despite some little adjustment, which suggests that the conditioning process was efficient and that the current values which were set as requirements are easily reachable at relatively low fields and in a reproducible way. In figure 4.11 it is also possible to notice a kink in the emitted current when the applied electric field exceeds 2.4 V/μm. This behaviour holds for all six ramps, both

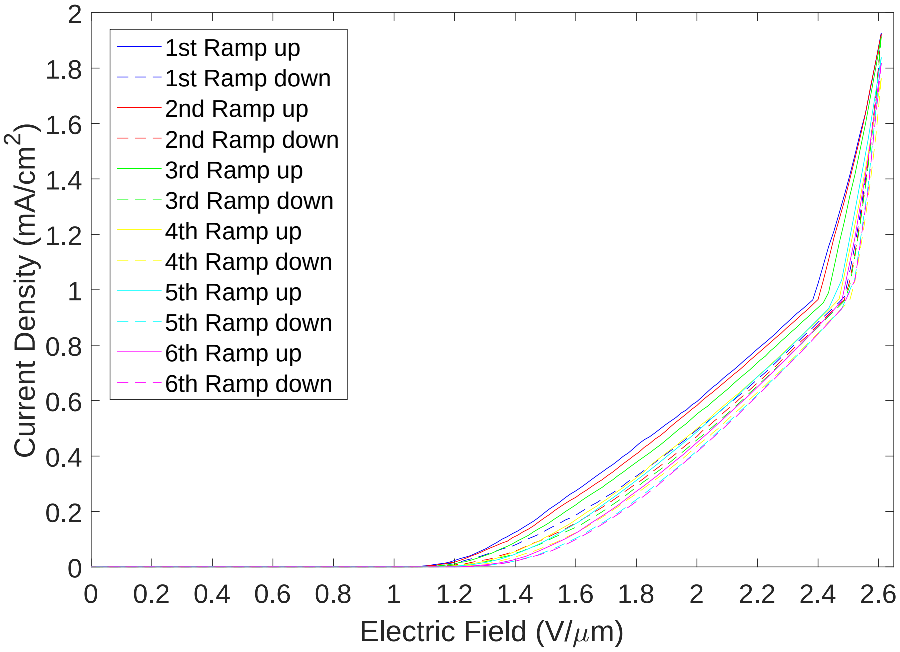

Figure 4.11: Current density vs applied electric field for CNT1-type array. The test include six voltage ramps with data acquisition on both the way up and down. The electric field was ramped from 0 to 2.6 V/μm.

on the way up and on the way down, indicating the possible presence of a change in the emission behaviour. This change seems to suggest the presence of two different emission regions, one below approximately 2.4 V/μm where the current emission seems to be inhibited and one at higher fields where the exponential behaviour of the current rise is enhanced. This is a behaviour that it has not been found anywhere in literature. The most probable reason for this is that when going to higher electric fields and also if the data are fitted, this change of region is suppressed by the fitting. However, it is visible in this particular case, as extremely high current are not needed and electric field is limited to a narrow low value region. The reason proposed to explain this phenomena is connected to extraction efficiency. In other words, at a certain field the emission is enhanced because of more efficient extraction.

Another factor to take into account was the current stability for different values of emitted current. For this reason a further experiment on this last CNT1 sample was performed. A study of the emission stability at five different applied electric fields for about 20 hours was performed, figure 4.12(a), and then the standard deviation σ for the emitted current density for each case was calculated. The standard deviation reflects the intensity of the current density fluctuations over the period of study. The results show an increase in the overall standard deviation when the current density increases. However, the calculation of the coefficient of variation percent shows instead an inverted trend. The coefficient of variation c_V, or relative standard deviation, is defined as the ratio between the standard deviation σ and the mean value of the data set (i.e. the average current density $\langle J \rangle$) and it is usually represented as a percentage [100],

$$c_V[\%] = \frac{\sigma}{\langle J \rangle} \times 100\,. \tag{4.1}$$

In this case, it represents the variation percentage of the emitted current density and provides a description of the emission stability over time. The analysis of the coefficient of variation shows how the current density variation percentage decreases at higher emitted current densities, indicating optimal stability when the emitted current density is increased, figure 4.12(b).

The experimental data is represented with circles, while the full line represents a fit of the experimental data in order to make the trend clearer. The fit was made with MATLAB and with a power equation of the type: $y = ax^b + c$.

This study suggests that CNTs can also stably emit at high applied elec-

Table 4.1: Measurement of standard deviation σ and coefficient of variation c_V of the emitted current density of a CNT1 sample at five different applied electric fields E and current densities $\langle J \rangle$.

E (V/μm)	$\langle J \rangle$ (mA/cm^2)	σ (mA/cm^2)	c_V (%)
2	0.337	0.006	1.85
2.1	0.611	0.005	0.85
2.25	0.762	0.006	0.76
2.43	0.953	0.006	0.58
2.6	1.385	0.01	0.73

tric fields with coefficient of variation of even less than 1 %. These results are summarized in Table 4.1.

Therefore, the choice of having large or small area cathodes would solely depend on the operational requirements regarding the total nominal current variations and most importantly the beam energy. For the emitted current and its variations, at equal nominal emitted current, a large area cathode permits lower current densities, therefore having slightly smaller nominal fluctuations; a behaviour that does not extend to the current density variations percentage. For the beam energy, large area samples permit the application of a lower electric field at equal nominal emitted current, therefore having electrons with lower longitudinal kinetic energy. This could be beneficial for operations requiring low energy electrons such as the ELENA experiment.

4.2.2 Surface analysis and work function measurements

The current output in field emission strongly depends on the work function, it is therefore important to accurately determine its value. It is possible to see the dependence of the emitted current density on it from the FN equation (equation 2.8). In fact, the work function of a material is one of the main parameters for determining how strongly the electrons are bonded to the material and how much energy is required to extract them. In field emission, electrons do not need to be excited above the potential barrier between the material's surface and the vacuum. In fact, during field emission, such potential barrier is lowered by the external field and this increases the probability of electron tunnelling. For this reason, even localized changes in the work function due to the presence of adsorbates on the CNT tips can lead

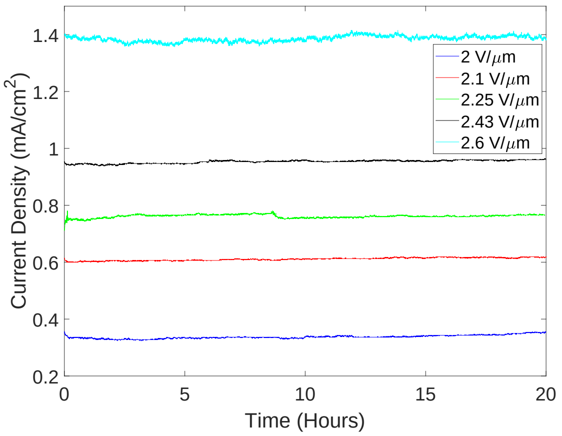

(a) Current density (mA/cm^2) as a function of time (hours) for CNT1 sample. Measurement conducted at five different applied electric fields for 20 hours of emission each.

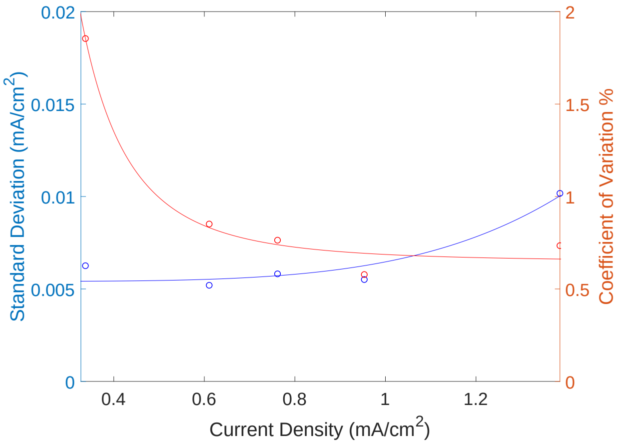

(b) Standard deviation (mA/cm^2) and coefficient of variation (%) as a function of the current density (mA/cm^2) for CNT1 sample.

Figure 4.12: Emission stability measurements at five different applied electric fields.

to drastic changes in the emitted current. Such changes will of course depend on the adsorbed elements since this can cause a change in the work function. This translates into a reduction of the emitted current, or alternatively, an increase in the emitted current due to a drop in the work function [72, 101].

Therefore, a characterization of the material's surface was performed in order to investigate these aspects. The surface properties of CNT samples were characterized under UHV conditions to determine the surface composition by XPS and to characterize the global work function of the CNTs by SEY measurements and UPS. Structured samples with either the honeycomb-like array or the square-island array were characterized after loading in the analysis system. As the lateral resolution of the implemented experimental techniques is limited to a spot diameter of 1–2 mm, leading to a superposition of signals from the CNT regions and the surrounding silicon wafer, a further characterization study was performed on two additional CNT samples ("Full Coverage 1" and "Full Coverage 2"), which consisted of a silicon substrate fully covered with CNTs on an area of 10×10 mm^2 that were grown using comparable processing parameters, except for slight adjustments in the gas ratio during growth. Additionally, on these two samples annealing cycles under UHV were performed to investigate whether air exposure affects the work function and surface composition and whether a thermal treatment in vacuum could improve the surface quality. All measurements were performed at room temperature, i.e. after each annealing step, the sample was left to cool down. Four annealing steps were performed:

- 180° for 30 mins,
- 180° for 120 mins,
- 250° for 240 mins,
- 300° for 180 mins.

Several groups have reported results on the work function of CNTs, with values spanning from 4 to even 5.6 eV, depending on the technique used and possible alterations due to adsorbates [102–104]. The performed measurements aim to quantify the work function value of MWNTs before and after annealing, which is linked to their practical utilization in a baked UHV chamber for field-emission applications in ELENA.

RGA was performed during each annealing cycle by means of a continuous recording of spectra to monitor the out-gassing and desorption. This allows the simulation of a bake-out of the vacuum chamber to improve the base pressure, while simultaneously also heating the CNT emitter region. The RGA measurements inevitably include signals from species desorbing from the CNT area as well as the pre-degassed sample holder. Therefore, their results allow only a partial identification of bake-out induced benefits for the CNT surface. As expected, mainly H, H_2, O, OH, H_2O, CO, various hydrocarbons, and CO_2 are desorbed. During the first cycle at 180 °C, the main contribution is water desorption and emission of volatile species. At higher annealing temperatures the relative content of CO and CO_2 increases, which is consistent with desorption and conversion of species at these temperatures. As anticipated such thermal treatment allows successful cleaning of the sample and especially of the CNTs for electron emission. As a result, it also prevents pressure bursts during emission ramp-up as confirmed by the stability measurements. The RGA experimental results hereby presented cannot provide for a quantitative analysis relative to the thermal treatment benefits, although they do provide for a qualitative endorsement of its beneficial effect to the emission region and sample cleaning. These results have been summarised in figure 4.13. The spectra reported are relative to the sample “Full coverage 2” and to the time when the out-gassing was the most significant. In fact, the out-gassing process during the annealing cycle would reach a peak after a certain time and then the out-gassing would decrease. The spectra are relative to the out-gassing peaks of each annealing step.

XPS measurements of the sample “Full coverage 2” before and after the annealing process are shown in figure 4.14. Most important to note is the low impurity level of oxygen (1.1 at.%) even without annealing, for which the weak signal of the 1s state is at 532.5 eV binding energy (i.e. the binding energy of the electrons in the first orbital, the orbital “1s”, of the oxygen atom). This oxygen content dropped further to below the detection limit of the O1s state (0.1 at.%) after annealing. In addition, iron (Fe) is detected (0.05 at.%) which is due to the iron catalyst layer that is deposited onto the silicon wafer prior CNT growth. The fluorine impurity signal (0.4 at.% before heating) disappeared as well as the oxygen contribution after the thermal processing. Figure 4.14b includes the spectra of the C1s state (i.e. the binding energy of the electrons in the first orbital, the orbital “1s”, of the carbon atom) for the sample prior to and after the annealing steps. Overall, only slight changes in the XPS spectra occurred. While the peak maximum at 284.5 eV is unchanged, the thermal processing in UHV induced a slight signal increase of the electronic excitations (around 290.5 eV) of the CNT sample. This as-

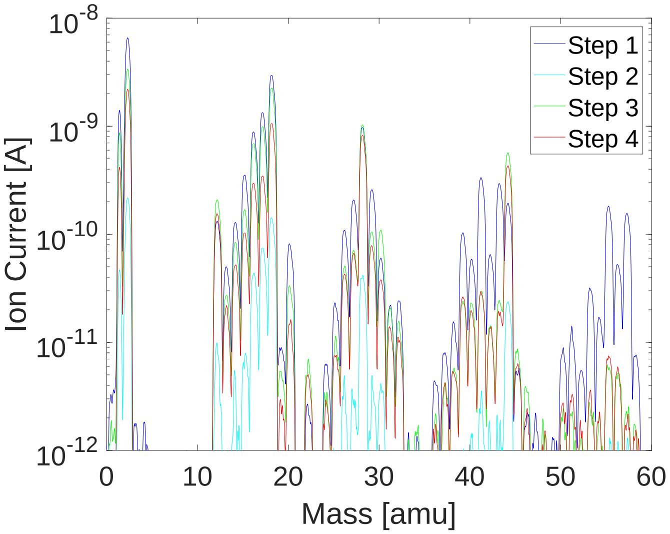

Figure 4.13: RGA spectra of a full coverage CNT sample. The spectra are relative to the four annealing cycles and are reported in logarithmic scale.

pect is to be attributed to the thermally induced desorption of adsorbates from the nanotube surfaces that partially saturated π electrons before the heating process. It is anticipated that the increase of delocalised electrons at the CNT surface is advantageous for its electron emission performance and stability.

The work function was extracted from the low primary energy part of the SEY curve. The method used, called beam-stop method, was already applied in earlier studies [94, 105, 106] and is correct when the beam is impinging normally to the surface. As this method requires a reference material for determining the work function, a sputter-cleaned polycrystalline gold sample with a work function Φ of 5.3 eV was measured in parallel [107]. Work function differences can be determined with high precision (0.01 eV) using this approach. Figure 4.15(a) shows as an example the energy dependence of the SEY at low energy for a CNT sample and the Au reference, while the derivatives of these curves are shown in figure 4.15(b). As the derivative represents symmetrical peaks, their minimum was used to determine the work function difference. The measured Φ values are summarized in table 4.2. After insertion in the analysis system Φ is around 4.4 – 4.5 eV. Figure 4.15(c) indicates that the UHV annealing up to 300 °C has only a minor influence on

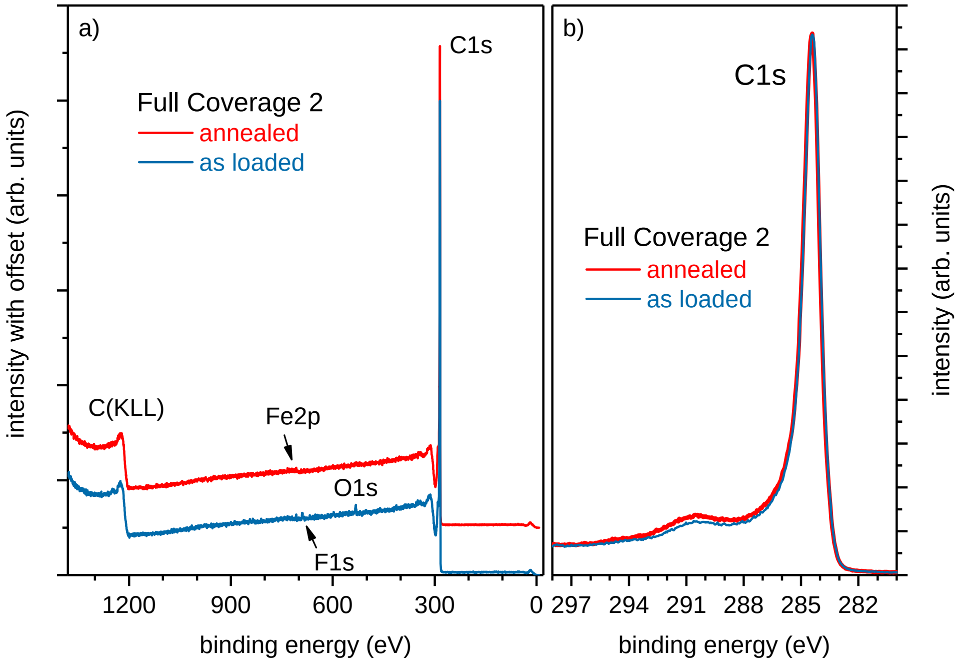

Figure 4.14: (a) XPS survey spectra of CNT sample “Full Coverage 2” as loaded and after the complete UHV annealing process. (b) Corresponding C1s spectra.

Table 4.2: Determined work function Φ in eV for the four different samples: honeycomb-like array (“Honeycomb”), squared-islands array (“Squared”), Full Coverage 1 (“FC 1”) and Full Coverage 2 (“FC 2”). Analysis based on SEY (used for “*as loaded*” and the first line of “*after annealing*”) and UPS (used for the last “*after annealing*”) analysis.

Sample condition	Honeycomb	Squared	FC 1	FC 2
as loaded (SEY)	4.38 ± 0.01	4.40 ± 0.01	4.47 ± 0.01	4.45 ± 0.01
after annealing (SEY)	-	-	4.45 ± 0.01	4.42 ± 0.01
after annealing (UPS)	-	-	4.54 ± 0.1	4.57 ± 0.1

the surface work function of the CNTs. As determining absolute work function values is always linked to experimental uncertainties (typically 0.1 eV), after annealing of the fully covered samples, Φ was additionally measured by linear extrapolation of the leading edge of secondary electron emission. The resulting values of (4.54 ± 0.1) eV and (4.57 ± 0.1) eV for sample “Full Coverage 1” and “Full Coverage 2”, respectively, match very well with the numbers obtained by the SEY analysis.

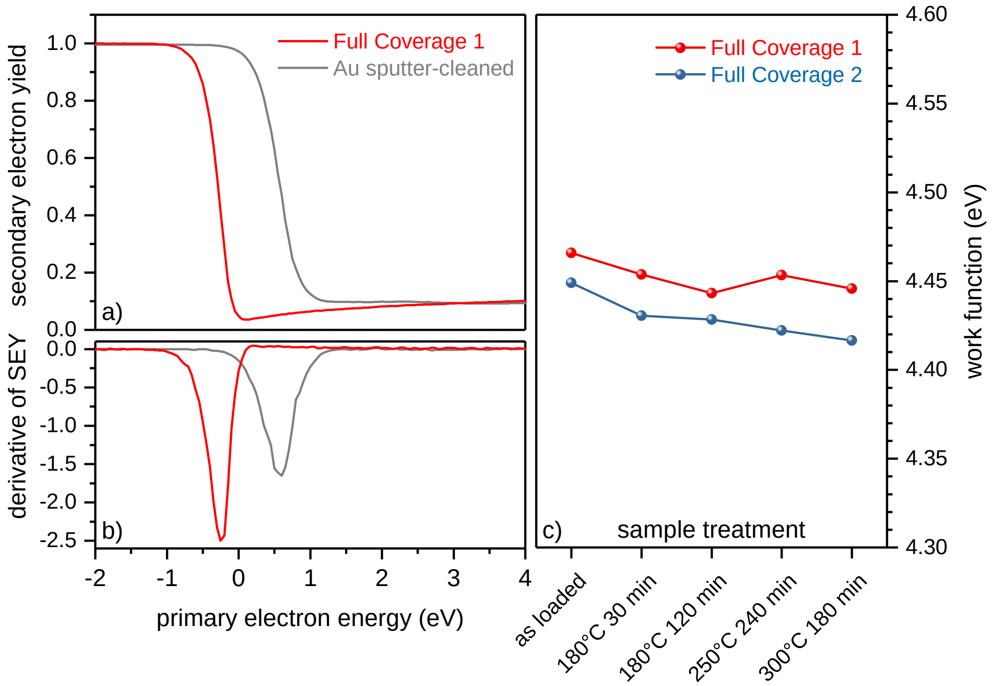

Figure 4.15: Work function analysis based on SEY measurements. Example LE-SEY data of the homogeneous CNT sample “Full Coverage 1” and a sputter-cleaned Au reference sample in (a) and the curves derivatives in (b). The variation of the work function during the performed heating cycle of samples “Full Coverage 1” and “Full Coverage 2” under UHV based on SEY measurements is shown in (c). The errors on the work function measurements performed through SEY are of approximately 0.01 eV.

4.3 Current switching system

The tests on the current switching mode have allowed calculation of the rise and fall times of the current emitted from CNTs and at the same time provided proof of the cathode's unmodified emission stability when used in current switching mode.

As first thing the difference between the signal coming from the signal generator and the signal measured after the push-pull are compared. The measurement after the push-pull is performed with a common oscilloscope probe and therefore it was necessary to use a low voltage; in this case, 20 V. The results relative to rise and fall are reported in figures 4.16 and 4.17. From the signal generator output it is possible to infer how the time necessary for the the signal to go from 5 V to 0 V and vice-versa is of about 40–50 ns. It then takes about 300–350 ns for the signal to fully stabilize. In that range some signal oscillations in the order of 0.1 V are observed, which are due to noise, most likely arising because of the cabling. The start of the signal inversion for the switch takes place about 100 ns later, this is motivated by the delay due to the cabling. To fully invert the signal the push-pull system additionally requires about 250 ns, and additional 100 ns to reach perfect stability. This makes for a total of about 300–400 ns. The scenario is perfectly symmetrical for the rise and fall of the signal, which also provides good proof that the reason behind the delays must be connected to cable-induced delays. The oscillations are instead due to possible residual impedance mismatch in the circuit, signal reflections, and field perturbations. However, the rise and fall times are well below 1 μs, which is an optimal result.

The main problem that was encountered during these measurements was due to a capacitance effect which was noticed in the shunt measurements. This is presented in figure 4.18. What is noticeable from figure 4.18 is a voltage rise when any voltage is applied. This effect happens symmetrically on the other side of the square wave with inversed polarity. The decay time of the voltage drop is of about 500–600 ns. An increase of the voltage doesn't provoke an increase of the decay time, while however inducing a higher voltage drop. This effect caused a few issues such as reaching the oscilloscope limitations at high voltages and masking the first 500–600 ns of the measurement. Nevertheless, this are all effects taking place in under 1 μs and do not represent a problem considering ELENA's specific requirements. Currently in ELENA, the electron gun's switch has rise and fall times in the order of 1 ms, which translates in an improvement of about three orders of

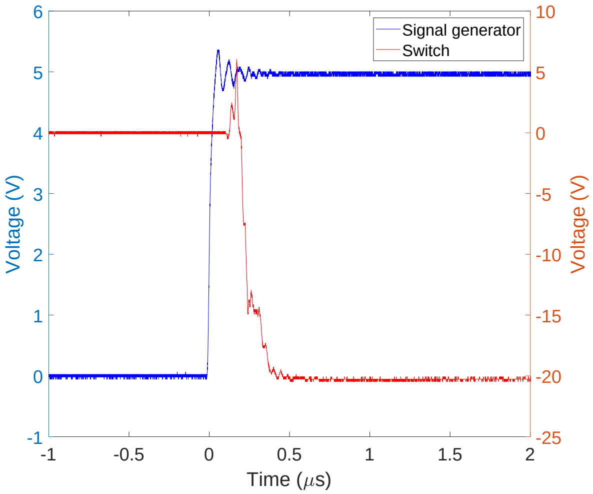

Figure 4.16: Comparison between the rise of the square wave coming from the signal generator and the square ware measured after the push-pull when a voltage of 20 V is applied.

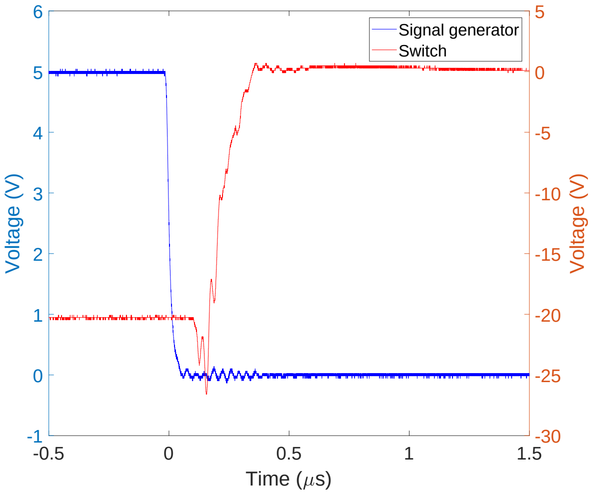

Figure 4.17: Comparison between the fall of the square wave coming from the signal generator and the square ware measured after the push-pull when a voltage of 20 V is applied.

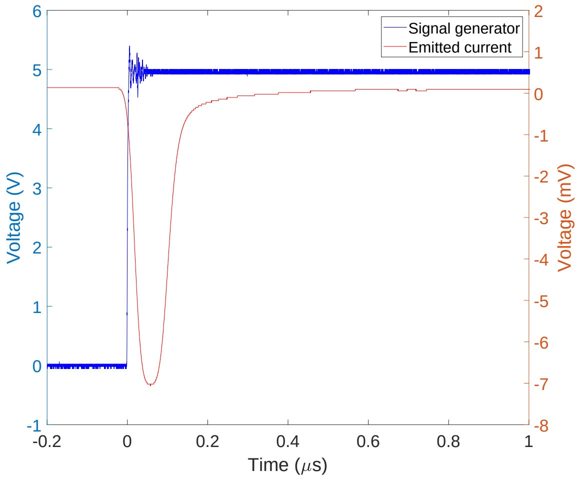

Figure 4.18: Shunt measurement when a voltage of 20 V is applied.

magnitude.

In order to fully establish the nature of the capacitance effect, a measurement of the capacitance of the cathode-anode system was performed; including the cables and up to the shunt where the current measurement takes place. The value of the capacitance that was found is 420 ± 10 pF. Considering the low-voltage side of the circuit as an RC circuit, including the CNT cathode and cathode-anode structure whole, the capacitance of the system can be analytically derived from the time constant t of the RC circuit, $t = RC$. $R = 1$ kΩ and $t = 500$ ns, therefore it can be obtained $C = 500$ pF, which is consistent with the value found empirically.

The final measurements on the current switching mode were performed using an applied voltage of up to 900 V. Which, considering an inter-electrode distance of about 800 μm, corresponds to an applied electric field of about 1.12 V/μm. With this applied electric field it was possible to extract a current of up to 30 μA. In figures 4.19 and 4.20 the rise and shutdown times relative to the emitted current can be observed.

As it is possible to notice from figures 4.19 and 4.20, the voltage drops relative to the aforementioned capacitance effect are still present and are perfectly symmetrical. The rise and shutdown times are of about 600 ns, which is due to the capacitance effect. However, this also proves that the emission from the CNT cathode can be switched on and off in a time that is

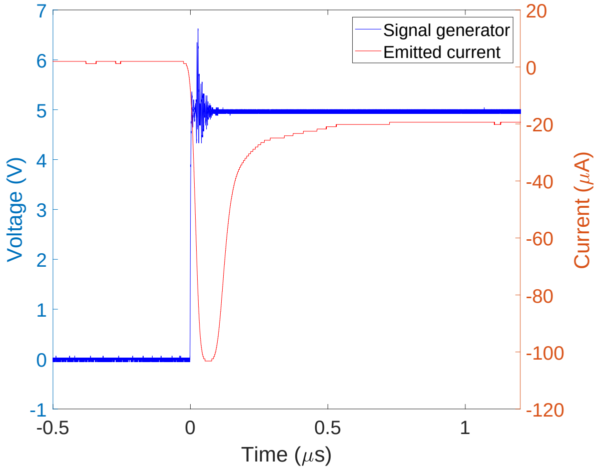

Figure 4.19: Shunt measurement of the emitted current rise at an applied voltage of about 900 V.

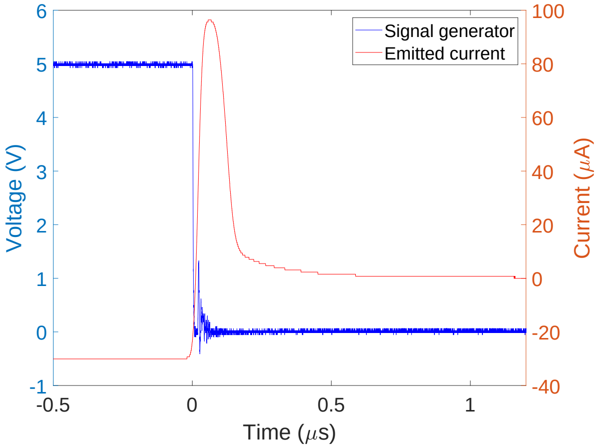

Figure 4.20: Shunt measurement of the emitted current shutdown at an applied voltage of about 900 V.

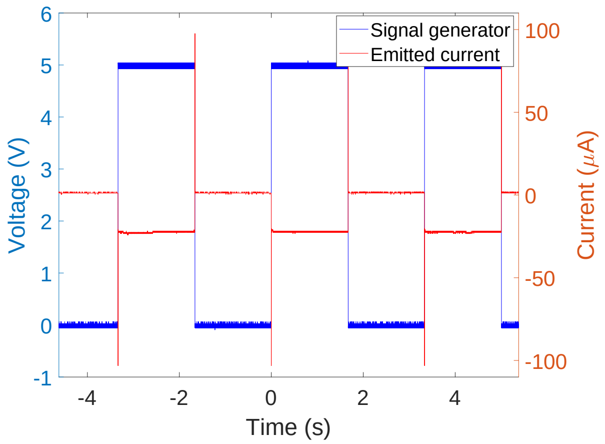

Figure 4.21: Current switching test at 0.3 Hz.

no longer than 600 ns. Effectively making the switching system more than three orders of magnitudes faster than the one currently used operationally in the ELENA elector cooler.

Finally, the current switching system was tested at different frequencies: 0.3 Hz, 1 Hz, and 10 Hz. No different behavior was observed during these tests, proving that the current switching is not affecting the current emission from CNTs. Examples of these tests are shown in figures 4.21, 4.22, and 4.23. As a reminder, in ELENA the cooling time is of about 3 seconds.

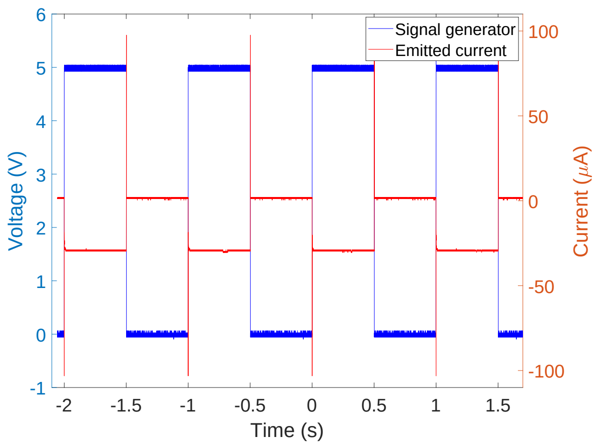

Figure 4.22: Current switching test at 1 Hz.

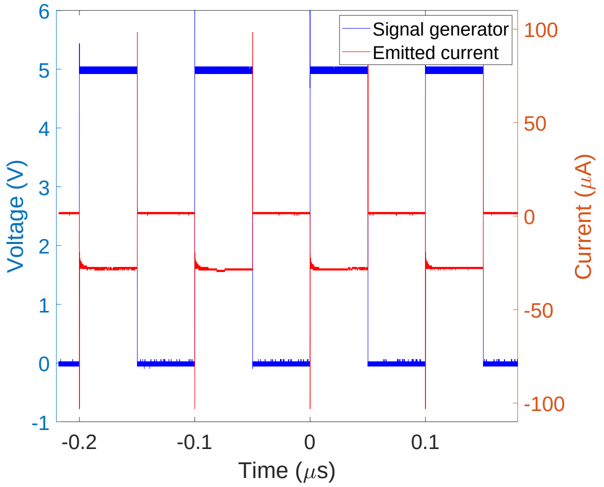

Figure 4.23: Current switching test at 10 Hz.

Chapter 5

Simulation study of the effect of extracting grids on the electron beam properties

Electron guns are used in many fields. They are used in medical applications for the production of X-rays and for radiotherapy within linear accelerators and X-ray tubes. They can be used for cathode ray tubes for the production of televisions and monitors, and they are widely used in accelerator science for linear accelerators, circular accelerators, electron cooling, free-electron lasers, travelling wave tubes, etc [59, 60, 108–112]. For electron guns, the use of grids is deemed essential for many purposes. In field emission cathodes a grid is necessary in order to extract a homogeneous beam concerning both beam current and beam energy. Grids can also be used when operating thermionic and photo-emission guns to have better control of the beam properties and to allow for efficient current switching. In most cases, the grid is placed directly after the cathode as a means to achieve the best control of the emission, beam trajectory and/or switching [59, 60, 108–119].

In all cases, the impact of the passage through the grid on the beam properties should be evaluated as it may lead to drastic variations of beam trajectory and beam energy.

In many cases of electron gun usage, the beam is extracted with a hollow anode. In a field emission gun such an anode is inappropriate, as the electric field is what drives the emission. This means that field distortions at the cathode surface translate into large emission variations for both beam current and beam energy. Therefore, a thorough study of the grid effect on the

Table 5.1: Grid types and their features.

Grid type	Hole size	Bar width
$250-50$	250	50
$200-40$	200	40
$150-30$	150	30
$100-20$	100	20
$50-10$	50	10
$25-5$	25	5

emission is essential for tuning the electron beam properties according to the requirements.

Although in this work the aim is to use CNTs, this study is relevant in the case of any field emitting cathode and in general to any case where a grid is deemed necessary. This study is considered valid for any source since the grid effect is determined in the case of different beam initial properties that can easily be re-conducted to all field emission, photo-emission, and thermionic emission.

The simulations were addressed considering the main grid parameters that can affect the beam properties, e.g. beam current due to losses in the grid, beam transverse energy due to transverse kicks within the grid holes, and beam displacement in the transverse plane. The grid distance from the cathode defines the voltage applied to the grid in order to get the desired electric field. The hole size severely affects the beam properties because of the distortion of the field lines within the hole. The relation between hole size and the bar width determines the transparency of the grid. Additionally, the hole shape and hole arrangement must be devised in order to maximize the grid transparency. Finally, the feasibility of physically manufacturing the desired grid according to the current technology must be taken into account. Six different grid types were analyzed and are listed in table 5.1. All grids are designed to have squared holes in order to maximize the holes packing and consequently the transparency. The bar width is defined as the solid spacing between each hole.

5.1 Description of the simulation layouts

All simulations are three-dimensional and conducted with the software CST Particle Studio [120], using the tracking solver. The simulation design allows for straight field lines in the whole emission region. In this way the grid represents the only source of distortion of the field lines and its effect on the beam can be isolated.

The emission is "Field Induced", with the parameters "A" and "B" of the FN equation, equation 2.8, derived from experimental results [21]. The kinetic settings of the particle emission model are set to have a uniform particle distribution with parametric energy value. The angle is set to the maximum, e.g. 89°. This gives an initial energy to all particles in all planes, e.g. x, y, and z. The number of emission points is set to adapt to the mesh size. In practice, it is over 100,000 for every simulation performed and can reach up to 400,000 for the finer meshed simulations.

There are four main simulation types and all have the layout illustrated in figure 5.1. The original CST 3D model is shown in figure 5.2. The configuration is of the triode type, meaning that there is a cathode, e.g. the field emitting material, an extracting grid, and an anode where the beam is dumped. Between the cathode and the grid is an insulating spacer. This also serves to delimit the emitting surface and at the same time limit the beam radius until reaching the grid. The voltage on the cathode and the voltage on the anode are kept constant in every case in order to set the final beam energy to the desired value. In this case such value is 355 eV, which is the longitudinal energy of the electron beam required in ELENA for the first cooling plateau. Therefore, the cathode voltage is always set to -355 eV and the anode voltage is always set to 0 V. The voltage on the grid depends on the desired electric field and consequently on the distance between cathode and grid. The meshing is hexahedral in all simulations.

Simulation 1 type was the start of the whole simulation work included in this chapter and for this reason it was the simulation which took the longest to design and test. The simulation layout is quite simple as the only requirements are to have perfectly straight field lines and perfect symmetry along the whole simulation layout. A few different simulation layouts have been tested before reaching the final design, changing parameters such as the diameters of the spacers, anode, and grid, as well as the size of the cathode. This type of simulation is quite peculiar since a large diameter for spacers and other components is required so that the field lines have space enough

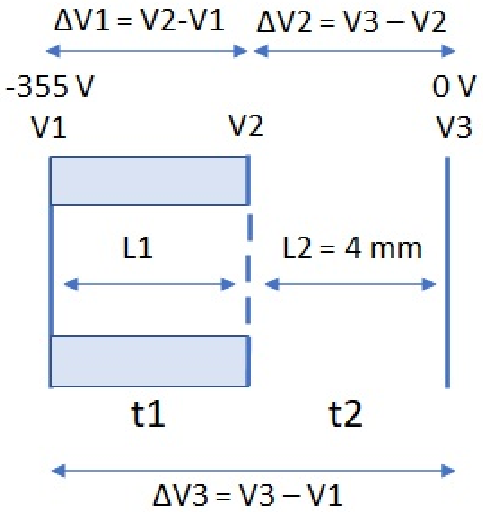

Figure 5.1: Simulation layout. Triode configuration: cathode (-355 V), grid (variable voltage depending on the cathode-grid distance), anode (0 V). Constant electric field of 2 V/μm. The emission is “Field Induced” with the parameters “A” and “B” of the FN equation (equation 2.8) derived from experimental results [21].

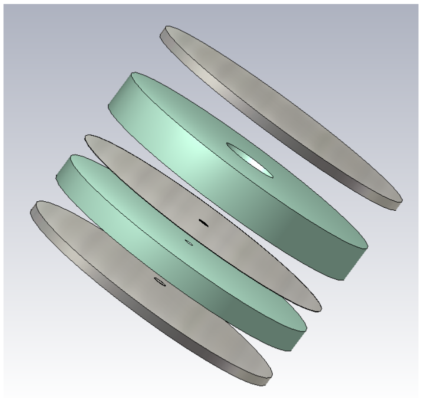

Figure 5.2: Stage view of the 3D model exported from CST. Starting from the bottom there is the cathode support with the cathode in its center, an alumina spacer, the grid, a second alumina spacer and finally the anode.

to fully straighten and thus be perfectly straight in the central region, i.e. the emission region. However, a small beam size was also required since the simulation's precision must be extremely high and this translates into very fine mesh cells, i.e. down to 2 μm, and consequently a high overall number of mesh cells, i.e. up to 200 millions. In turn, having a large number of mesh cells significantly increases the simulation time. Furthermore, it is non-trivial to model grids with extremely small holes and large overall size. The software "Autodesk Inventor" [121] was used for this purpose, which is quite powerful, but it is not able to render 25 μm holes for a space larger than a few mm. On average, with the computational power available, it was possible to render about 100×100 holes. This did not represent an issue as keeping the overall grid size as small as possible was encouraged so that the usage of very small mesh cells could be limited to a small region only.

The total number of mesh cells also needed to be carefully taken into account. The maximum number of mesh cells that it was possible to compute with the available computational power was of about 220 millions, as a maximum threshold. While it may seem that grids with small hole sizes would translate into a longer simulation time, this was actually not necessarily true. Large hole sizes requires a larger grid with larger overall size in order to have a large enough array of holes. This sets the constraint of having a larger emission region, resulting in a relatively limited precision of the simulations for grids with large holes.

All other simulation types were then simply based on the layout of the first one. The only difference was mostly represented by Simulation 2, were the thickness of the grid was parametrically changed. As previously mentioned, the grids are designed using Inventor and then imported into CST as STEP files. This means that their features cannot be changed within the CST modeler. For this reason, an alternative solution was used. A thick grid was imported into CST and it was then systematically resized by subtracting a solid, so to set the required thickness. This solution proved to work smoothly and permitted to perform a fully automatised parametric simulation.

Despite all simulations being somewhat similar for what concerns the general layout, they can be differentiated depending on the main parameter/s which were investigated and how they impact the beam properties, namely the beam current and the beam transverse energy.

5.1.1 Simulation 1: the effect of the cathode-grid distance

The grid distance is one of the first parameters to be taken into account, since this will determine the voltage applied on the grid and therefore the initial longitudinal beam energy. Furthermore, the grid distance can greatly affect the alignment of the field lines in the emission region, which is the most critical region. This region experiences the strongest electric field and it is where the beam features are mostly affected. The beam properties can be greatly affected by the field lines at the cathode's surface, where the emission takes place, and at the grid's bottom surface. The reason is that a great difference of voltage is applied between these two surfaces, resulting in drastic changes in the beam properties if the field lines are not straight.

This is a parametric simulation in which the grid distance was varied from 0.4 to 5 mm with a step width of 0.2 mm. The electric field was kept constant. The beam initial transverse energy is set to 0.1 eV in order to run a critical test for all grids. It was then possible to derive the standard deviation % of the voltage along the grid plane and the beam offset, "r", which represents the difference between the radii of the emitted beam and the beam hitting the anode. This value is calculated from the "Envelope" option in the CST post-processing tools. This option allows the calculation of the maximum absolute distance of all particles from their average position, in other words, it allows the calculation of the maximum beam radius. Furthermore, it was possible to conduct a study on the transparency of each grid.

In this simulation the precision is of about 8 μm, i.e. the mesh cell size, and the grid thickness is in all cases of 50μm.

5.1.2 Simulation 2: the effect of the grid thickness

Each of the grids have holes size in the order of several microns. However, the smaller the hole the greater is the manufacturing limitation on the grid thickness. This is connected to technical issues that pose constraints on the maximum grid thickness depending on the hole size. For instance, when considering the smallest grid, $25 - 5$, it would be challenging to manufacture it with a thickness greater than roughly 100–200 μm. However, having an extremely thin grid could also lead to higher field lines deviation/misalignment. Contrarily, greater thicknesses can result in decreasing the grid transparency. With the goal of evaluating these variables, a further parametric simulation was performed changing the grid thickness between 0.005 and 0.2 mm, while keeping the grid distance constant to 1 mm. This simulation has an improved precision of 3 μm since it is focused on the smallest hole size grids.

5.1.3 Simulation 3: the effect of the beam initial energy

The initial transverse energy of the beam is clearly a crucial parameter in order to establish the final transverse beam energy. Changes in the initial transverse beam energy may lead to different grid effects.

This is a double parametric simulation varying the grid distance from 0.6 mm to 2 mm with 0.2 mm step width and the beam initial transverse energy from 0 eV to 0.1 eV with 0.025 eV step width. It allowed analysis of the beam offset depending on the grid distance and on the beam initial transverse energy. The beam initial transverse energy is varied tuning the kinetic settings of the particle beam source in CST. This is an absolute value that has also an impact on the longitudinal energy, which however is negligible compared to the longitudinal energy acquired due to the electric field. Consequently, the beam's initial energy can be simply considered as the beam's initial transverse energy. The choice of limiting the distance to 2 mm depends on a consideration of the voltage needed on the grid to achieve the desired emitted current. Distance values much greater than 2 mm would most likely be unfeasible since it would imply the need of applying voltages higher than 10 kV.

This simulation has an precision of about 3 μm. The grid thickness is 50 μm in this case too.

5.1.4 Simulation 4: the effect of the applied electric field

In the previous simulations a fixed electric field was set to isolate the parameters of interest and only investigate the dependencies on grid distance and initial transverse energy. However, the electric field can also affect the beam properties and its impact must be evaluated.

This is a double parametric simulation in which the grid distance is varied from 0.6 mm to 2 mm with 0.2 mm step width, and the electric field is varied from 2.5 V/μm to 6 V/μm.

The grid thickness is $50\,\mu$m. The simulation precision is about $3\,\mu$m.

5.1.5 Data analysis

After the simulation the data analysis was conducted using "MATLAB" and/or "Python" after exporting the data sets from CST.

It was also possible to calculate the transverse energy of the beam using the beam envelope extracted from the simulations. Considering how the beam offset was calculated, the transverse energy derived will represent the maximum possible transverse energy of the electrons composing the beam. The formula used for the calculation is

$$E_{tr}\,[eV] = \frac{V_2^2 r^2}{32\left(\sqrt{2(V_2+355)} - 26.646\right)^2}. \tag{5.1}$$

This formula was derived considering the simulation layout and it is only valid if the field lines are perfectly straight in the whole simulation region, since in such case there are no field contributions in the transverse plane. The kinetic energy for non-relativistic particles is given by

$$K = \frac{1}{2}mv^2, \tag{5.2}$$

with m being the particle mass, in this case the mass of an electron, and v being the electron velocity.

The particles' motion in the transverse plane, considering the region between the grid and the anode, will be given by

$$r = vt_2 + \frac{1}{2}at_2^2. \tag{5.3}$$

Considering that the electric field in the transverse plane is equal to zero, then the acceleration a will also be equal to 0. Therefore, using equation 5.2 and considering $K = E_{tr}$

$$r = vt_2 = \sqrt{\frac{2E_{tr}}{m}}t_2, \tag{5.4}$$

with t_2 being the time that the electrons require to go from the grid to the anode as indicated in figure 5.1.

Let us now take into account

$$F = ma \;\Rightarrow\; a = \frac{F}{m} = \frac{eE}{m} = \frac{e\Delta V}{L\,m} \tag{5.5}$$

with E being the electric field value and e the electron charge. L_2, ΔV_1, ΔV_2 and ΔV_3 are the parameters illustrated in figure 5.1. It is now possible to determine the time t_2 considering the longitudinal motion of the electrons from the grid to the anode

$$\begin{aligned} v = v_0 + at_2 &= \sqrt{\frac{2\Delta V_1}{m}} + \frac{e\Delta V_2}{L_2 m}t_2 \\ \Rightarrow \sqrt{\frac{2\Delta V_3}{m}} &= \sqrt{\frac{2\Delta V_1}{m}} + \frac{e\Delta V_2}{L_2 m}t_2. \end{aligned} \tag{5.6}$$

In this case there were a retarding field and a grounded anode ($V_3 = 0$), therefore $\Delta V_2 = V_3 - V_2 = -V_2$. Setting $e, m = 1$, it can be shown

$$t_2 = \frac{L_2}{V_2}(\sqrt{2\Delta V_1} - \sqrt{2\Delta V_3}) \tag{5.7}$$

Combining equations 5.4 and 5.7,

$$E_{tr}\,[eV] = \frac{V_2^2 r^2}{2L_2^2\left(\sqrt{2\Delta V_1} - \sqrt{2\Delta V_3}\right)^2}. \tag{5.8}$$

Substituting all the data from the simulation layout equation 5.1 is obtained. Namely: $L_2 = 4$ mm, $\Delta V_1 = V_2 + 355$ V, $\Delta V_3 = 355$ V.

Finally, the calculation precision, and consequently the error bars, can be calculated via error propagation starting from equation 5.1. The errors deriving from L_2 and V_2 are considered negligible. In such a way the absolute error on the transverse energy value is given by

$$\delta E_{tr} = 2 \cdot \frac{V_2^2}{32\left(\sqrt{2(V_2 + 355)} - 26.646\right)^2} \cdot r \cdot \delta r \tag{5.9}$$

with δr depending on the simulation precision, hence on the mesh size.

Simulation precision

The simulation precision is of high importance as it defines the error on the simulation results. The area of the simulation layout that mostly affects the simulation results is certainly the grid region due to the micrometer size of the holes and the bars width. Special care must be taken in order to avoid edge effects and appropriately evaluate the electromagnetic field in the grid region.

For this reason a simulation varying the mesh size in the grid region for the case of the smallest grid, 25-5, was performed. The mesh sizes considered were: $5\,\mu$m, $3\,\mu$m, $2\,\mu$m and $1.5\,\mu$m.

The results show that no significant difference is present for the mesh sizes $3\,\mu$m, $2\,\mu$m and $1.5\,\mu$m. The envelopes for such mesh sizes all sit in a $3\,\mu$m range, with no clear up or down trend among the three. This shows that they lie in a noise region and that the $3\,\mu$ precision assumption can be considered valid. Furthermore, this proves that a $3\,\mu$m mesh cell size can be used for the simulations.

Space charge effect

Space charge effects often play a significant role in the beam transport of charged particles. The effect is emphasized when the beam, in the case of this study an electron beam, has high current and low energy.

It is also known that space charge effect can alter the I-V characteristics of the field emission process in CNTs. However, this effect is only visible at high current densities, e.g. several A/cm^2 [122]. This current density value is order of magnitudes higher than what is required by this work and this type of space charge limited emission is consequently non significant.

Space charge effects may however still affect the beam properties, especially during calculation of the beam transverse energy. For this reason a further simulation was designed in order to evaluate whether space charge effects should be considered significant.

In this simulation the same layout as in the previous simulations was used. The grid type used was 25-5 and the mesh size was of $3\,\mu$m. The simulation was performed with the “gun iteration” and “self-induced field” options enabled within the tracking solver. The “gun iteration” option is the one which allows inclusion of the space charge effect in the calculation, whilst the “self-induced field” option allows consideration of the magnetic field induced by the electron beam itself when calculating the electromagnetic field. The emission was set to be with fixed current, while the remaining beam properties were the same as in the grid simulations. The simulation was parametric so to vary the fixed current value and therefore the current density. The current density values considered were: 1.5 mA/cm^2, 15 mA/cm^2 and 150 mA/cm^2.

The simulation results have shown that no difference is present for any of the investigated cases. For such reason, the space charge effect can be considered negligible for the simulations performed and is no longer considered.

Inclusion of magnetic field contribution

The simulations performed do not include a magnetic field and are thus purely electrostatic.

The main reason why no magnetic was added, despite the electron gun of the electron cooler of ELENA being immersed in an axial magnetic field, is that this work tries to address the problem in a more general way and not only refers to the case of ELENA or electron cooling.

However, a further study with the addition of an external axial magnetic field was carried out to assess the possible impact of the magnetic field on the beam envelope. The simulation was performed with two possible magnetic field values; 1000 G, as in the expansion solenoid of the cooler of ELENA, and 100 G as in the remaining solenoids of the cooler of ELENA.

The simulation layout included a grid 25-5, a cathode-grid distance of 2 mm, an electric field in the extraction region of 2 V/μm and initial beam energy of 0.05 eV.

The beam envelope presented a slight variation in the case of the higher magnetic field, but the variation was below 3 μm, which can be considered negligible considering the simulation precision.

These results showed that the magnetic field can be neglected in the region of beam extraction and beam deceleration, which is the region considered in the simulation campaign.

5.2 Results and discussion

As in the previous section the results are grouped in the following categories:

- simulation 1: the effect of the cathode-grid distance

- simulation 2: the effect of the grid thickness
- simulation 3: the effect of the beam initial energy
- simulation 4: the effect of the applied electric field

This simulation work represents one of the most important milestones of this thesis work. The grid is one of the elements that most affects the beam properties and therefore needs to be extremely carefully studied. This simulation work served to define what are the target grid features which directed the research of suppliers for the most suitable grid types.

5.2.1 Simulation 1: the effect of the cathode-grid distance

From figures 5.3a and 5.3b it is possible to infer how the beam offset and the voltage standard deviation (%) both greatly decrease with the distance and for smaller hole grids. It is also noticeable from figure 5.3c how the beam offset is dependent on the voltage standard deviation (%). The reason for the increase of the beam offset when the voltage standard deviation increases is connected to the higher voltage fluctuations in the grid's holes, which translates in curvatures of the field lines that consequently lead to transverse components in the beam trajectory. This trend is reversed increasing the distance, since higher distance translates into smaller voltage fluctuations along the grid.

For the three cases an empirical fitting equation was found. For what concerns figure 5.3a, the fitting equation used is $y = a/x + 0.7a$. For figure 5.3b $y = ax^{-3/2} + c$ and finally, for figure 5.3c, the equation is $y = ax^{1/2}$. The fitting parameters and the coefficients of determination "R-squared" are summarised in tables 5.2, 5.3, and 5.4. The coefficients of determination "R-squared" served to assess the quality of the fit. From the "R-squared" values of all fits it can be noticed how the quality of the fits for grids $50 - 10$ and $25 - 5$, mostly in the case when the beam offset is plotted, is quite low compared to all other grid types. The reason is connected to the simulation precision. The precision for this set of simulations is in the order of $10\,\mu$m, this value is sufficient for grid types down to $150 - 30$ since the beam offset values for such grids are mostly over 100μm. This translates to a precision in the range of 4–10 %, depending on the grid distance, which proved to be sufficient to determine the trends with good precision. The fits for the

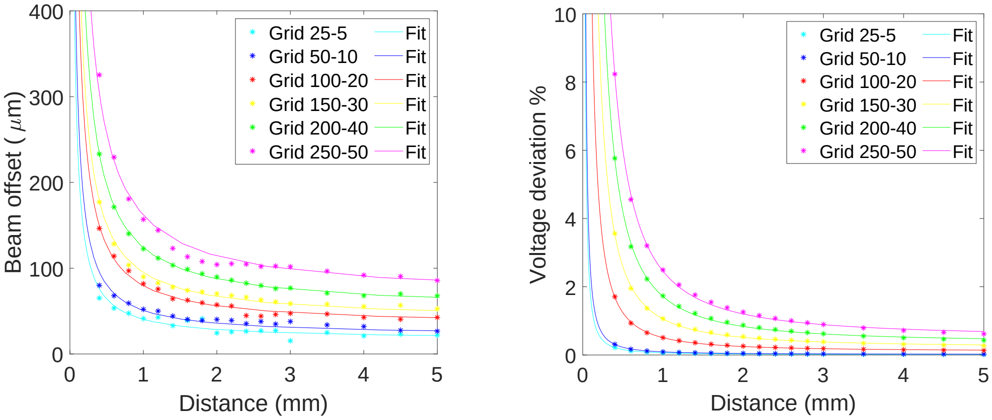

(a) Grid distance (mm) vs Beam Offset (μm). Fits are done with a power equation of the type: $y = a/x + 0.7a$

(b) Grid distance (mm) vs Voltage standard deviation (%). Fits are done with a power equation of the type $y = ax^{-3/2} + c$.

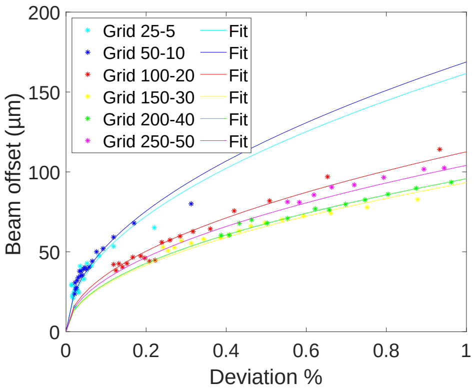

(c) Voltage standard deviation (%) vs Beam offset (μm). Fits are done with a power equation of the type $y = ax^{1/2}$.

Figure 5.3: Analysis of the beam offset and voltage deviation % as functions of the cathode-grid distance.

Table 5.2: Fitting parameters “a” and coefficients of determination “R-squared” for the fitting equations of figure 5.3a

Grid type	a	R-squared
25 – 5	23.74	0.7901
50 – 10	29.83	0.877
100 – 20	46.71	0.9855
150 – 30	55.82	0.9885
200 – 40	72.9	0.998
250 – 50	95.07	0.9837

Table 5.3: Fitting parameters “a” and “c” and coefficients of determination “R-squared” for the fitting equations of figure 5.3b

Grid type	a	c	R-squared
25 – 5	0.05198	0.01225	0.9987
50 – 10	0.07333	0.01923	0.9988
100 – 20	0.4008	0.1069	0.9988
150 – 30	0.838	0.2202	0.9988
200 – 40	1.36	0.3553	0.9989
250 – 50	1.944	0.5149	0.9988

two smallest grids exhibit instead a significantly lower fit quality. In general, the reliability of all the fits can still be considered relevant due to the high number of data points spanning in a wide distance range, 0.4–5 mm. This precision problem is mostly related to the plots describing the beam offset, where the 10 μm sensitivity holds. In figure 5.3b, where the voltage standard deviation (%) is plotted as a function of the grid distance (mm), the precision problem vanishes, since the sensitivity of the voltage standard deviation (%) is instead negligible; as it is possible to infer from the “R-squared” values reported in Table 5.3, which are all above 0.99.

What it can also be inferred from figure 5.3a and its fitting equation is how the beam offset is proportional to the inverse of the distance. The hole size instead affects the pre-power coefficient and and the intercept value, while it has no impact on the power coefficient. Where the pre-power coefficient, the power coefficient and intercept are respectively “a”, “b”, “c” in the power

Table 5.4: Fitting parameters “a” and coefficients of determination “R-squared” for the fitting equations of figure 5.3c

Grid type	a	R-squared
$25 - 5$	161.6	0.7817
$50 - 10$	168.8	0.8956
$100 - 20$	112.6	0.9837
$150 - 30$	93.29	0.9846
$200 - 40$	95.73	0.9972
$250 - 50$	104.1	0.9718

equation: $y = ax^b + c$. From figure 5.3b and table 5.3, it is noticeable how the voltage deviation % along the grid plane never goes to zero even when the distance increases to infinity. However, the residual voltage deviation becomes smaller and smaller if the hole size decreases. The fits used for figure 5.3c has also been added, however it is just been used to present the remaining findings in a clearer way.

It was also possible to quantify the transverse energy increase due to the passage of the beam through the grid using equation 5.1 in order to study its variation when using each grid and depending on the distance. The beam initial transverse energy was linearly subtracted. The results are shown in figure 5.4.

The empirical fitting equation is of the type $y = a/x^{3/2} + 1.5a$. The fitting parameters and the coefficients of determination “R-squared” are listed in table 5.5.

The “R-squared” values show a lower goodness of the fit compared to the previous case, especially for the two smallest grids. For such grids the further decreased fits’ goodness is connected to the lower simulation precision, as discussed above. In general, the calculation of the transverse energy leads to an increase on the calculations’ error and consequent lowering of the results’ precision. This is made clear through evaluation of the error bars, from which it can be noticed how the precision concerning the transverse energy values is not optimal, especially for the smallest grids.

The values of the additive parameter in the fitting equation also show that for all grids the minimum transverse energy acquired by the electron beam due to the grid effect never goes to zero. For grids $250 - 50$ and $200 - 40$,

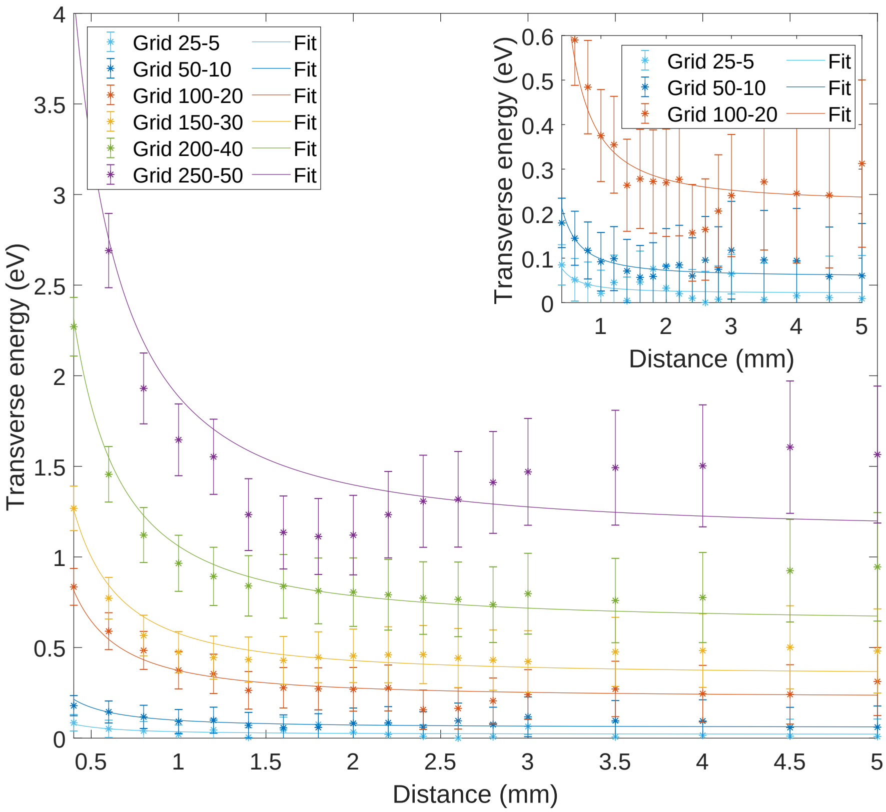

Figure 5.4: Grid distance (mm) vs Transverse energy due to the grid (eV). Inset: magnification for better showing the behaviour of the grids $100-20$, $50-10$ and $25-5$. All fits are done with a power equation of the type: $y = a/x^{3/2} + 1.5a$.

Table 5.5: Fitting parameters “a” and coefficients of determination “R-squared” for the fitting equations of figure 5.4. Distance (mm) vs Transverse energy due to the grid (eV). Equation: $y = a/x^{3/2} + 1.5a$.

Grid type	a	R-squared
$25 - 5$	0.0142	0.3721
$50 - 10$	0.03925	0.5587
$100 - 20$	0.1494	0.918
$150 - 30$	0.2311	0.8616
$200 - 40$	0.424	0.9178
$250 - 50$	0.7541	0.8852

the values at high distances show an upward behaviour, this is most likely due to a non-perfect field alignment when the distance approaches 5 mm.

These calculations served to understand whether the use of any of the investigated grids can fulfill the requirements in terms of maximum beam transverse energy spread. From the inset in figure 5.4 it is evident that the only suitable grids are grids $50-10$ and $25-5$ at distances greater than 1 mm. All other grids add a transverse kick that is too significant at every feasible inter-electrode distance. Therefore, in the remaining simulations only grids $50 - 10$ and $25 - 5$ were considered.

From simulation 1 it was possible to investigate the current emitted from the cathode depending on the grid distance and the grid type. Two main data for each instance of the parametric simulation were extracted: the emitted current and the beam current after the grid. In such a way the grid transparency could be estimated. Prior to performing the grid transparency calculation the amount of current losses in the spacer was calculated for each data set and eliminated from the transparency calculations. The beam current loss in the spacer was also found to be dependent on the cathode-grid distance and on the grid type. In general, the beam loss in the spacer amounted to percentage values up to 1 %. From figure 5.5a it is possible to infer how the emitted current increases at higher grid distance until reaching a plateau. This behavior is shown in every grid type. It is also possible to notice that for smaller holes this effect, while still visible, is considerably limited. In particular, for grid $25 - 5$ the effect is greatly reduced, making this grid type more stable at every distance for what concerns current

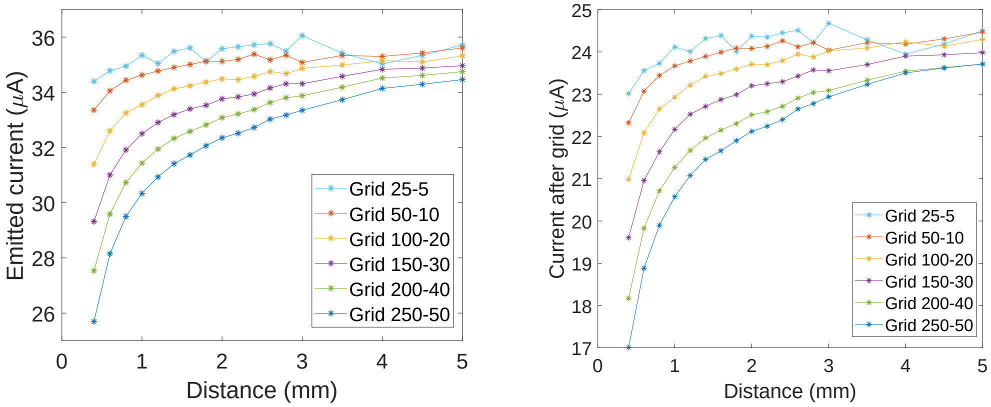

(a) Emitted current (μA) as a function of the grid distance (mm) for all grid types.

(b) Current passing through the grid (μA) as a function of the grid distance (mm) for all grid types.

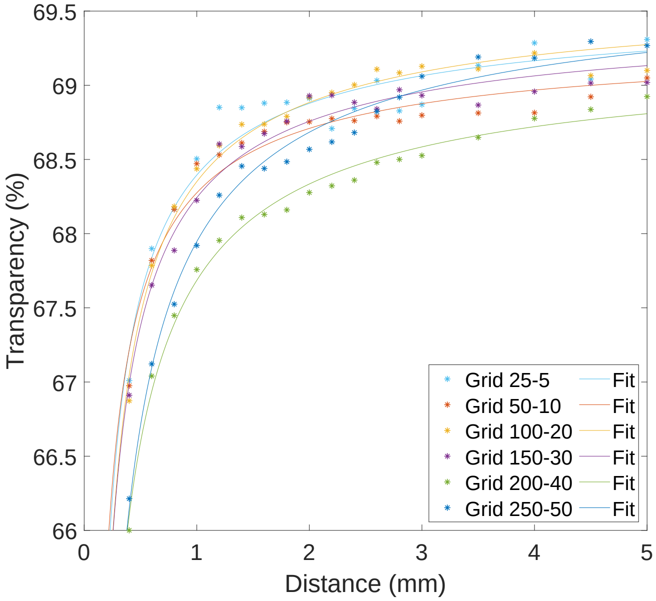

(c) Transparency (%) of all grids depending on the grid distance (mm). In the latter the fits are performed with a power equation of the type: $ax^{-0.75} + c$.

Figure 5.5: Emitted current and grid transparency as a function of the grid distance and the grid type.

Table 5.6: Fitting parameters “a” and “c” and coefficients of determination “R-squared” for the fitting equations of figure 5.5c. Grid distance (mm) vs Grid transparency (%). Fitting equation: $y = ax^{-0.75} + c$.

Grid type	a	c	R-squared
$25 - 5$	-1.193	69.59	0.9224
$50 - 10$	-1.071	69.35	0.9483
$100 - 20$	-1.318	69.67	0.9773
$150 - 30$	-1.27	69.51	0.9684
$200 - 40$	-1.603	69.29	0.9892
$250 - 50$	-1.819	69.77	0.9868

emission and transparency. The same behavior can be inferred from figure 5.5b, as expected. Finally, it is noticeable the same trend for the grid transparency (%), showing that at small distances the transparency of a grid is lower than the transparency of the same grid at a higher distance from the cathode. In figure 5.5c, the data were fitted with a power equation of the type $y = ax^{-0.75} + c$. The values found for the fitting parameters “a” and “c” are listed in table 5.6. The fits present a good coefficient of determination “R-squared”, proving the high goodness of the fits. From the “c” parameters can be further calculated the maximum transparency reachable with all grid types. Despite some little variation, mostly connected to the sensitivity of the simulations, the mean maximum transparency proved to be $69.5 \pm 0.2\%$.

This effect can be reconnected with the differences in the emitted current depending on the distance. If the grid is closer to the cathode, and especially for larger hole sizes, the emission is inhibited. This can be explained via geometrical and electric field considerations. If the hole is too close to the cathode surface, the current emitted in its direction will be smaller as there are deviations of the voltage in the grid holes, which translate in a smaller electric field in direction of the hole itself. This phenomenon is enhanced for smaller distances and bigger hole sizes and needs to be carefully considered if the grid distance is lower than 1 mm, as this can drastically affect the beam current.

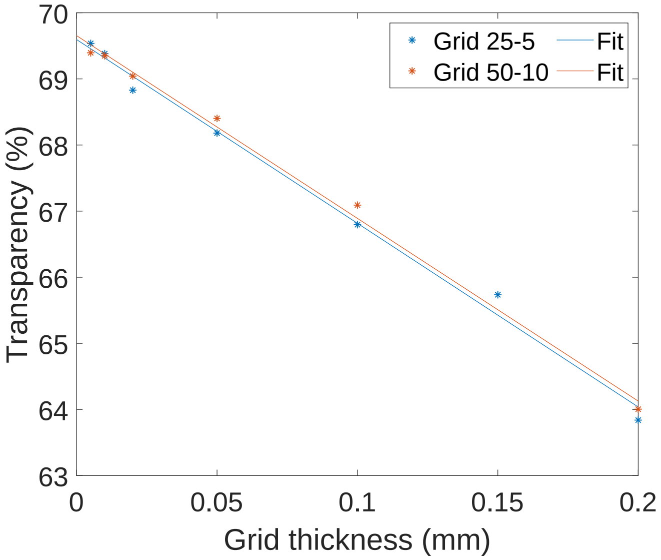

Figure 5.6: Grid transparency (%) as a function of the grid thickness (mm). The fits have been done with a linear equation of the type $y = -27.7x + c$.

5.2.2 Simulation 2: the effect of the grid thickness

For making grids with such small features it is often necessary to limit the grid thickness. This is related to manufacturing requirements. The grid thickness mostly affects two parameters: the grid transparency, which will decrease when the thickness increases, and the beam transverse energy, that in principle should instead decrease when the grid thickness increases. For grids having features as small as 10's μm thickness limitations can be quite strict. Depending on the process used for making the holes the possible thickness typically varies from $5-10\,\mu$m up to roughly $200\,\mu$m, according to a research with multiple suppliers. This is quite a wide range and depending on the chosen value the effect on the beam properties can be quite significant and needs to be evaluated.

The impact of the grid thickness on the grid transparency is shown in figure 5.6. The beam current lost in the spacer has also been included in the calculations.

The grid thickness was scanned between $5\,\mu$m and $200\,\mu$m, while keeping the cathode-grid distance set to 1 mm. The choice of the grid thickness values is based on a research of the main suppliers of micro-meshed grids and on the

Table 5.7: Intercept values “c” and coefficients of determination “R-squared” for the fitting equations of figure 5.6. Grid thickness (mm) vs Grid transparency (%). Equation: $y = -27.7x + c$.

Grid type	c	R-squared
$25-5$	69.59	0.9929
$50-10$	69.66	0.9958

responses received about the possible grid thicknesses. Figure 5.6 shows how the grid transparency rapidly decreases from about 70%, when the thickness approaches 0, to values as low as 64%, when reaching a thickness of 200 μm. The trends for grids $25-5$ and $50-10$ are identical and follow a linear equation of the type $y = -27.7x + c$. The values of the intercept “c” are almost identical showing how the two grids perform similarly. The intercept values and “R-squared” value are reported in table 5.7. The intercepts have extremely similar values, 69.59 and 69.66, whilst the R-squared values show in both cases an ideal goodness of the fits with values over 0.99.

Finally, the impact of the grid thickness on the beam transverse energy is evaluated in figure 5.7.

What it can be inferred from figure 5.7 is how the beam transverse energy values for grid $50-10$ are all above the 0.1 eV threshold for all the grid thicknesses considered, even taking into account the error bars. The grid distance here is only 1 mm, suggesting that the beam transverse energy would go below 0.1 eV at higher distances. The results achieved with grid $25-5$ are more promising, from the figure it is noticeable how the transverse energy values are all well below 0.025 eV, also considering the error bars. For these simulations the beam initial energy is set to 0 eV, which cannot reflect the reality, but the results are promising considering a grid distance of only 1 mm. For both grids the fits are performed with a power equation of the type $y = ax^{-b}$. In this case, the intercept value was not included in the fitting equations, due to physics considerations. When the grid thickness is approaching 0 the transverse energy increases to infinite, which is the expected behaviour. Similarly, when the grid thickness goes to infinite, the transverse energy would go to 0 eV, since all electrons with transverse energy above 0 eV will at some point hit the grid. These assumptions are both valid considering that the beam initial energy is set to 0 eV. Moreover, the grid

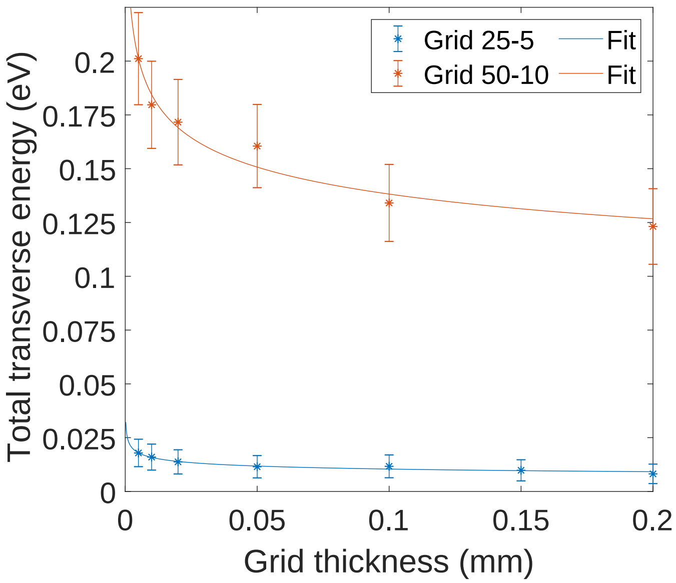

Figure 5.7: Beam transverse energy (eV) as a function of the grid thickness (mm). The fits have been done with a power equation of the type $y = ax^{-b}$.

distance is set to 1 mm, hence at a higher distance the results would further improve. The values for the pre-power coefficient, the power coefficient and "R-squared" are listed in Table 5.8. In this case the "R-squared" values show a high goodness of the fits with values over 0.96.

In figure 5.7 and table 5.8 the dependency of the beam transverse energy on the grid thickness is highlighted: for grid $25-5$ $E_{tr} \propto x^{-0.182}$, while for grid $50-10$ $E_{tr} \propto x^{-0.1253}$. The "a" coefficient is mostly dependent on the electric field value, the grid distance and the grid features, such as the hole

Table 5.8: Fitting parameters "a" and "b" and coefficients of determination "R-squared" for the fitting equations of figure 5.7. Grid thickness (mm) vs Beam transverse energy (eV). Fitting equation: $y = ax^{-b}$.

Grid type	a	b	R-squared
$25-5$	0.00685	0.182	0.96
$50-10$	0.1036	0.1253	0.9636

size.

These simulations have been performed with higher precision compared to the previous one. In this case the sensitivity was of about $3\,\mu$m. While the previous precision used was working well with grids with larger holes, in the case of the two grids used in this simulation a much higher precision proved to be essential in order to achieve repeatable and reliable results.

Considering the optimal results achieved for grid $25-5$ the next simulations will only be run on this grid type.

5.2.3 Simulation 3: the effect of the beam initial energy

Simulation 3 served to investigate how the beam transverse energy changes if the beam initial transverse energy varies. The simulation is ran only on the smallest grid, $25-5$, since this is the best suited considering the results obtained so far. The results of this simulation are shown in figure 5.8. The simulation sensitivity used is $3\,\mu$m.

From figure 5.8 it can be seen how the beam initial energy affects the beam transverse energy. The equation used for the fits is of the type $y = ax^{-1.5} + E_i$. It is noticeable how in this case, as for all other grids, the beam transverse energy is proportional to the distance at the power of -1.5. For this particular grid it can also be inferred from the fits how for infinite grid distance the transverse energy converges to the beam initial energy. This behaviour was not valid for all other grids and depends on the hole size. The inclusion of a further additive transverse energy was investigated while researching the best fitting equation, but its value was below 0.005 eV for each beam initial energy step and the goodness of the fit, the “R-squared”, was never improved by more than 0.01. The coefficient “a” and the “R-squared” values are listed in table 5.9.

The “R-squared” values in table 5.9 indicate a significant goodness of the fits, which however seldom overcome the 0.9 threshold. From figure 5.8 it can be seen how the data points that are less consistent with the fits are always relative to the same grid distances. Those are the most responsible for the relatively low “R-squared” values. Such points are relative to the grid distances $0.6, 1.4$ and 1.8. For $d = 0.6, 1.4$ the total transverse energy values are always lower than the fit, while for $d = 1.8$ the total transverse energy values are always higher than the fit. This is a reproducible behaviour

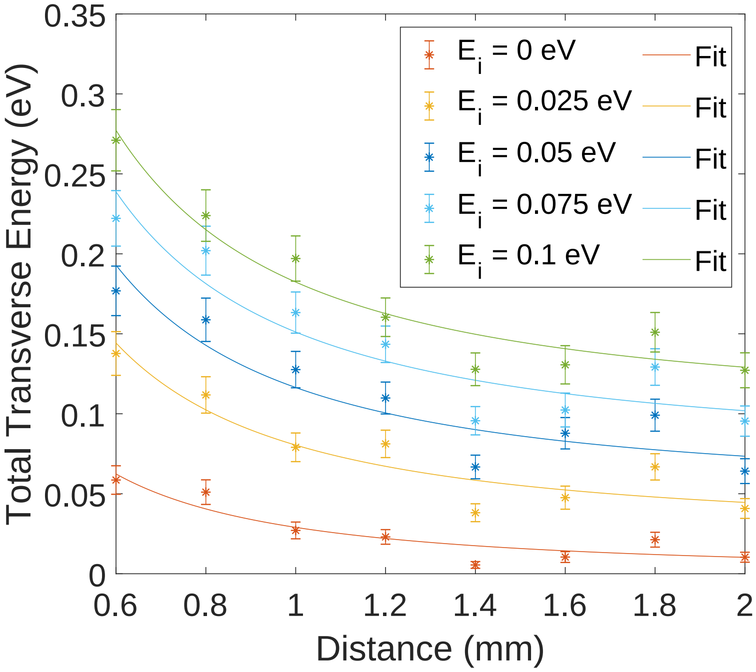

Figure 5.8: Beam transverse energy (eV) as a function of the grid distance (mm). The fits have been done with a power equation of the type $y = ax^{-1.5} + E_i$.

Table 5.9: Fitting parameters "a" and coefficients of determination "R-squared" for the fitting equations of figure 5.8. Grid distance (mm) vs Total transverse energy (eV) at different beam initial energies. Fitting equation: $y = ax^{-1.5} + E_i$.

Energy (eV)	a	R-squared
0	0.029	0.8574
0.025	0.05543	0.8693
0.05	0.06643	0.8422
0.075	0.07613	0.8628
0.1	0.08237	0.9376

Table 5.10: Fitting parameters “a” and coefficients of determination “R-squared” for the fitting equations of figure 5.9. Grid distance (mm) vs Voltage standard deviation (%) and Grid distance vs Maximum voltage deviation (%). Equation: $y = ax^{-1.5}$.

	a	R-squared
Standard deviation	0.0003852	0.9817
Maximum deviation	0.005978	0.9904

throughout all the data points included in this simulation. The reason for this behaviour is presumably connected to geometrical factors, which may alter the beam trajectory of the outer electrons in the simulation at such distances. No other parameter apart from the grid distance and the beam initial energy were changed during the simulation, whilst the same discrepancies arise at the same distances and similarly for each beam initial energy step. These sudden changes do not reflect a real change of the total transverse energy. This is also supported by a study of the voltage standard deviation (%) and voltage maximum deviation (%) along the grid for all distances shown in figure 5.9. The fitting parameters “a” and “R-squared” values are listed in table 5.10. The fits have high coefficients of determination, above 0.98, proving their goodness and the fitting equation is for both the same used for the other grids in the first simulation type. The results show that no unexpected effect takes place at those distances, nor in terms of the voltage standard deviation nor in terms of the maximum voltage deviation, suggesting that the observed transverse energy changes may be neglected. Interestingly, the only grid distance at which a slight change is visible away from the main trend is $d = 1.2$ mm. This has not caused significant variations in the evaluation of the beam transverse energy.

Finally, from this study on grid $25 - 5$ it can be shown that the total transverse energy of the electron beam successfully remains below the 0.1 eV threshold for any distance if $E_i = 0$, from 0.8 mm for $E_i = 0.025$ and from 1.5 mm for $E_i = 0.05$. More precisely, in the case of $d = 2$ mm, the total transverse energy of the electron beam would be

- $E_i = 0 \implies E_{tr} = 0.010$ eV. 90% less of the threshold value 0.1 eV.
- $E_i = 0.025 \implies E_{tr} = 0.045$ eV. 55% less of the threshold value 0.1 eV.

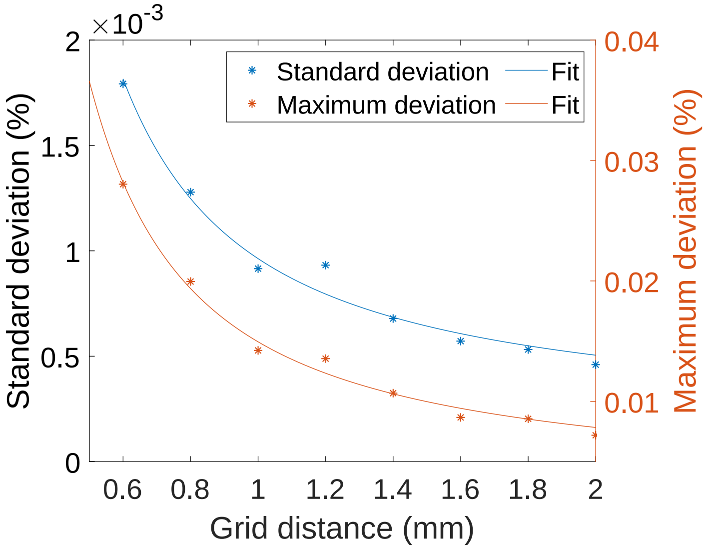

Figure 5.9: Voltage standard deviation (%) along the grid and voltage maximum deviation (%) as a function of the grid distance (mm). The fits have both been done with a power equation of the type $y = ax^{-1.5}$ as for all the other grids.

- $E_i = 0.05 \implies E_{tr} = 0.073$ eV. 27% less of the threshold value 0.1 eV.

5.2.4 Simulation 4: the effect of the applied electric field

Simulation 4 is directed to assess the effect of an increase of the electric field on the beam total transverse energy. This has a two-fold importance. Firstly, the electric field is what drives emission in field emitters, thus the electric field strictly defines the emitted current of a particular cathode. Secondly, if a cathode is used for a long time, in the order of hundreds/thousands of hours, it can be that in order to keep the current stable the electric field must be controlled accordingly. In particular, because of the emitter ageing, a stronger electric field might be required in order to extract the desired.

In order to conduct the investigation a double parametric simulation was performed, changing both the grid distance and the electric field. The grid distance was varied between 0.6 mm and 2 mm, whilst the electric field was varied between 2.5 V/μm and 6 V/μm. In such a way it was possible to study how the total transverse energy varies increasing the grid distance and applying different electric fields (figure 5.10).

In figure 5.10, the fit was performed with the equation $y = ax^{-3/2}$. The dependence on the distance observed in the previous cases seems to be valid in this case as well. This time, a fit without a parameter "c" was performed, since at $x = 0$ there would be no current emission and at the same time no voltage fluctuations on the grid. The values of the parameter "a" and the "R-squared" values are listed in table 5.11.

From figure 5.10 and table 5.11 it can be noticed that the error bars are quite large compared to the previous case (beam initial energy simulation 5.8) and the goodness of the fits, while comparable, appears to be slightly lower. This is mostly due to the higher error on the transverse energy calculation. While the simulation precision is the same in this case as in the previous one (3μm), when calculating the error on the transverse energy the propagation is higher in this case. This is visible in equation 5.9. In this case the values of r, partly, and most importantly the values of V_2, are much higher due to the higher applied electric field. This translates in higher calculation errors, which will increase at every iteration of the applied electric field.

Nevertheless, the trends show an acceptable goodness with the expected distance proportionality: $\propto d^{-3/2}$. Furthermore, it is noticeable how the data

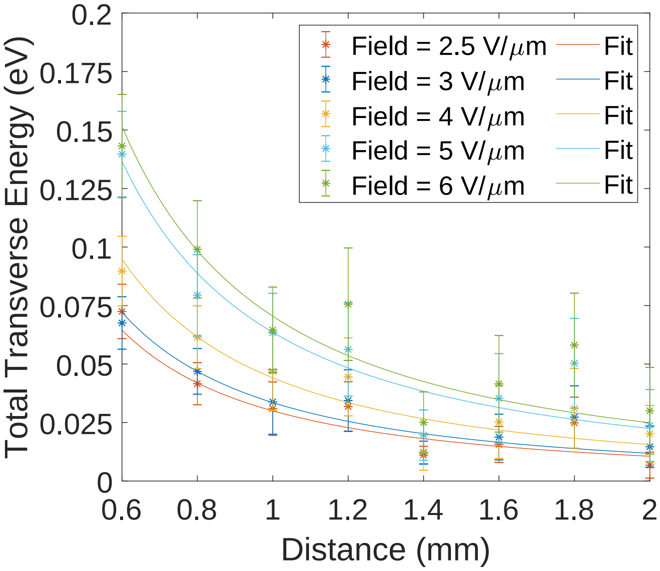

Figure 5.10: Beam total transverse energy (eV) as a function of the grid distance (mm). Fits performed with a power equation of the type: $y = ax^{-3/2}$.

Table 5.11: Fitting parameters "a" and coefficients of determination "R-squared" for the fitting equations of figure 5.10. Distance(mm) vs Total transverse energy (eV) at different applied electric fields. Equation: $y = ax^{-3/2}$.

Electric field (V/μm)	a	R-squared
2.5	0.02999	0.8811
3	0.03353	0.8493
4	0.04408	0.875
5	0.06355	0.8934
6	0.07045	0.8323

Table 5.12: Transverse energy values for different applied electric fields for a grid $25-5$ at a distance of 2 mm from the cathode.

Electric field (V/μm)	Transverse energy (eV)
2.5	0.011
3	0.012
4	0.016
5	0.023
6	0.025

points that are farther off the fits are relative to grid distances: $0.6, 1.2, 1.4, 1.8$. These are the same grid distances listed in the previous case with the addition of $d = 1.2$, which, as also showed in the previous case, did show a peculiar voltage deviation on the grid. In this case, due to the higher electric field values, this behaviour was enhanced.

In general, it can be seen how the beam transverse energy values rise when increasing the applied electric field. This was expected as at a higher electric field corresponds a higher voltage applied on the grid. This in turn translates to higher voltage deviations on the grid itself and a higher effect on the beam transverse energy. Nevertheless, the beam transverse energy values tend to converge when the distance increases.

For $d = 2$, according to the fits, the expected transverse energy values are listed in table 5.12.

Considering the required current output it is not expected to ever apply an electric field higher than about 4 V/μm. Meaning that the higher transverse energy value increase, when compared to the case of $Field = 2$ V/μm, would be of about 0.006 eV. The “R-squared” value in this case was of about 0.85, indicating that this value can be considered valid with a certainty of about 85%.

Chapter 6

Design of a possible CNT-based electron gun

In this chapter a possible gun design is reported. The aim of the design process was to reduce any possible contribution to the beam transverse energy, effectively trying to model a low-energy cold electron gun. Whilst in this thesis the aim is using CNTs, the gun design is valid for any field emitting array and virtually for any field emitting cathode, taking into account that the values of the electric field necessary for the electron beam extraction may considerably vary.

The gun design was based on the results achieved with the previous experiments and simulations and by ad-hoc simulations aiming at defining the shape and size of each of the electron gun components.

As described in the previous sections, the grid plays one of the most significant roles in the gun layout and special care is required to determine its placing, shape and size.

The cathode layout also plays a role in obtaining an emission region with straight field lines, thus permitting to avoid transverse kicks, and must therefore be carefully designed.

Finally, a possible gun layout is proposed after an optimization of all the electrodes' shapes and sizes.

6.1 Grid

The hole size and the bar width have been finally set respectively to 15 μm and 3 μm. The research of a supplier who could make such a grid was a challenge, since this is a high precision and somewhat uncommon job. The chosen supplier lastly was “Micro Create” [123], an independent company specialized in clean room fabrication.

The grid will be made out of a highly doped silicon wafer with a thickness of 500 μm and a diameter of about 10 cm. The wafer is then thinned down to 50 μm in a central area of 6 cm × 6 cm and the hole pattern is realized in the center of it on an area of 3 cm × 3 cm. The reason for a thinner central area is connected to technical limitations when etching holes with such an aspect ratio, whilst starting with a thicker wafer has the goal to improve the mechanical strength of the component.

Having holes of about 15 μm will further decrease the impact of the grid on the beam final transverse energy, when compared to the results achieved via simulation of the $25-5$ grid type. This translates into better performance of the gun. A further parametric simulation was also performed on this new grid type in order to precisely evaluate its effect on the beam transverse energy.

Figure 6.1 shows the results relative to the calculation of the total beam transverse energy after passing through a grid 15-3 depending on the grid distance and beam initial energy. The simulation layout is identical to the one used in chapter 5 for simulation of the other grids. These results show that this grid type doesn’t significantly affect the beam transverse energy, with only a minimal effect at an inter-electrode distance of 0.6 mm and virtually no effect at higher distances. This makes this grid type almost transparent for the electron beam in this setup. This effect holds unvaried for beam initial energies of 0.025, 0.05 and 0.075 eV. For this simulation campaign the mesh size around the grid plane was further decreased to 2 μm in order to increase the number of mesh cells in the grid holes and ensure an unaltered simulation precision.

From the same simulation it was also possible to calculate the grid transparency. The fit was performed with a power equation of the type $y = ax^{-0.75} + c$ as for the case of the previous grid types. The fit goodness “R-squared” was 0.9575, indicating a good agreement with the data points. The results are shown in figure 6.2. As it is possible to infer from figure 6.2, the transparency varies between about 67 % for a grid distance of 0.6 mm and

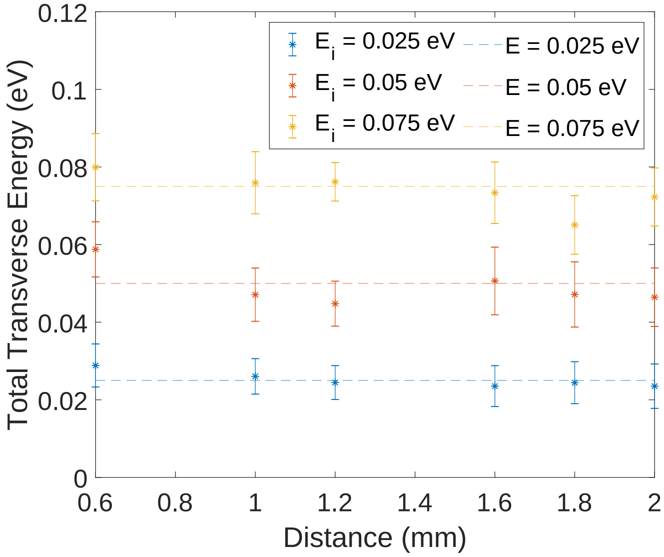

Figure 6.1: Beam total transverse energy (eV) as a function of the beam initial energy (eV) for different grid distances.

Table 6.1: Fitting parameters "a" and "c" and coefficients of determination "R-squared" for the fitting equations of figure 6.2. Grid distance (mm) vs Grid transparency (%). Fitting equation: $y = ax^{-0.75} + c$.

Grid type	a	c	R-squared
$15 - 3$	-1.726	69.42	0.9575

68.5 % for a grid distance of 2 mm. From the fitting formula it is possible to estimate a grid transparency of 69.42 % when the grid distance approaches infinity. This value is in good agreement with the results obtained for the other grid types. The fitting parameters are listed in table 6.1.

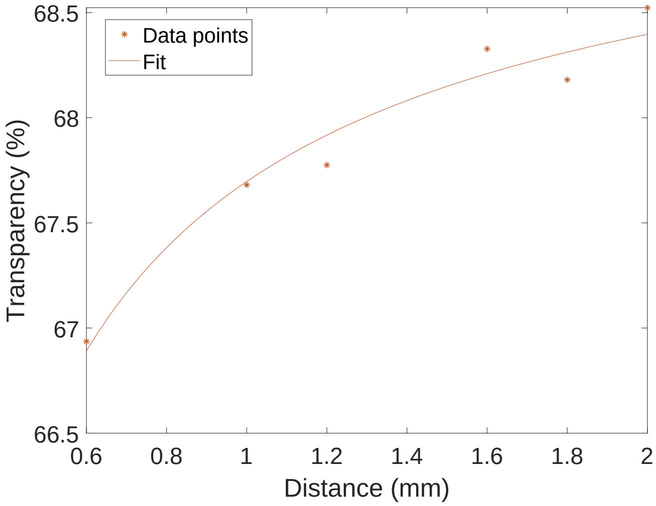

Figure 6.2: Transparency (%) as a function of the grid distance (mm). Fit performed with a power function of the type $y = ax^{-0.75} + c$.

6.2 Grid layout and grid tilting

Another possible solution concerning the grid layout that was considered was to manufacture a smaller grid component and then frame it with an additional electrode. This could improve the grids mechanical strength and make it easier to handle. However, simulations of this arrangement have suggested that this could lead to further complications connected to grid tilting and electrical connections.

The two cases were simulated introducing a grid tilting into the simulation layout already used for the previous simulations. There are two simulation types:

- Case 1: Grid with frame. Only the grid is tilted in respect to the grid frame and the supporting cathode-grid spacer;
- Case 2: One-component grid. It is only tilted in respect to the supporting cathode-grid spacer.

The beam spot uniformity was then investigated. This was done using CST for simulation and plotting the particles transverse position. The monitor planes investigated were just after the cathode, and just before the anode.

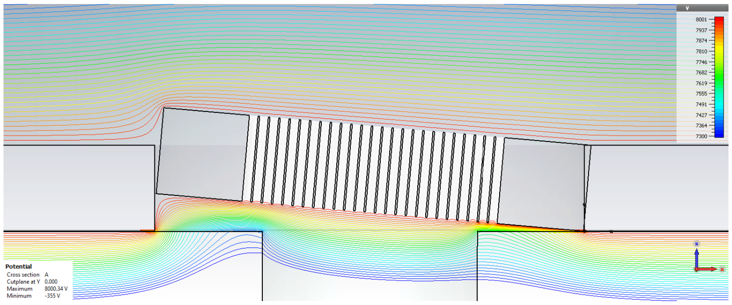

(a) Case 1: grid + frame. Tilt = 5°.

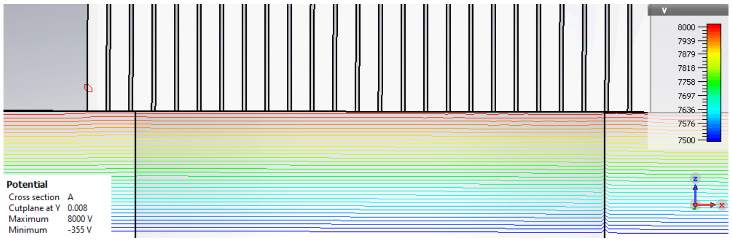

(b) Case 2: single electrode grid. Tilt = 0.2°.

Figure 6.3: Field lines plot for the two cases of grid tilting.

A comparison of the field lines for the two cases, when the tilting is at its maximum considered value was exported from CST and reported in figure 6.3. Here it is possible to see how the tilting in the case of a framed grid can be disruptive for the flatness of the field lines.

A parametric simulation was performed varying two parameters: the grid tilt and the beam initial energy, E_i. In such a way, the effects of the two parameters could be determined separately. In order to make the data visualization as clear as possible the data analysis was performed making a histogram of the data points composing the beam spot and using the map view for visualization with a gray-scale colormap. The histogram is composed of 50×50 bins equally distributed along the plot. This strategy permitted us to have a histogram plot that resembles an intensity plot, which is in turn very similar to a black and white image of the beam spot.

Precisely measuring the tilting of a grid in an experimental setup is not straightforward. However, the displacement can be expected to be in the range $50 - 200\,\mu$m. Additionally, the grid tilting is hardly relative to one

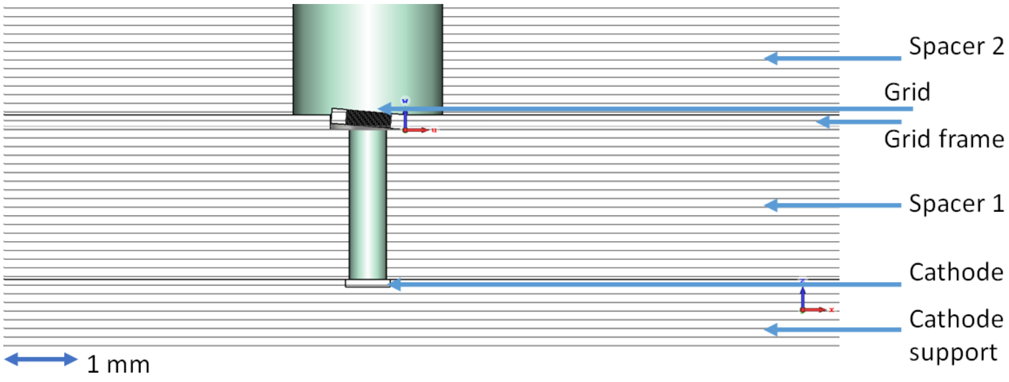

Figure 6.4: CST model view for the grid tilting of Case 1: framed grid.

plane only. This imposes tight constraints on the analysis, but allows an estimation of the possible issues arising in the simple case of a single plane tilting.

6.2.1 Case 1: grid with frame

The CST model regarding this case is illustrated in figure 6.4.

The grid tilt values were: 1°, 3° and 5°, which corresponds to a grid displacement respectively of about 15 μm, 50 μm and 90 μm. The beam initial energy, E_i values were: 0 eV, 0.03 eV and 0.075 eV.

To be able to perform the simulation with a high precision of about 3 μm, there was the constraint of keeping the grid size as small as possible. In this case the grid diameter was only of 0.5 mm. This means that a 5° tilting would lead to a grid displacement of only 90 μm in this particular case, on the other hand a 5° tilting would represent an exaggeration for a bigger grid. Nonetheless, it nicely serves to understand the possible impact of the grid tilting using this arrangement.

In figure 6.5 how the beam spot looks like right after the emission from the cathode is shown. This does not appreciably changes when varying the grid tilting and the beam initial energy.

As it is possible to see from both figures the particle density is homogeneous.

When the beam passes through a tilted grid its shape is modified due to the angle at which the grid holes are placed in relation to the beam longitu-

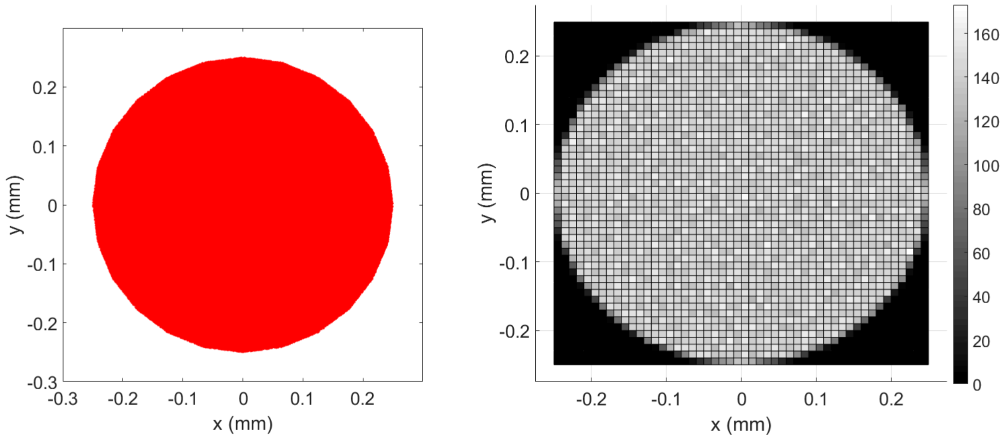

(a) (b)

Figure 6.5: Case 1. Beam spot right after emission from the cathode. (a) Particles position on the x axis vs particle position on the y axis. (b) Histogram plot of the particles density.

dinal trajectory and due to the distortion of the field lines at the interface spacer-grid. The results corresponding to a tilting of 1° are reported in figure 6.6. Each figure corresponds to a different beam initial energy value, which are 0 eV, 0.03 eV and 0.075 eV.

What is firstly apparent is that the beam is partly hollow, meaning that the electron density in the central region is less than the electron density in the outer region. This phenomena is further increased when the beam initial energy increases. Furthermore, it can be seen that in the outer region the beam density is not uniform, as there is an increased particle density on the left side, the part where the grid is detached from the spacer. This is due to the field lines distortion in the spacer-grid contact area that provokes curvatures of the electrons trajectory. In such a way the electrons can more easily pass trough the tilted grid holes.

The results obtained for a tilting of 3° and 5° are shown in figures 6.7 and 6.8.

What can be determined from the results obtained at higher tilting is how the increased tilting angle of the grid translates in a more hollow beam. The majority of the electrons are placed in the outer region, mostly in the left side. With the edges being even thinner when the beam initial energy

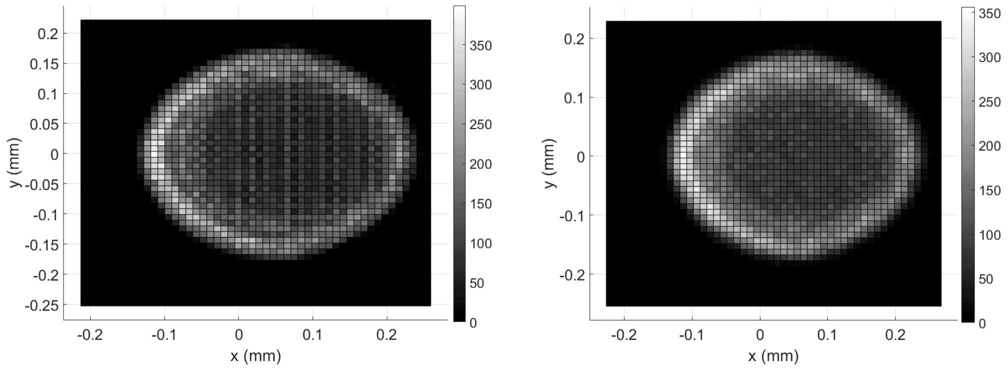

(a) Tilt = 1°, $E_i = 0$ eV. (b) Tilt = 1°, $E_i = 0.03$ eV.

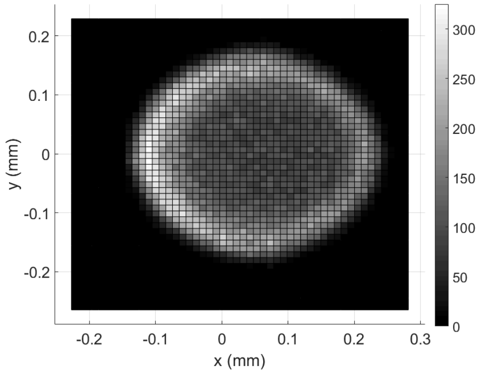

(c) Tilt = 1°, $E_i = 0.075$ eV.

Figure 6.6: Case 1. Effect of a 1° grid tilting for different initial beam energies.

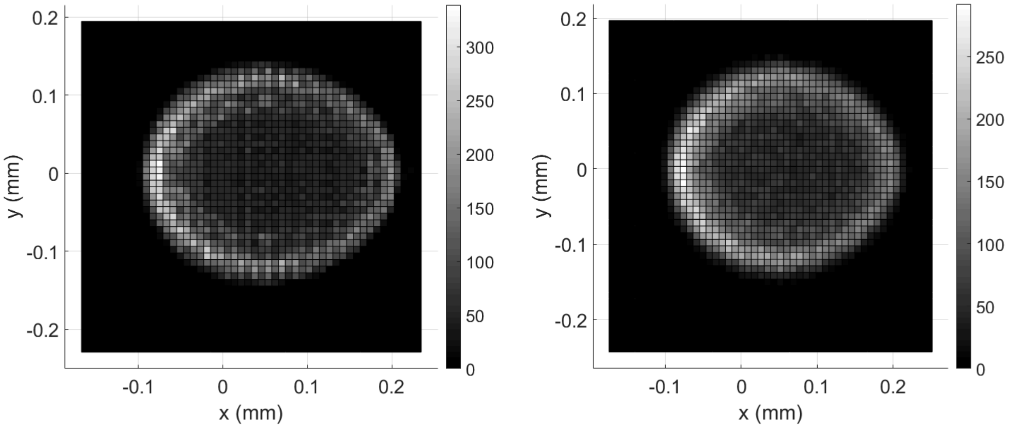

(a) Tilt = 3°, $E_i = 0$ eV.

(b) Tilt = 3°, $E_i = 0.03$ eV.

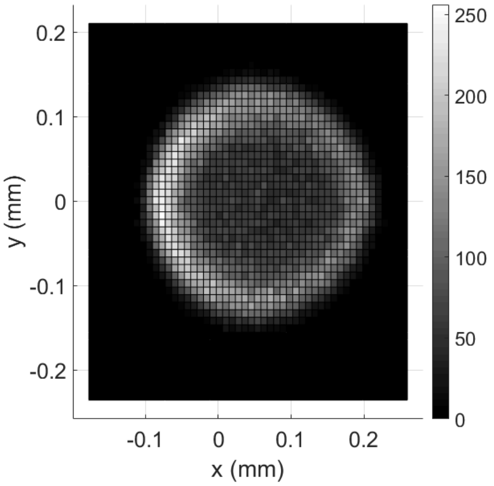

(c) Tilt = 3°, $E_i = 0.075$ eV.

Figure 6.7: Case 1. Effect of a 3° grid tilting for different initial beam energies.

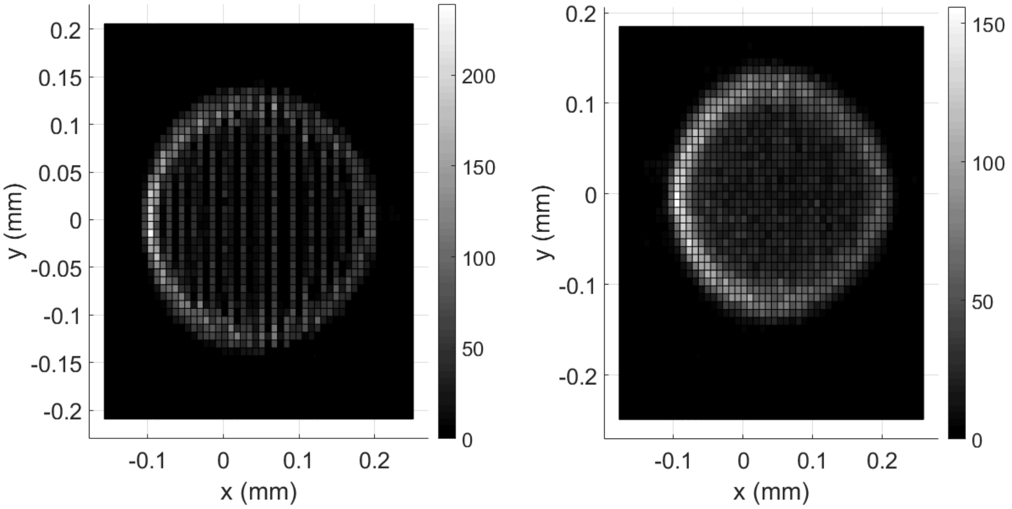

(a) Tilt = 5°, $E_i = 0$ eV.

(b) Tilt = 5°, $E_i = 0.03$ eV.

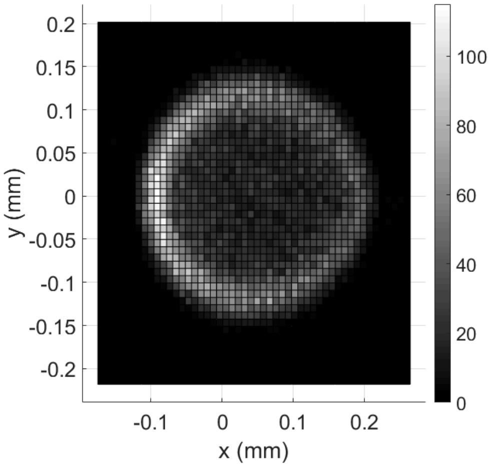

(c) Tilt = 5°, $E_i = 0.075$ eV.

Figure 6.8: Case 1. Effect of a 5° grid tilting for different initial beam energies.

is lower. This is due to the higher number of electrons that have close to zero transverse trajectory component, as they are more easily lost hitting the hole walls. At the edges, as stated beforehand, the field lines change the electrons' direction, facilitating their passage through the tilted grid holes.

6.2.2 Case 2: one-component grid

In this case the grid was as big as the spacer. The tilting was therefore relative to the whole extension of the grid electrode. The tilting options investigated are:

- tilt = 0
- tilt = 0.02°, which is equal to about 17 μm displacement. This is the closest option to the reality, according to precision reachable via common manufacturing techniques
- tilt = 0.05°, which is equal to about 50 μm displacement
- tilt = 0.1°, which is equal to about 100 μm displacement
- tilt = 0.2°, which is equal to about 200 μm displacement

Each case was simulated for two different beam initial energy values: 0 eV and 0.05 eV. The results of these simulations are presented in figures 6.9, 6.10, 6.11, 6.12 and 6.13. From these figures it can be seen that the grid tilting in this arrangement does not provoke significant changes in the electron density uniformity. Moreover, it is noticeable how for a beam initial energy equal to 0 eV the beam shows a square pattern, as per the pattern of the holes. The same behaviour does not hold for a beam initial energy higher than 0 eV, as the transverse energy of the electrons make them cover the grid walls space.

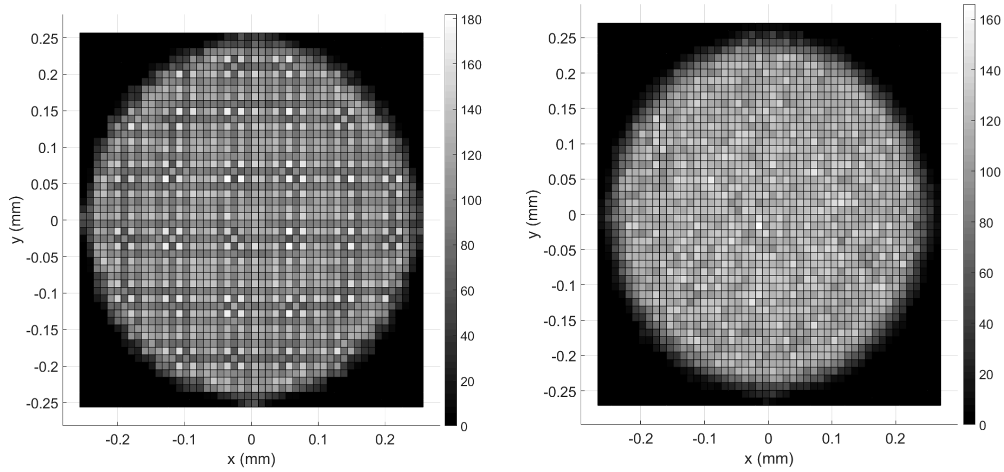

(a) Tilt = 0°, beam energy = 0 eV. (b) Tilt = 0°, beam energy = 0.05 eV.

Figure 6.9: Case 2. Beam spot in absence of grid tilting for different initial beam energies.

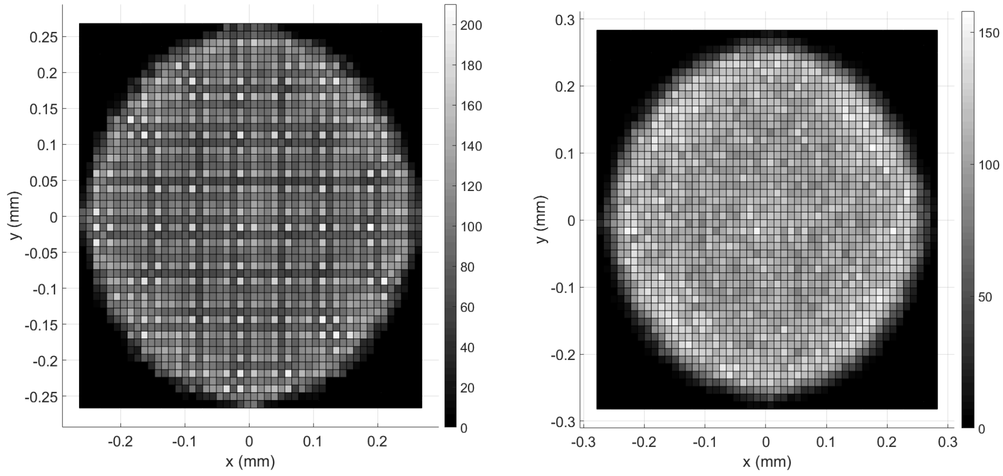

(a) Tilt = 0.02°, $E_i = 0$ eV. (b) Tilt = 0.02°, $E_i = 0.05$ eV.

Figure 6.10: Case 2. Effect of a 0.02° grid tilting for different initial beam energies.

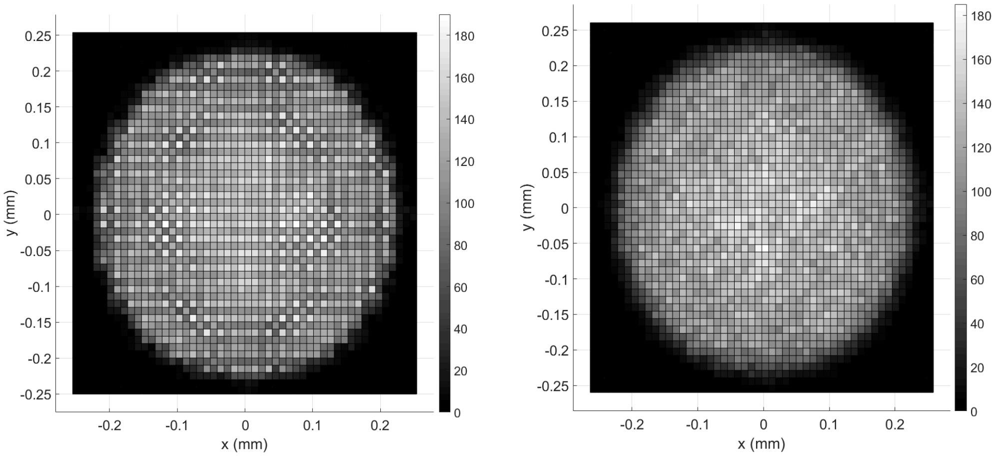

(a) Tilt = 0.05°, $E_i = 0$ eV.

(b) Tilt = 0.05°, $E_i = 0.05$ eV.

Figure 6.11: Case 2. Effect of a 0.05° grid tilting for different initial beam energies.

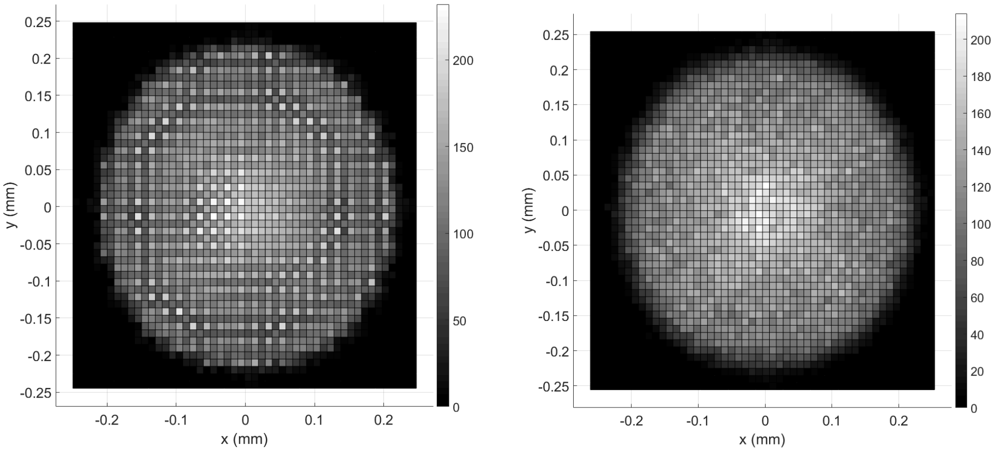

(a) Tilt = 0.1°, $E_i = 0$ eV.

(b) Tilt = 0.1°, $E_i = 0.05$ eV.

Figure 6.12: Case 2. Effect of a 0.1° grid tilting for different initial beam energies.

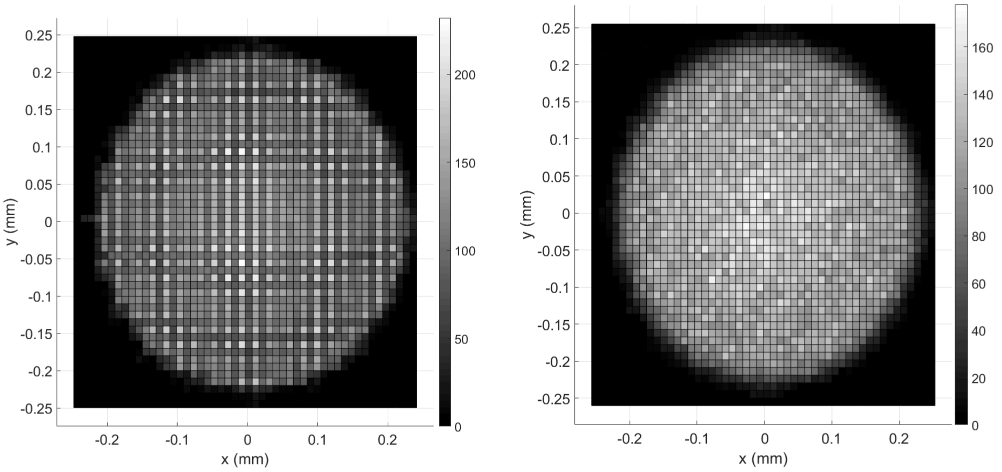

(a) Tilt = 0.2°, $E_i = 0$ eV. (b) Tilt = 0.2°, $E_i = 0.05$ eV.

Figure 6.13: Case 2. Effect of a 0.2° grid tilting for different initial beam energies.

The results presented for the case of a grid with additional frame, and the case of a one-component grid, show a remarkable difference regarding the electron density uniformity. Using a one-component grid provides results that are significantly more reliable at every tested tilting. This is due to a better uniformity of the field lines in the grid region when the electrode is a single piece and not divided into frame and grid. The two field lines distributions were shown in figure 6.3. The distribution of the field lines in figure 6.3b is visibly more uniform and this explains the better results obtained with this configuration.

These results led to the selection of a grid which is a stand-alone piece, and to discarding the option of a framed grid. The drawback is an increased fragility of the grid electrode, but the impact on the beam properties has greater importance.

6.3 Impact of the cathode layout

The impact of the cathode thickness and layout also needs consideration. In principle there are two main cases: the CNT array diameter is smaller than the spacer hole, e.g. the spacer between cathode and grid; the CNT array diameter is larger than the spacer hole. However, if the CNT array has a larger diameter than the spacer, when placing the spacer on the top of the cathode all CNTs that are not in the hole will be destroyed, with the CNT array assuming the size of the hole. This makes the two cases previously mentioned equivalent. At the same time, these scenarios expose an issue: the bending of the field lines at the edges of the CNT array due to the height of the CNTs. This effect was studied by simulating various CNT heights and observing the beam spot variations. The simulation layout is identical to the previous simulation with the only difference that the cathode diameter is now 0.2 mm and that the distance between the grid, which now is just a transparent layer, and the anode is set to 500 μm. These modifications have the purpose to decrease the simulation area and allow for finer meshing.

The CNT array heights investigated are: 0 μ, 1 μm, 5 μm and 50 μm. The case of 0 μm, while unrealistic, was added to have a comparison with the ideal case of no field distortions.

In figures 6.14, 6.15, 6.16, 6.17 the histograms calculated from the particle positions at the anode have been reported for comparison. The data analysis and visualization have been performed in the same way as for the grid tilting analysis. As it is possible to see from figures 6.14, 6.15, 6.16, 6.17, an increased cathode thickness results in a brighter beam in the central part and less bright at the tails. Furthermore, an increase in beam size is also noticeable. The case of 50 μm cathode thickness is quite disruptive for the beam if compared with the ideal case of 0 μm, with a beam much less bright and with bigger tails. The case of 1 μm does not seem to provoke significant altercations both in beam brightness and beam size.

The reason behind these effects is given by the field distortions at the cathode edges. When the cathode thickness is high the field distortions propagate for a larger area of the cathode, resulting in a less bright beam and a higher beam divergence. The case of 50 μm is reported in figure 6.18. As it is possible to notice from figure 6.18 the field distortions propagate along with the full size of the cathode. The cathode size used for this simulation is only 0.2 mm, thus for a larger cathode the field lines would eventually straighten, however for such cathode thickness this effect cannot be considered negligible. Moreover, this would enhance the edge effect described in chapter 3, effectively increasing the emission at the edges. The reason why this effect is not visible here is due to the spacer, where the outer part of the electron beam is dumped.

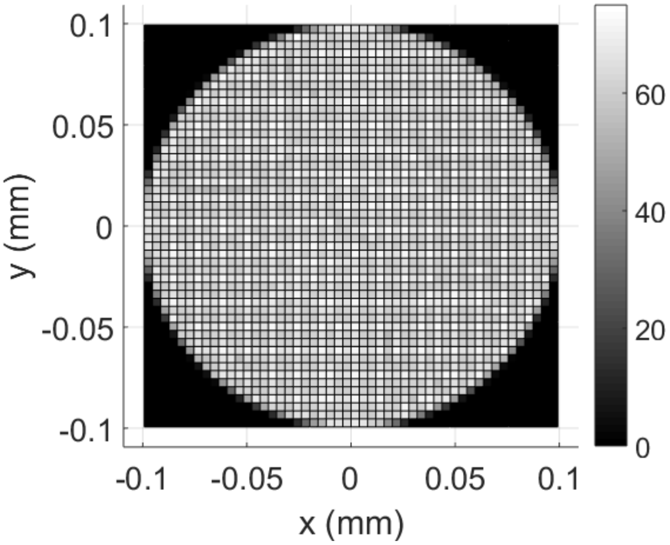

Figure 6.14: Effect of the cathode thickness on the beam spot. Cathode thickness: 0 μm.

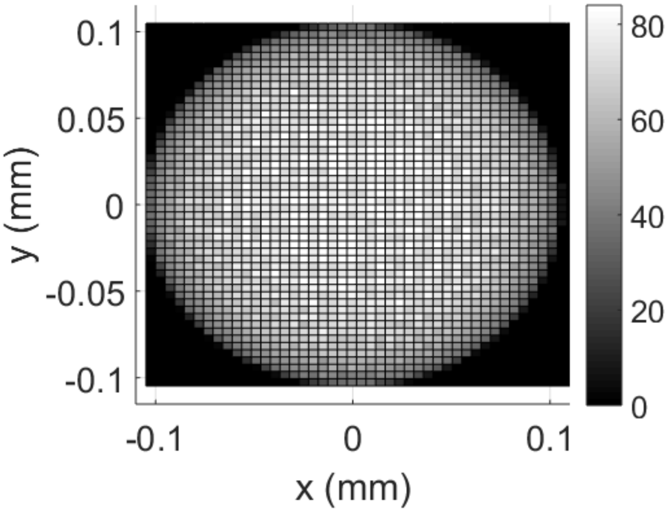

Figure 6.15: Effect of the cathode thickness on the beam spot. Cathode thickness: 1 μm.

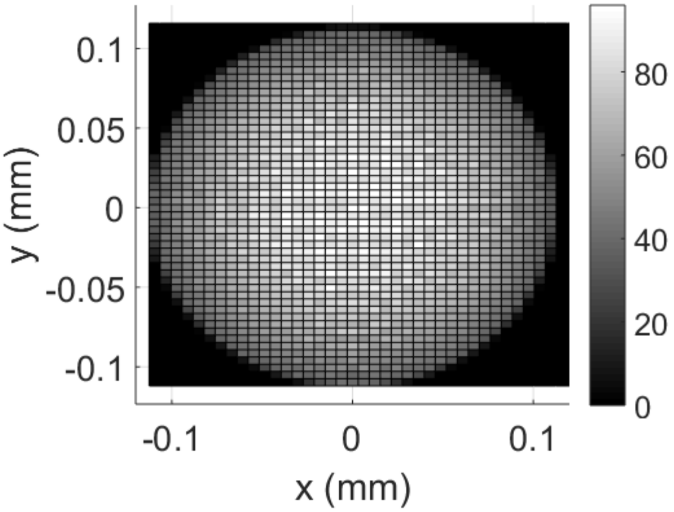

Figure 6.16: Effect of the cathode thickness on the beam spot. Cathode thickness: 5 μm.

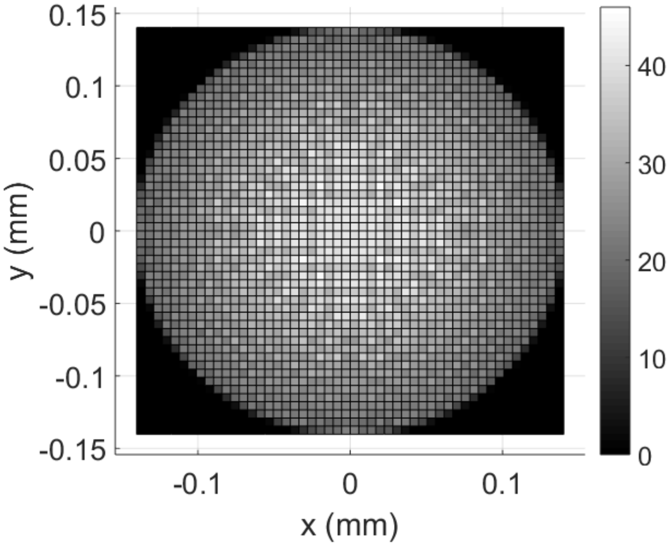

Figure 6.17: Effect of the cathode thickness on the beam spot. Cathode thickness: 50 μm.

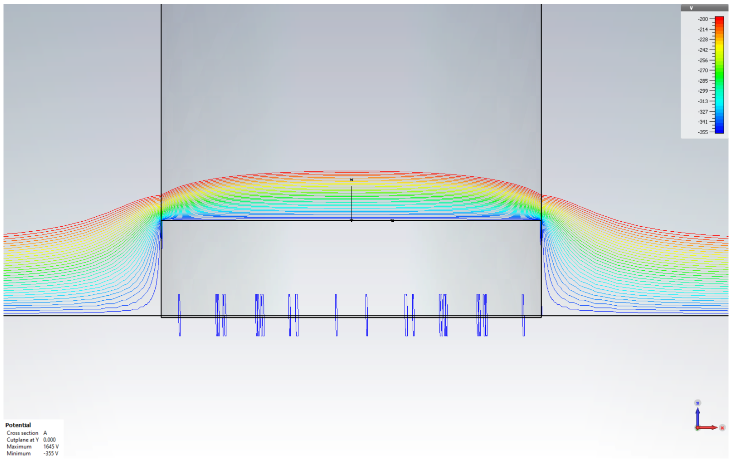

Figure 6.18: Field line distortions due to cathode thickness. Cathode thickness: 50 μm.

If the current output is taken into consideration this effect is well visible. In figure 6.19 the emitted current for every cathode thickness is reported. It is noticeable how the emitted current increases when the cathode thickness is higher. Although most of this current gain is lost into the spacer due to the high divergence of such electrons.

The field lines in the case of a cathode thickness of 1 μm are then reported in figure 6.20. In this case, it is noticeable how the field distortions are less evident and the field lines straighten much sooner, resulting in a brighter and more homogeneous beam. For a large area cathode the effect of such cathode thickness can be considered negligible.

This is also noticeable looking at the emitted current for these two cases. Figure 6.21 shows how when the cathode thickness is 1 μm, the current gain is quite limited and it is all lost into the spacer. After the grid the beam current for the two cases are equivalent.

The CNT array height can be tuned during growth, but values below 5 μm are usually not suggested in order to ensure vertically aligned tubes through thermal CVD [82]. In this thesis work, CNTs with height of 50 μm and grown using thermal CVD were used, and thus the choice of 50 μm as one of the simulation parameters.

For mitigating this issue, a possible solution can be the metalization of the spacer at the cathode side via the addition of a thick conductive layer. With the metal layer being of the same thickness as the CNT array; in this

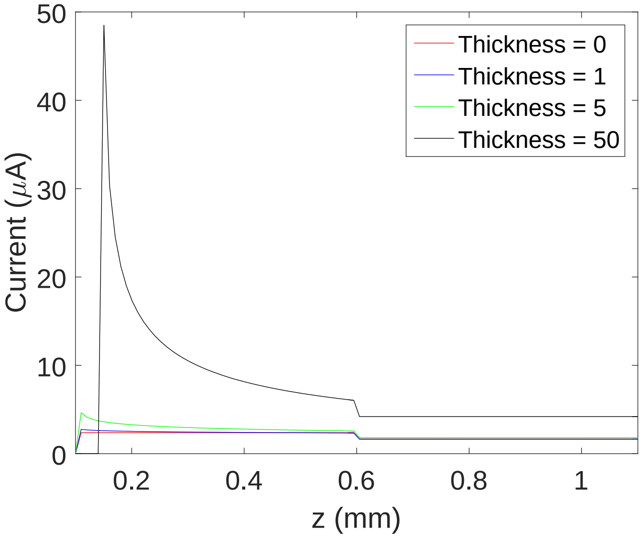

Figure 6.19: Emitted current for every cathode thickness.

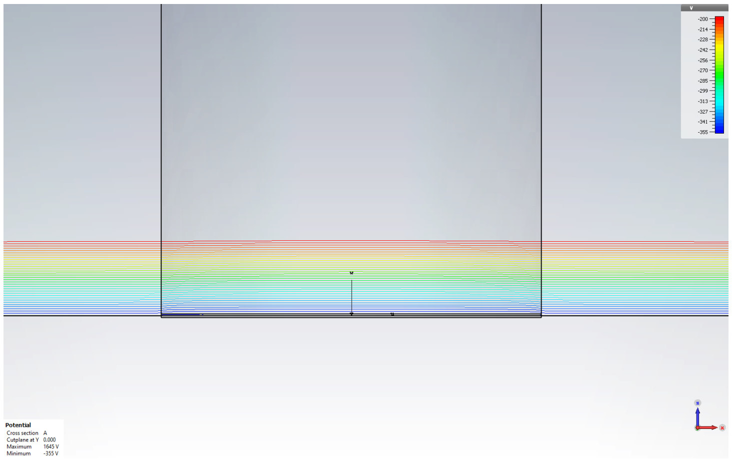

Potential
Cross section A
Cutplane at Y 0.000
Maximum 1645 V
Minimum -355 V

Figure 6.20: Field line distortions due to cathode thickness. Cathode thickness: 1 μm.

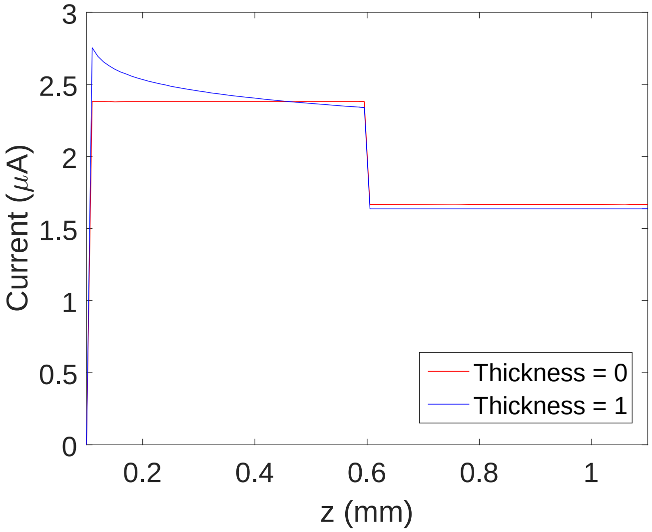

Figure 6.21: Emitted current for cathode thicknesses 0 and 1 μm.

case, 50 μm. The CNT height can usually be controlled within 1 μm, as per information acquired from suppliers, whilst the same height can, however, be measured with improved precision using SEM, e.g. sub-micron precision. The metalization thickness can also be controlled at a sub-micron precision according to suppliers' specifications. Therefore, the case of 1 μm previously studied can be considered valid, with the possibility of further improvement below 1 μm.

Alternatively, it is also possible to grow buried CNTs. This could avoid the use of metalization and also avoid current losses in the spacer as the spacer would no longer require to delimit the emission area.

6.4 Electrodes layout

The gun layout that was lastly designed is illustrated in figures 6.22 and 6.23. This design was made to allow for straight field lines in the whole emission and transport regions, whilst allowing enough space for mechanical fixings. From figure 6.22 it is possible to notice the main mechanical components which keep the gun together. The gun is mounted on a DN200 flange where 6 SHV connectors are welded. Of these 6 SHV, only 3 are needed, e.g.

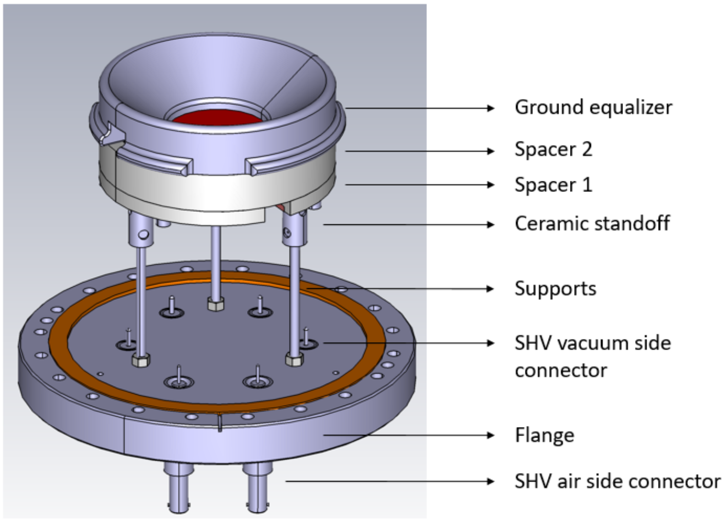

Figure 6.22: Illustration of the gun design.

cathode, grid 1, grid 2; the remaining 3 are spares. On the top of the flange, 3 metallic bars serve to sustain the gun. Between the bars and the gun, ceramic standoffs are placed to provide electrical insulation.

The gun is made of a CNT cathode on n-doped a Si substrate. A first ceramic spacer to separate the CNT cathode from grid 1, a second ceramic spacer, a second grid, and finally the so-called ground equalizer.

The gun is double gridded with two grids 15-3 type, as discussed in the previous sections of the chapter. The cathode-grid distance is set to 1.4 mm. This thickness ensures to have a virtually transparent grid, taking into account that the electric field may need to be increased if the current output decreases with time.

The distance between the first and second grid, thus the thickness of spacer 2, is set to 1 cm. This allows for straight field lines and permits to have some more space for the bolts to successfully keep all elements together.

The ground equalizer has the task to keep the voltage at 0 V after the second grid. Simulations have shown that the voltage applied on grid 1 can penetrate from the gun sides and affect the region after grid 2. The ground equalizer mitigates this issue.

To observe the flatness of the field lines it is helpful to divide the gun into three regions; between the cathode and grid 1, between grid 1 and grid 2, and after grid 2. Figure 6.24 shows the isolines plot for the first region

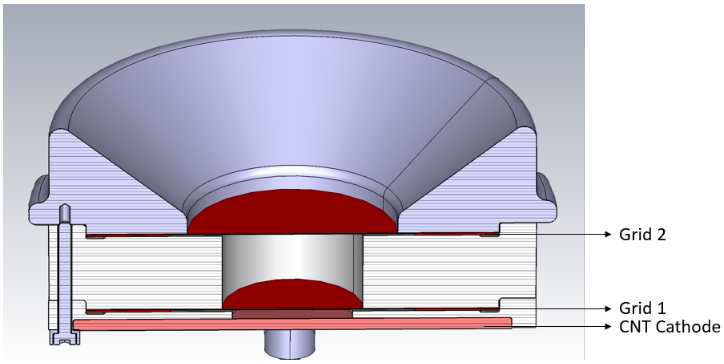

Figure 6.23: Illustration of the gun design: cut view.

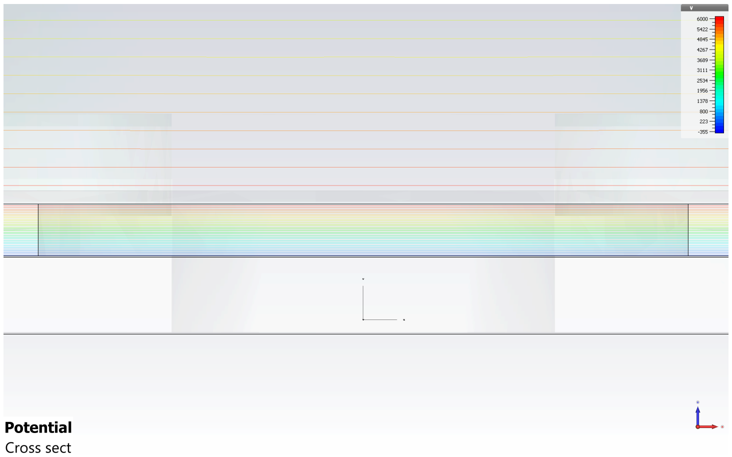

Figure 6.24: Isolines plot for the region between grid 1 and grid 2.

and perfectly straight lines in the whole emission region. The isolines plot for the second region is shown in figure 6.25. The isolines are in this case too perfectly straight. Finally, a contour plot for the third region is shown in figure 6.26. In this case, a contour plot was chosen as it can better represent an area where the potential is unvaried. The contour plot shows how the potential is successfully kept to 0 V with a precision better than 1 mV.

Due to straight field lines in all the regions of the gun and due to virtually transparent grids used, the beam should keep the properties set by the emission principle and the cathode properties. A minor tail effect is to be expected due to possible misalignment and cathode thickness mismatch as described in the previous sections.

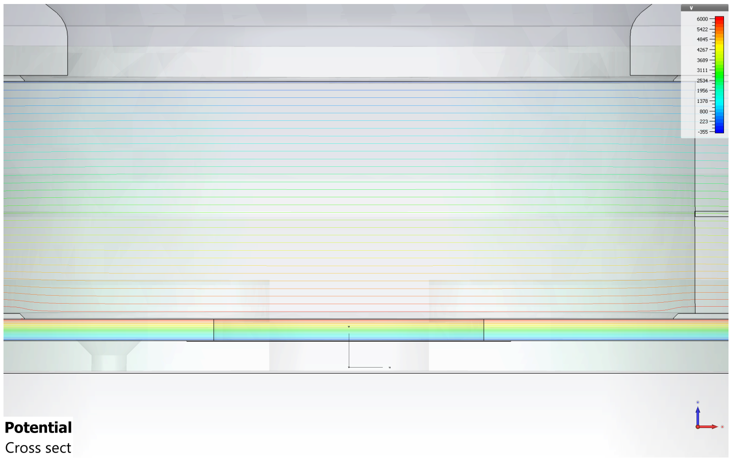

Figure 6.25: Isolines plot for the region between cathode and grid 1.

Figure 6.26: Contour plot for the region after grid 2.

A comprehensive simulation that would take into account a large area cathode, e.g. 2 cm of diameter, and two grids 15-3 type is unfortunately unfeasible because of the incredibly large number of mesh cells that it would require. Additionally, the modeling of a grid 15-3 type with an area larger than 2 mm proved to be unfeasible with the CAD tools at disposal.

Chapter 7

Conclusions

This PhD project aimed at assessing the performance limitations of a CNT-based cold electron gun. According to those, it sets the goal of providing a solid basis for the decision on whether a CNT-based cold electron gun can be a viable solution for the ELENA electron cooler.

The emission properties of CNTs were thus characterized. Namely: current stability, lifetime, and current switching capabilities. Furthermore, a vacuum surface characterization was performed to study some of the benefits of a conditioning process; in particular, the bake-out at high temperatures.

Several CNT samples were characterized, focusing on two main arrangement geometries. The samples tested have shown promising results if operated in optimal conditions, i.e. at a pressure P below 1×10^{-8} mbar and after a bake-out at a temperature T above 200 °C. Additionally, a conditioning process with voltage ramps was found necessary in order to achieve reproducible results. UHV and bake-out perfectly match the requirements of ELENA, where the nominal pressure is around 10^{-12} mbar and bake-out is part of the conditioning procedure.

One of the biggest concerns about CNTs pertains to their lifetime and stability. The tests performed indicated good stability and the lifetime is promising for the so-called CNT1 arrays with honeycomb-like geometry. Namely, for the array most thoroughly tested, emission for more than 1500 hours at different electric fields was proved, without signs of burnout or degradation.

The use of a large area cathode would most likely be beneficial for optimizing the performance for operational use as it would permit the use of a lower applied electric field. Nonetheless, the current stability proved to be unaffected when increasing the current emission from a few hundred μA/cm^2

to a few mA/cm^2, with current fluctuations within 1 % of the nominal emitted current.

Regarding the maximum reachable current, all samples showed that they can reach current densities as high as 2 mA/cm^2, which would already suffice for the electron gun of the ELENA cooler. Moreover, CNTs can reportedly emit much larger currents.

Finally, having a large number of CNTs and small channels improved stability and lifetime. This explains why the honeycomb-like arrays exhibited the best performance. A hexagonal pattern leads to a large number of CNTs emitting simultaneously, as it allows for the best space optimization, thus maximizing the number of emitters. A reason for the poorer performance of the square-islands array may derive from this feature since in this case, the total number of CNTs is much smaller compared to a honeycomb-like array of equal chip size.

Studies of the emission from CNTs operated in current switching mode have also shown how fast current switching is possible with unaltered emitting properties. Rise and fall times below 600 ns were proved at different switching frequencies. A limitation was in this case represented by the diode configuration used for the experiments, as it included a capacitance effect during fast switching. This made it impossible to study the rise and fall times at a higher speed.

This part concludes the set of experiments devoted to characterizing the current emission performance of CNTs as electron field emitters.

The second part included a simulation study of the impact of the extracting grids on the beam properties. Such simulation study addressed several extracting grids with progressively smaller holes and it was devised to assess the feasibility of using such grids.

Within this simulation study, it was possible to address what most likely are the parameters that affect the electron beam the most, namely:

- cathode-grid distance
- grid thickness
- beam initial energy
- applied electric field

Investigating the effect of such parameters it was possible to derive the main beam properties of interest: the grid transparency, and the beam total transverse energy after the beam passes through the grid. The study of several grids led to choosing a grid with holes no larger than 25 μm and a bar width of 5μm as the first optimal candidate considering ELENA's requirements. Namely, a beam transverse energy smaller than 0.1 eV. This is the minimum transverse energy of the electron beam currently generated in the ELENA electron cooler using a thermionic cathode. It must also be pointed out that for the thermionic gun case the 0.1 eV is the minimal transverse energy value relative to the core of the beam, while the tails would show a much higher transverse energy. Contrarily, due to our simulation and calculation methods, the transverse energy values reported are relative to the maximum transverse energy of the electrons composing the beam.

The grid transparency was also evaluated as it affects the required emitted current. Low grid transparency implies that the emitted current must be increased; and to increase the emitted current, the applied electric field must be consequently increased. As a consequence, the beam transverse energy would increase as well. From such considerations, it is clear how all parameters are interconnected and must therefore be accounted for in detail to fully assess the grid effect on the beam properties.

This simulation study led to an industry research aimed at assessing the smaller hole size which is possible to reach with the current state-of-the-art technology. The research has led to finding a supplier able to further down-scale the grid to a hole size of 15 μm and bar width of 3 μm. Further simulations on this grid type have shown that such a grid does not significantly affect the beam transverse energy. This results in an electron beam whose properties are almost fully dependent on the emission process.

Finally, a possible gun design was proposed. This took into account a further set of simulations aimed at mitigating some of the main sources of beam energy growth and beam homogeneity. These simulations addressed: the grid tilting, resulting in the choice of a one-component n-doped Si grid; and the cathode thickness and relative edge effects, resulting in the possible solution of the metalization of the ceramic spacer with thickness as close as possible to the CNT height.

These expedients permit to have a beam that only presents a minor tail effect at the very end of its diameter, while the majority of the beam presents unaltered properties after the emission.

To conclude, it has been shown that CNTs can stably emit for more than 1500 hours, which wasn't prior proved. The measurements were done in conditions - such as base pressure, bake-out, and emitted current - which are compatible with the ELENA electron cooler. Thus proving that their use is compatible with ELENA and most accelerator facilities.

In the same way, the fast current switching has been proved with results that significantly outperform the current electron gun used in ELENA. Furthermore, these experiments have shown the potential of CNTs in applications where fast pulsing is strictly required.

The results obtained within this PhD thesis are thus valid for many fields and areas. The case of ELENA is only one of the possible use cases.

The results concerning the emission performance of CNT-based cathodes are spendable in every area where a field emission cathode can be used and set the base for the use of CNT-based cathodes in operation.

The investigation of extracting grids has an even wider reach. Such results are not only valid for the case of a CNT-based cathode, but can be extended to any case where an extracting grid is deemed necessary. While grids pose constraints such as beam losses due to hitting the grid's solid bars, they also provide unbeatable field homogeneity, especially for large emission areas.

To date and my knowledge, there is not a similar simulation or experimental study on extracting grids in literature. This study thus sets a solid basis for the use of extracting grids in low-energy electron guns and beyond.

Finally, the double-gridded gun design proposed, while still at a prototype stage, is also valid for any use case, with the CNT case being only one of the possible options. The double grid setup permits to have control of the beam kinetic energy changing the voltage on the cathode only, independently of the field required for achieving the desired current output. This makes it a possible choice for thermionic cathodes and photo-cathodes too.

Undoubtedly, more tests are needed before using a CNT-based electron gun in ELENA. An open question is the impact of the field distortion at the CNT tip on the beam energy width.

This PhD thesis sets the basis for the use of CNT-based cathodes in long-lasting operation. It further proves how extracting grids can be a viable solution for electron guns, and how a grid does not significantly perturb the beam. Finally, the proposed gun design and the study on sources of beam distortion show how the measurement of the intrinsic beam properties can be highly affected by the conditions of the experiments. This can set the basis for future precision studies of the CNT intrinsic emission properties.

List of Figures

List of Tables

Bibliography

[1] `https://home.cern/`. 25-02-2023.

[2] H. Damerau et al. *LHC Injectors Upgrade, Technical Design Report.* 2014. DOI: `10.17181/CERN.7NHR.6HGC`.

[3] M. Hori and J. Walz. “Physics at CERN’s Antiproton Decelerator”. In: *Progress in Particle and Nuclear Physics* 72 (2013), pp. 206–253.

[4] S .Maury, W. Oelert, W. Bartmann, P. Belochitskii, H. Breuker, F. Butin, C. Carli, T. Eriksson, S. Pasinelli, and G. Tranquille. “ELENA: the extra low energy anti-proton facility at CERN”. In: *Hyperfine Interact* 29 (2014), pp. 105–115.

[5] W. Oelert. “The ELENA project at CERN”. In: *Proceedings of IPAC2016* 48 (2017).

[6] G. Tranquille, A. Frassier, and L. Joergensen. “The ELENA electron cooler: Parameter choice and expected performance.” In: *Proceedings of COOL2013* WEPPO16 (2013), pp. 113–115.

[7] Helmut Poth. “Electron cooling: theory, experiment, application”. In: *CERN-EP/90-04* (1990).

[8] I. N. Meshkov. “Electron cooling: status and perspectives”. In: *CERN* (1994).

[9] YA. S. Derbenev and A. N. Skrinsky. “The kinetics of electron cooling of beams in heavy particles storage rings”. In: *Particle Accelerators* 8 (1976), pp. 1–20.

[10] V. V. Parkhomchuk and A. N. Skrinsky. “Electron cooling: 35 years of development”. In: *Physics - Uspekhi* 43.5 (2000), pp. 433–452.

[11] G. I. Budker, N. S. Dikansky, V. I. Kudelainen, I. N. Meshkov, V. V. Parchomchuk, D. V. Pestrikov, A. N. Skrinsky, and B. N. Sukhina. "Experimental studies of electron cooling". In: *Particle Accelerators* 7 (1976), pp. 197–211.

[12] YA. S. Derbenev and A. N. Skrinsky. "The effect of an accompanying magnetic field on electron cooling". In: *Particle Accelerators* 8 (1977), pp. 235–243.

[13] A. H. Sorensen and E. Bonderup. "Electron cooling". In: *Nuclear Instruments and Methods* 215 (1982), pp. 27–54.

[14] G. Tranquille and J. Cenede. "Design and Optimization of the ELENA electron cooler gun and collector". In: *Proceedings of IPAC2016* (2016).

[15] T. Shirai et al. "S-LSR, Cooler ting development at Kyoto University". In: *Proceedings of COOL05* (2005).

[16] `http://www.tesla.co.uk/`. 25-02-2023.

[17] R. Warner. "Electromagnetic Analysis of the ELENA Magnet System". In: *Tesla Engineering internal report* ().

[18] S. Pastuszka, U. Schramm, M. Grieser, C. Broude, R. Grimm, D. Habs, J. Kenntner, H. Miesner, T. Schubler, D. Schwalm, and A. Wolf. "Electron cooling and recombination experiments with an adiabatically expanded electron beam". In: *Nuclear Instruments and Methods in Physics Research A* 369 (1996), pp. 11–22.

[19] H. Danared, A. Kallberg, G. Andler, L. Bagge, F. Osterdahl, A. Paal, K. Rensfelt, A. Simonsson, O. Skeppstedt, and M. Ugglas. "Studies of electron cooling with a highly expanded electron beam". In: *Nuclear Instruments and Method in Physics Research A* 441 (2000), pp. 123–133.

[20] Yahachi Saito. *Carbon nanotube and related field emitters.* Wiley-VCH, 2010.

[21] B. Galante, G. A. Tranquille, M. Himmerlich, C. P. Welsch, and J. Resta López. "Stability and lifetime study of carbon nanotubes as cold electron field emitters for electron cooling in the CERN extra low energy antiproton ring". In: *Phys. Rev. Accel. Beams* 24.113401 (2021). DOI: `10.1103/PhysRevAccelBeams.24.113401`.

[22] B. Galante, G. A. Tranquille, C. P. Welsch, O. Apsimon, and J. Resta López. “Carbon nanotubes as cold electron field emitters for electron cooling in the CERN Extra Low ENergy Antiproton (ELENA) ring”. In: *Proceedings of IPAC21* (2021).

[23] J. I. Sohn, S. Lee, Y.-H. Song, S.-Y. Choi, K.-I. Cho, and K.-S. Nam. “Patterned selective growth of carbon nanotubes and large field emission from vertically well-aligned carbon nanotube field emitter arrays”. In: *Applied Physics Letters* 78.7 (2000).

[24] C. Li, Y. Zhang, M. Mann, D. Hasko, W. Lei, B. Wang, D. Chu, D. Pribat, G. Amaratunga, and W. I. Milne. “High emission current density, vertically aligned carbon nanotube mesh, field emitter array”. In: *Appl. Phys. Lett.* 97.113107 (2010).

[25] J. Sohn, S. Lee, Y.-H. Song, S.-Y. Choi, and K.-S. Nam. “Patterned selective growth of carbon nanotubes and large field emission from vertically well-aligned carbon nanotube field emitter arrays”. In: *Appl. Phys. Lett.* 78.7 (2001).

[26] A. Nojeh. “Carbon nanotube electron sources: from electron beams to energy conversion and optophotonics”. In: *ISRN Nanomaterials* 2014.879827 (2014).

[27] X. Gu et al. “Stable operation of a high-voltage high-current dc photoemission gun for the bunched beam electron cooler in RHIC”. In: *Physical Review Accelerators and Beams* 23.013401 (2020).

[28] C. J. Liaw et al. “Cathode puck insertion system design for the LEREC photoemission dc electron gun”. In: *NAPAC2016* BNL-112352-2016-CP (2016).

[29] R. H. Fowler and L. Nordheim. “Electron emission in intense electric fields”. In: *Proceeding of the royal society A - Mathematical, physical and engineering sciences* CXIX.-A (1928).

[30] A. V. Eletskii. “Carbon nanotube-based electron field emitters”. In: *Phyics-Uspeki - Review of topical problems* 53 (2010), pp. 863–892.

[31] F. Giubileo, A. Di Bartolomeo, L. Iemmo, G. Luongo, and F. Urban. “Field Emission from Carbon Nanostructures”. In: *Appl. Sci.* 8.526 (2018).

[32] L. Nordheim. “Zur Theorie der thermischen Emission und der Reflexion yon Elektronen an Metallen.” In: *Z. f. Physik* 46.833 (1928).

[33] E. L. Murphy and R. H. Good. “Thermionic emission, field emission, and the transition region”. In: *Physical Review* 102.6 (1956).

[34] L. Nordheim. “The effect of the image force on the emission and reflection of electrons by metals.” In: *Proc. R. Soc. Lond. A* 121 (1928), pp. 626–639.

[35] R. E. Burgess, H. Kroemer, and J. M. Houston. “Corrected values of Fowler-Nordheim field emission functions v(y) and s(y).” In: *Phys. Rev.* 90 (1953), p. 515.

[36] R. G. Forbes. “The Murphy–Good plot: a better method of analysing field emission data”. In: *R. Soc. open sci.* 6.190912 (2019).

[37] R. G. Forbes. “Comments on the continuing widespread and unnecessary use of a defective emission equation in field emission related literature.” In: *J. Appl. Physics* 126 (2019).

[38] J. G. Simmons. “Richardson-Schottky effect in Solids”. In: *Physical Review Letters* 15-25 (1965), pp. 967–968.

[39] M. Dionne, S. Coulombe, and J.-L. Meunier. “Field emission calculations revisited with Murphy and Good theory: a new interpretation of Fowler-Nordheim plot”. In: *J. Phys. D: Appl. Phys.* 41.245304 (2008).

[40] C. Germain and F. Rohrbach. “High voltage breakdown in vacuum.” In: *Vacuum* 18 (7 1968), pp. 371–377.

[41] P. Yaghoobi, K. Walus, and A. Nojeh. “First-principles study of quantum tunneling from nanostructures: current in a single-walled carbon nanotube electron source”. In: *Physical Review B* 80.115422 (2009).

[42] S. Han and J. Ihm. “First-principles study of field emission of carbon nanotubes”. In: *Physical Review B* 66.241402 (2002).

[43] S. Han, M. H. Lee, and J. Ihm. “Dynamical simulation of field emission in nanostructures”. In: *Physical Review B* 65.085405 (2002).

[44] H.-S. Ahn, K.-R. Lee, D.-Y. Kim, and S. Han. “Field emission of doped carbon nanotubes”. In: *Applied Physics Letters* 88.093122 (2006).

[45] N. Park, S. Han, and J. Ihm. “Effects of oxygen adsorption on carbon nanotube field emitters”. In: *Physical Review B* 64.125401 (2001).

[46] A. Mayer, N. M. Miskovsky, P. H. Cutler, and Ph. Lambin. “Transfer-matrix simulations of field emission from bundles of open and closed (5, 5) carbon nanotubes”. In: *Physical Review B* 68.235401 (2003).

[47] A. Mayer, N. M. Miskovsky, and P. H. Cutler. “Theoretical comparison between field emission from single-wall and multi-wall carbon nanotubes”. In: *Physical Review B* 65.155420 (2003).

[48] M. F. L. De Volder, S. H. Tawfick, R. h¿ Baughman, and A. J. Hart. “Carbon nanotubes: Present and future commercial applications”. In: *Science* 339 (2013), p. 535.

[49] N. Gupta, S.M. Gupta, and S.K. Sharma. “Carbon nanotubes: synthesis, properties and engineering applications”. In: *Carbon Lett.* 29 (2019), pp. 419–447.

[50] S. Rathinavel, K. Priyadharshini, and Dhananjaya Panda. “A review on carbon nanotube: An overview of synthesis, properties, functionalization, characterization, and the application”. In: *Materials Science and Engineering: B* 268.115095 (2021).

[51] S. Iijima. “Helical microtubules of graphitic carbon”. In: *Nature* 354 (1991).

[52] S. Iijima. “Carbon nanotubes: past, present, and future”. In: *Physica B* 323 (2002), pp. 1–5.

[53] T. W. Ebbesen. “Carbon nanotubes”. In: *Annu. Rev. Mater. Sci.* 24 (1994), p. 235.

[54] A. V. Eletskii. “Carbon nanotubes”. In: *Physics-Uspekhi* 40.9 (1997).

[55] V. N. Popov. “Carbon nanotubes: properties and application”. In: *Materials Science and Engineering R* 43 (2003), pp. 61–102.

[56] H. Dai. “Carbon nanotubes: opportunities and challenges”. In: *Surface Science* 500 (2002), pp. 218–241.

[57] S. Iijima and T. Ichihashi. “Single-shell carbon nanotubes of 1-nm diameter”. In: *Nature* 363 (1993), p. 603.

[58] N. Dwivedi et al. “The rise of carbon materials for field emission”. In: *J. Mater. Chem. C* 9.2620 (2021).

[59] M. Krystof. “Field-emission electron gun for a MEMS electron microscope”. In: *Microsystems & Nanoengineering* 7.43 (2021).

[60] J. Zhang, J. Xu, D. Ji, H. Xu, M. Sun, L. Wu, X. Li, Q. Wang, and X. Zhang. “Development of an electron gun based on CNT-cathode for traveling wave tube application”. In: *Vacuum* 186.110029 (2021).

[61] V. Chouhan, T. Noguchi, and S. Kato. “Field emission from optimized structure of carbon nanotube field emitter array”. In: *Journal of Applied Physics* 119.134303 (2016).

[62] M.R. Kurilich, A. Thapa, A. Moilanen, J.L. Miller, W. Li, and S. Neupane. “Comparative study of electron field emission from randomly-oriented and vertically-aligned carbon nanotubes synthesized on stainless steel substrates”. In: *J. Vac. Sci. Technol. B* 37.4 (2019).

[63] M. S. Dresselhaus, G. Dresselhaus, and R. Saito. “Physics of carbon nanotubes”. In: *Carbon* 33.7 (1995), pp. 883–891.

[64] N. Saifuddin, A. Z. Raziah, and A. R. Junizah. “Physics of carbon nanotubes”. In: *Journal of Chemistry* 2013.676815 (2013).

[65] J.B. Bai and A. Allaoui. “Effect of the length and the aggregate size of MWNTs on the improvement efficiency of the mechanical and electrical properties of nanocomposites—experimental investigation”. In: *Composites Part A: Applied Science and Manufacturing* 34 (8 2003), pp. 689–694.

[66] G. Rahman, Z. Najaf, A. Mehmood, S. Bilal, A. H. A. Shah, S. A. Mian, and G. Ali. “An overview of the recent progress in the synthesis and applications of carbon nanotubes”. In: *Journal of Carbon Research* 5.3 (2019).

[67] J.-M. Bonard, J.-P. Salvetat, T. Ctockli, L. Forro, and A. Chatelain. “Field emission from carbon nanotubes: perspectives for applications and clues to the emission mechanism”. In: *Appl. Phys. A* 69 (1999), pp. 245–254.

[68] J.-M. Bonard, M. Croci, C. Klinke, R. Kurt, O. Noury, and N. Weiss. “Carbon nanotubes films as electron field emitters”. In: *Carbon* 40 (2002), pp. 1715–1728.

[69] R. C. Smith and S. R. P. Silva. “Maximizing the electron field emission performance of carbon nanotube arrays.” In: *Appl. Phys. Lett.* 94.133104 (2009).

[70] Y. M. Wong, W. P. Kang, J. L. Davidson, B. K. Choi, W. Hofmeister, and J. H. Huang. “Array geometry, size and spacing effects on field emission characteristics of aligned carbon nanotubes”. In: *Diamond and Related Materials* 14.2017-2083 (2005).

[71] H. Todokoro, N. Saitou, and S. Yamamoto. “Role of ion bombardment in field emission current instability”. In: *Japanese Journal of Applied Physics* 21 (1982), pp. 1513–1516.

[72] C. Kim, Y. S. Choi, S. M. Lee, J. T. Park, B. Kim, and Y. H. Lee. “The effect of Gas adsorption on the field emission mechanism of carbon nanotubes”. In: *J.AM.CHEM.SOC.* 124 (2002), pp. 9906–9911.

[73] J. I. Sohn and S. Lee. “Patterned selective growth of carbon nanotubes and large field emission from vertically well-aligned carbon nanotube field emitter arrays”. In: *Appl. Phys. Lett.* 78 (2001), p. 901.

[74] P. Vincent, S. T. Purcell, C. Journet, and V. T. Binh. “Modelization of resistive heating of carbon nanotubes during field emission”. In: *Physical Review B* 66.075406 (2002).

[75] S. T. Purcell, P. Vincent, and V. T. Binh. “Hot Nanotubes: Stable Heating of Individual Multiwall Carbon Nanotubes to 2000 K Induced by the Field-Emission Current”. In: *Phys. Rev. Lett.* 80.105502 (2002).

[76] Jun-Tae Kang Y.C. Choi, S. Park, E. Go, H. Jeon, J.-W. Kim, J.-W. Jeong, K.-H. Park, and Y.-H. Song. “High performance field emission and Nottingham effect observed from carbon nanotube yarn”. In: *Physica E: Low-dimensional Systems and Nanostructures* 86 (2017), pp. 52–57.

[77] `https://iseg-hv.com/en/products/detail/HPS`. 25-02-2023.

[78] `https://cdn.rohde-schwarz.com/pws/dl_downloads/dl_common_library/dl_manuals/gb_1/h/hm8012_1/HM8012_Digit_Multimeter_UserManual_de_en_03.pdf`. 25-02-2023.

[79] `https://www.ni.com/pdf/manuals/320999e.pdf`. 25-02-2023.

[80] `https://www.pfeiffer-vacuum.com/en/products/measurement-analysis/measurement/activeline/activeline-gauges/16099/pirani-cold-cathode-gauge-pkr`. 25-02-2023.

[81] `https://www.edwardsvacuum.com/en/our-products/turbomolecular-pumping-stations`. 25-02-2023.

[82] `https://www.nano-lab.com`. 25-02-2023.

[83] L. Sun, G. Yuan, L. Gao, J. Yang, M. Chhowalla, M. H. Gharahcheshmeh, K. K. Gleason, Y. S. Choi, B. H. Hong, and Z. Liu. “Chemical vapour deposition”. In: *Nature Reviews - Methods Primers* 1.5 (2021).

[84] `https://www.zeiss.com/microscopy/en/products/sem-fib-sem/fib-sem/crossbeam.html`. 25-02-2023.

[85] A. Mohammed and A. Abdullah. “Scanning electron microscopy (SEM): a review”. In: *Proceeding of 2018 International Conference on Hydraulic and Pneumatics* ISSN 1454 - 8003 (2018).

[86] `https://www.zeiss.com/microscopy/en/products/sem-fib-sem/sem.html`. 25-02-2023.

[87] V. Baglin, J. Bojko, O. Grobner, B. Henrist, N. Hilleret, C. Scheuerlein, and M. Taborelli. “The secondary electron yield of technical materials and its variation with surface treatments”. In: *Proceeding of EPAC 2000* (2000).

[88] K. Ozawa. “Ultraviolet Photoelectron Spectroscopy”. In: *The Surface Science Society of Japan (eds) Compendium of surface and interface analysis* Springer, Singapore (2018).

[89] J. F. Moulder, W. F. Stickle, P. E. Sobol, and K. D. Bomben. *Handbook of X-Ray Photoelectron Spectroscopy*. Perkin-Elmer Corporation, 1992.

[90] `https://www.vacuumscienceworld.com/blog/residual-gas-analysers-explained`. 25-02-2023.

[91] `https://www.specs-group.com/`. 25-02-2023.

[92] `https://www.specs-group.com/nc/specs/productseries/detail/phoibos-150/`. 25-02-2023.

[93] `https://www.kimballphysics.com/product/elg-2-egps-1022/`. 25-02-2023.

[94] V. Petit, M. Taborelli, H. Neupert, P. Chiggiato, and M. Belhaj. “Role of the different chemical components in the conditioning process of air exposed copper surfaces”. In: *Phys. Rev. Accel. Beams* 22 (8 2019), p. 083101. DOI: `10.1103/PhysRevAccelBeams.22.083101`. URL: `https://link.aps.org/doi/10.1103/PhysRevAccelBeams.22.083101`.

[95] `https://www.behlke.com/`. 25-02-2023.

[96] `https://www.behlke.com/pdf/general.pdf`. 25-02-2023.

[97] `https://cdn.rohde-schwarz.com/pws/dl_downloads/dl_common_library/dl_brochures_and_datasheets/pdf_1/RTO_bro_en_5214-2327-12_v2201.pdf`. 25-02-2023.

[98] `https://www.keysight.com/ch/de/product/33220A/function--arbitrary-waveform-generator-20-mhz.html`. 25-02-2023.

[99] `https://www.delta-elektronika.nl/en/products/dc-power-supplies-300w-es300-series.html`. 25-02-2023.

[100] B. Everitt. *The Cambridge Dictionary of Statistics*. Cambridge University Press, 1998.

[101] A. Kumar, S. Parveen, S. Husain, M. Zulfequar, Harsh, and M. Husain. “Oxygen and nitrogen doping in single wall carbon nanotubes: an efficient stable field emitter”. In: *Journal of Alloys and Compounds* 711 (2017), pp. 85–93.

[102] H. Ago, W. R. Salaneck T. Kugler F. Cacialli, M. S. P. Shaffer, A. H. Windle, and R. H. Friend. “Work functions and surface functional groups of multiwall carbon nanotubes”. In: *J. Phys. Chem. B* 103 (1999), pp. 8116–8121.

[103] P. Liu, Q. Sun, F. Zhu, K. Liu, K. Jiang, L. Liu, Q. Li, and S. Fan. “Measuring the Work Function of Carbon Nanotubes with Thermionic Method”. In: *Nano Letters* 8 (2008), pp. 647–651.

[104] M. Shiraishi and M. Ata. “Work function of carbon nanotubes”. In: *Carbon* 39 (2001), pp. 1913–1917.

[105] G. Rovida, F. Pratesi, M. Maglietta, and E. Ferroni. “Chemisorption of oxygen on the silver (111) surface”. In: *Surface Science* 43.1 (1974), pp. 230–256. ISSN: 0039-6028. DOI: `https://doi.org/10.1016/0039-6028(74)90229-5`.

[106] R. Cimino, L. A. Gonzalez, R. Larciprete, A. Di Gaspare, G. Iadarola, and G. Rumolo. “Detailed investigation of the low energy secondary electron yield of technical Cu and its relevance for the LHC”. In: *Phys. Rev. ST Accel. Beams* 18 (5 2015), p. 051002. DOI: `10.1103/PhysRevSTAB.18.051002`.

[107] Hiroyuki Kawano. “Effective work functions for ionic and electronic emissions from mono- and polycrystalline surfaces”. In: *Progress in Surface Science* 83.1 (2008), pp. 1–165. ISSN: 0079-6816. DOI: `https://doi.org/10.1016/j.progsurf.2007.11.001`.

[108] Q. Chen et al. “Development of a High-Beam-Transparency Gridded Electron Gun Based on a Carbon Nanotube Cold Cathode”. In: *IEEE Electron Device Letters* 43.4 (2022), pp. 615–618.

[109] S. Suemine et al. “Grid pulser for an electron gun with a thermionic cathode for the high-power operation of a terahertz free-electron laser”. In: *Nuclear Instruments and Method in Physics Research A* 773 (2015), pp. 97–103.

[110] X. Li, B. Chen, Y. Feng, Y. Zhang, S. Deng, and J. Feng. “Beam Test of a Novel CNT Cathode-Based Electron Gun Assembled in a TWT”. In: *IEEE Transactions on Electron Devices* 66.5 (2019), pp. 2382–2388.

[111] J. -T. Kang et al. “Fast and Stable Operation of Carbon Nanotube Field-Emission X-Ray Tubes Achieved Using an Advanced Active-Current Control”. In: *IEEE Electron Device Letters* 36.11 (2015), pp. 1209–1211.

[112] A.P. Gupta, S. Park, S.J. Yeo, J. Jung, C. Cho, S.H. Paik, H. Park, Y.C. Cho, S.H. Kim, J.H. Shin, J.S. Ahn, and J. Ryu. “Direct Synthesis of Carbon Nanotube Field Emitters on Metal Substrate for Open-Type X-ray Source in Medical Imaging”. In: *Materials* 10.878 (2017).

[113] N. N. Dzbanovskii, P. V. Minakov, A. A. Pilevskii, A. T. Rakhimov, B. V. Seleznev, N. V. Suetin, and A. Yu. Yur’ev. “High-current electron gun with a field emission cathode and diamond grid”. In: *Surface, Electron and Ion Emission* 75.10 (2005), pp. 111–114.

[114] Z. Yang et al. “Experimental proof test of CW mode RF modulated grid-controlled thermionic electron gun”. In: *Nuclear Instruments and Method in Physics Research A* 1021.165958 (2022).

[115] Y. Yamazaki and M. Nomura. “Development of the electron gun for the JNC high power LINAC”. In: *Proceedings of the XX International Linac Conference* (2000).

[116] I. S. Lehrman et al. “Design of a high-brightness, high-duty factor photocathode electron gun”. In: *Nuclear Instruments and Method in Physics Research A* 318 (1992), pp. 247–253.

[117] A. Eisenstein. “A grid controlled x-ray tube”. In: *Review of Scientific Instruments* 13.208 (1942).

[118] J. Li, Y. Ke, B. Li, and S. Deng. “A cold cathode electron gun using convex carbon nanotube emitter”. In: *IEEE Transactions on Electron Devices* 69.3 (2022), pp. 1457–1460.

[119] Y. Guo et al. “Achieving high current stability of gated carbon nanotube cold electron source using IGBT modulation for X-ray source application”. In: *Nanomaterials* 12.11 (2022).

[120] `https://www.3ds.com/products-services/simulia/products/cst-studio-suite/`. 25-02-2023.

[121] `https://www.autodesk.com/products/inventor/overview?term=1-YEAR&tab=subscription`. 25-02-2023.

[122] M.-C. Lin. “Space charge effects on the characteristics of field emission arrays.” In: *Journal of Vacuum Science & Technology B: Microelectronics and Nanometer Structures Processing, Measurement, and Phenomena* 25.493 (2007).

[123] `https://www.microcreate.nl/`. 25-02-2023.

Appendix: List of publications and contributions

In this appendix, a list of all publications, conference and workshop proceedings, and further contributions connected to this thesis work is presented.

Publications

- **Application of nanostructures and metamaterials in accelerator physics** - J.R. Lopez, O. Apsimon, C. Bontoiu, B. Galante, C.P. Welsch, G. Xia, A. Bonatto - **Proceedings of IPAC22** - MOPOMS016
- **Stability and lifetime studies of carbon nanotubes for electron cooling in ELENA** - B. Galante, G.A. Tranquille, C.P. Welsch, J.R. Lopez - **Proceedings of IPAC22** - MOPOMS028
- **Stability and lifetime study of carbon nanotubes as cold electron field emitters for electron cooling in the CERN extra low energy antiproton ring** - B. Galante, G.A. Tranquille, M. Himmerlich, C.P. Welsch, J.R. Lopez - **Phys. Rev. Accel. Beams** 24, 113401 - 2021.
- **Optimization of the electron emission from carbon nanotubes for electron cooling in ELENA** - B. Galante, G.A. Tranquille, C.P. Welsch, J.R. Lopez - **Proceedings of COOL21** - P1010
- **Carbon nanotubes as cold electron field emitters for electron cooling in the CERN Extra Low ENergy Antiproton (ELENA) ring** - B. Galante, G. A. Tranquille, C. P. Welsch, O. Apsimon, J. R. Lopez - **Proceeding of IPAC21** - WEPAB152

Oral presentations

- **NanoAc 2022: Application of Nanostructures in the field of Accelerator Physics** - Invited talk - Title: ”Characterization of carbon nanotubes as cold electron field emitters for electron cooling in ELENA”
- **AVA Topical Workshop: Machine-Experiment Interface, 2019** - Contributed talk - Title: “Data acquisition, data analysis, and simulation tools in a test bench environment”
- **IVNC-IVESC 2019: International Vacuum Nanoelectronics Conference and International Vacuum Electron Sources Conference** - Contributed talk - Title: “Generation of cold electrons for an eV electron cooler”.
- **AVA Topical Workshop: Low Energy facility design and optimization through diagnostics, 2019** - Contributed talk - Title: ”Study of cold electron emission sources for a cold cathode electron gun”

Poster presentations

- **IPAC22: International Particle Accelerator Conference** - Title: ”Stability and lifetime studies of carbon nanotubes for electron cooling in ELENA”
- **COOL21: International Workshop on Beam Cooling and Related Topics** - Title: ”Optimization of the electron emission from carbon nanotubes for electron cooling in ELENA”
- **IPAC21: International Particle Accelerator Conference** - Title: ”Carbon nanotubes as cold electron field emitters for electron cooling in the CERN Extra Low ENergy Antiproton (ELENA) ring”